A Study of the Electrical Flame Off Process During Thermosonic Wire Bonding with Novel Wire Materials

by

Andrew Pequegnat

A thesis
presented to the University of Waterloo
in fulfilment of the
thesis requirement for the degree of
Master of Applied Science
in
Mechanical Engineering

Waterloo, Ontario, Canada, 2010

Declaration

I hereby declare that I am the sole author of this thesis. This is a true copy of the thesis, including any required final revisions, as accepted by my examiners.

I understand that my thesis may be made electronically available to the public.

Andrew Pequegnat

Abstract

Thermosonic ball bonding is the most popular method used to create electrical interconnects between integrated circuits (ICs) and substrates in the microelectronics industry. Traditionally gold (Au) wire is used, however with industry demands for lower costs and higher performance, novel wire materials are being considered. Some of these wire materials include Cu, insulated, and coated wires. The most promising of which being Cu wire. Some of the main issues with these wire materials is their performance in the electrical flame off (EFO) step of the wire bonding process. In the EFO step a ball called the free air ball (FAB) is formed on the end of the wire. The quality of the FAB is essential for reliable and strong ball bonds. In Cu wire bonding the hardness of the FAB and oxidation are the main issues. A hard FAB requires larger bonding forces and US levels to make the bond which increases the likelihood of damage to the IC. Excessive oxidation acts as a contaminant at the bond interface and can also influence the shape of the FAB. Shielding gases are required to reduce oxidation and improve FAB quality. This thesis focuses on the EFO process and the influence of EFO parameters and shielding gases on Au and Cu FABs. The primary focus of this thesis is to provide a better understanding of the EFO process in order to expedite the introduction of novel wire materials into industry.

Several different experiments are performed on an automated thermosonic wire bonder with 25 μm Au and Cu wires to investigate the EFO process during ball bonding. The effects of EFO parameters on the hardness and work hardening of FABs and the effects of shielding gas type and flow rates on the quality of the FABs are determined. The EFO discharge characteristics in different shielding gases is also studied to better understand how the composition of the atmosphere the FAB is formed in influences the energy input via the EFO electrical discharge.

Using the online deformability method and Vickers microhardness testing it is found that the EFO current (I_{EFO}) and EFO time (t_{EFO}) have a large influence on the hardness and work hardening of Au and Cu FABs. A harder FAB produced with a large I_{EFO} and low t_{EFO} will work harden less during deformation. The bonded ball will be softer than that of a FAB produced with a lower I_{EFO} and higher t_{EFO}. The online deformability method is found to be twice as precise as the Vickers microhardness test.

An online method for characterizing the quality of FABs is developed and used to identify shielding gas flow rates that produce defective FABs. The EFO process for an Au wire and two Cu wire materials is investigated in flow rates of 0.2-1.0 l/min of forming gas (5 % H_2 + 95 % N_2) and N_2 gas. All three of the most common FAB defects are identified with this online method. It is found that good quality FABs cannot be produced above flow rates of 0.7 l/min and that H_2 in the shielding gas adds a thermal component to the EFO process. It is recommended that the gas flow rate be optimized for each new wire type used.

The EFO discharge power is measured to be 12 % higher in a N_2 gas atmosphere than in a forming gas atmosphere. The lower ionization potential of the forming gas leads to a higher degree of ionization and therefore lower resistance across the discharge gap. It was found that the discharge power does not determine the energy transferred to the wire anode because the Au FAB produced in forming gas has a 6 % larger diameter than that of the FABs produced in N_2 gas. Other factors that effect the voltage of the EFO discharge include the controlled EFO current, the discharge gap, and the wire anode material.

Acknowledgements

I would like to thank my supervisors Dr. M. Mayer and Dr. Y. Zhou for their input and support over the duration of this research. I was motivated to work hard and strive for my full potential. I have learned many valuable skills which will help further reach my career goals. The memories and successes that were shared with my colleagues in the CAMJ will never be forgotten.

Special acknowledgement goes out to John Persic for his advice and guidance. The technical support of Microbonds Inc., Markham, Ontario, Canada is greatly appreciated and was essential for the success of this work.

Finally, I would like to thank my family and beautiful fiancé, Colleen, for their love and support. My successes in life would not be possible without them.

Table of Contents

List of Figures

List of Tables

1.0 Introduction

The majority of electrical interconnects between integrated circuits (ICs) and substrates are made using wire bonds. Wire bonds connect the microelectronic devices to the macroelectronic system [1]. Competing technologies included tape automated bonding (TAB) and flip chip bonding. Due to wire bondings extensive infastructure, ability to support high performance device packaging, high manufacturing throughput, and its low cost, no other IC interconnection technology is expected to displace wire bonding in the foreseeable future [1, 2]. In 2006 90 % of all IC interconnects are made with Gold (Au) wire bonds [1].

Since the development of thermocompression wire bonding in 1957 by Bell Laboratories wire bonding technologies have been rapidly evolving in order to keep pace with the microelectronics industry demands. Large advances in the wire materials, capillary design and the bonding machines have taken place. Two major advances in the wire bonding technology are the development of ultrasonic wedge bonding in 1960 and the development of thermosonic wire bonding in 1970. Thermocompression wire bonding requires high temperatures (> 300 °C), larger bonding pads than ultrasonic and thermosonic wire bonding, and has the lowest yield. Ultrasonic wedge bonding is performed at room temperature, has the highest yield of the processes (< 20 ppm), but only has half of the manufacturing throughput of the other processes. Thermosonic wire bonding combines the best qualities of the thermocompression and ultrasonic wire bonding technologies. Thermosonic wire bonding uses lower temperatures in order to not damage sensitive components and ultrasonic (US) energy which helps disperse contaminants at the bond interface and aid in deformation. Thermosonic ball bonding has the ability to bond in all directions and is easily automat-

ed making the process very fast. Today the majority of all interconnections to ICs are made with Au thermosonic ball bonds [2]. The thermosonic ball bonding process is used in this study.

The general trends in the microelectronic industry are for higher performance, lower costs, and miniaturization [3, 4]. The wire bonding industry responds to these trends by developing low-cost packaging solutions for fine pitch, high input-output devices. One approach to meeting these demands is the development of new wire types and materials. The most promising materials are Cu, insulated, and coated wires [5-7]. However, these new materials pose new process challenges in particular during the first step of the thermosonic ball bonding cycle called the electrical flame off (EFO) process, where a ball is formed on the end of the wire. The ball formed on the end of the wire is called the free air ball (FAB) and its quality is essential for reliable and strong ball bonds. There is a need for more research in this area in order to advance the thermosonic ball bonding process to a point where these new materials will be fully accepted by industry.

1.1 Objectives

This study is performed in order to better understand the EFO process. The knowledge obtained through this study helps to advance the thermosonic bonding process to a point where new wire materials will be accepted by industry. The main FAB issues associated with Cu such as its higher hardness and oxidation are addressed as well as the conditions at which acceptable shape and quality FABs are produced. In order to fulfil these objectives the following tasks were performed:

a) investigation into the effect of EFO parameters on FAB hardness and work hardening,

b) investigation into the effect of shielding gas type and flow rate on FAB formation, and

c) preliminary investigation of the EFO discharge and how the properties of both the discharge and wire materials effect FAB formation.

1.2 Thesis Organization

This work focuses on the EFO stage of the thermosonic ball bonding process. Chapter 1 gives a detailed introduction into the thermosonic wire bonding process. The motivation for using novel wire materials and the issues associated with them are presented. The effects of the EFO parameters on the FAB hardness and work hardening are presented in Chapter 2. The hardness and deformability of Cu and Au FABs are investigated using two different evaluation techniques. The hardness and work hardening of different wire materials are compared. In Chapter 3 the effects of shielding gas types and flow rates on the quality of the FAB is investigated. A new technique for quickly assessing the shape of the FAB is presented allowing for the identification of undesirable flow rates. Preliminary work investigating the influence of shielding gas composition on the EFO discharge is presented in Chapter 4. The energy transferred to the wire via the discharge and the factors that effect the discharge power are investigated.

1.3 The Thermosonic Ball Bonding Process

In the thermosonic ball bonding process normal force, heat, and US energy are used to make the bonds. First a bond is made between the wire and the metallization on the IC device (i.e. ball bond) then a second bond is made to the substrate or leadframe (i.e. wedge bond) that carries the IC. The thermosonic process is a solid-state bonding process where no melting occurs during bonding [8]. Metallic bonds are formed where intimate contact is achieved between the two materials to be joined at the atomic level.

The thermosonic ball bonding process steps are illustrated in Figs. 1 a) to e). The first step of the ball bonding process is the EFO process. During EFO a high electrical potential is applied between the electrode and the wire tail that protrudes from the capillary resulting in an electrical discharge or spark. The tip of the wire tail melts and the molten metal rolls up in to a spherical ball due to surface tension where it then solidifies [Fig. 1 a)]. This ball is called the free air ball (FAB). After EFO the wire clamp is opened and the capillary moves downward towards the heated IC device, which is typically heated to a temperature around 150 °C. A bonding force is then applied deforming the FAB between the ceramic capillary and the bond pad metallization on the device. Ultrasonic (US) energy is applied simultaneously and the ball bond is formed via a solid-state bonding mechanism [Fig. 1 b)]. After the ball bond has been formed the capillary moves to the second bond location. During this step the wire clamp is open allowing for the wire to be fed out, forming the wire loop [Fig. 1 c)]. Once at the second bond location, again the bonding force and US energy is applied. The wire is deformed between the capillary and the lead finger or substrate and the second bond is created [Fig. 1 d)]. The last step is the wire tail formation which is necessary for the process to continue. During this step the capillary moves upward with the wire clamp

opened until the desired tail length is achieved where the clamp is then closed. The tail bond between the wire tail and the lead finger or substrate is then broken creating the wire tail [Fig. 1 e)]. A FAB can now be formed on the wire tail and the process will continue.

1.3.1 Electrical Flame Off Process

Since the primary focus of this study is on the formation of FABs during the thermosonic ball bonding process, a more in depth review of the EFO process step is provided. The FAB shape and surface quality are essential for reliable ball bonds [9-11]. A DC constant current power supply is used for producing the EFO discharge where the EFO current (I_{EFO}) is the input parameter and the EFO voltage is the response. In the modern EFO process a negative EFO (NEFO) discharge is used meaning the electrode is the cathode. A NEFO discharge is beneficial since it results in a more uniform FAB formation which is necessary for high yield and fine pitch bonding. Also, foreign particles are not attracted to the wire and capillary and in the case of Au ball bonding, Au is not sputtered from the wire and deposited on the capillary [2].

1.3.1.1 The EFO discharge

The EFO discharge is initiated by applying an electrical potential that exceeds the breakdown potential of the gas in the gap between the electrode and the wire. This voltage is referred to as the pre-spark voltage. At standard temperatures and pressures gases are excellent insulators [12]. Once the breakdown potential is exceeded the gas ionizes and begins to conduct electricity. The ionization of a gas due to an electrical potential is called field ionization [12]. As the gas heats up thermal ionization will also occur [12].

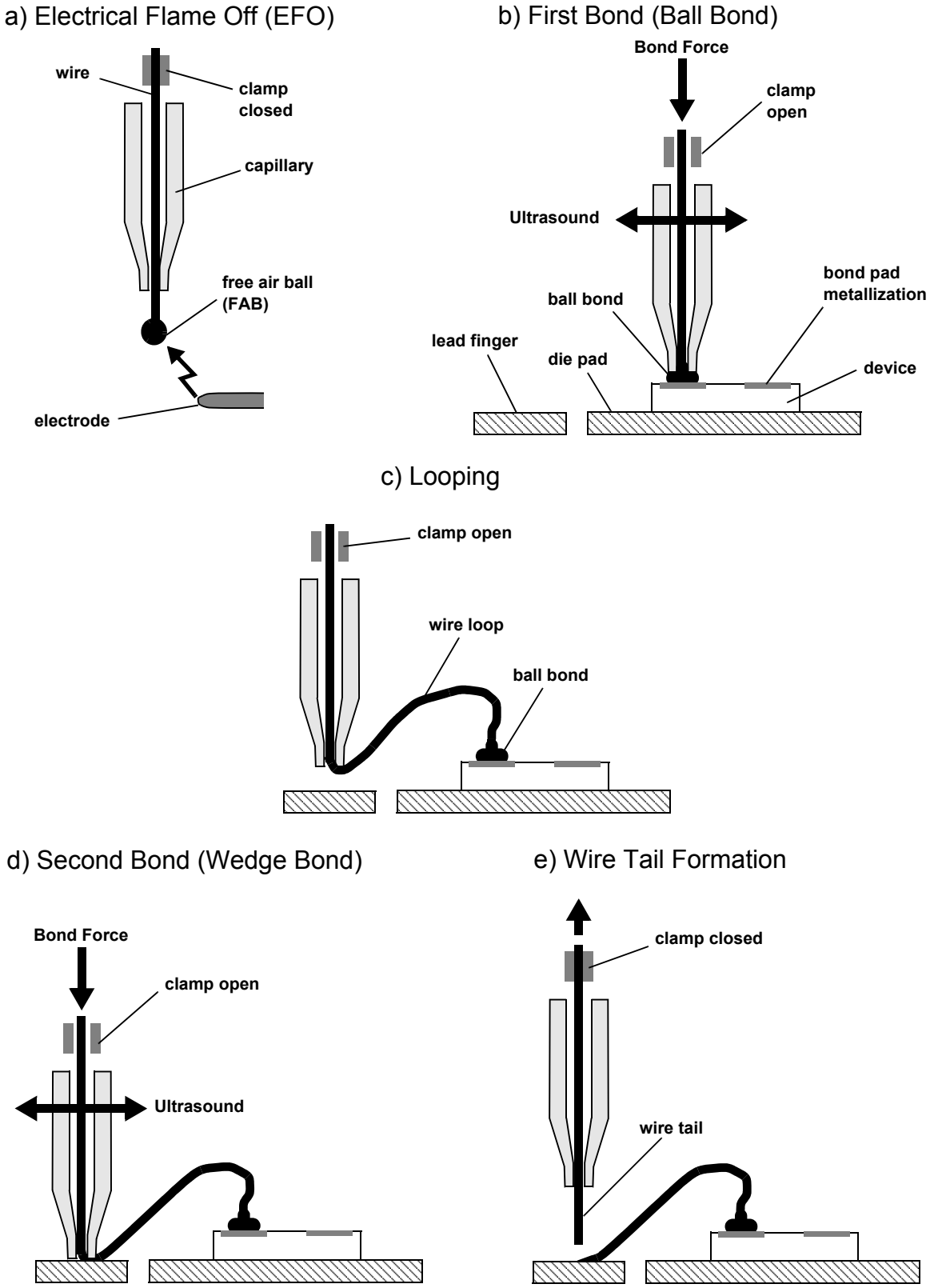

Figure 1: Illustration of thermosonic (TS) ball bonding process steps: a) electrical flame off (EFO), b) ball bond, c) looping, d) wedge bond, and e) tail formation.

In the EFO discharge, once a sufficiently high energy level is achieved, the gas molecules will dissociate into a monatomic state breaking the interatomic bonds. As the energy in the gas further increases, the outer electrons are detached from the atom [13]. Once the electrons have been stripped from the atom, they are accelerated to high speeds in a short distance by the large electric field. When the high speed electrons collide with other atoms or ions with an energy that exceeds their ionization energy, the particles are ionized producing more electrons [14]. The collisions are elastic if no ionization occurs and inelastic if some of the energy is absorbed due to ionization [13]. As the number of these elastic and inelastic collisions increases, an avalanche of electrons and positive ions is formed [15]. If the applied voltage is large enough, this avalanche of electrons produces a sufficient amount of electrons and protons to be self-sustained and will reach a steady-state, as required during the EFO process [14]. The electrons will flow towards the wire (anode) and the protons will flow towards the electrode (cathode) due to the applied electromagnetic fields and the gas conducts electricity as illustrated in Fig. 2 [12]. Due to the smaller mass of the electrons they move more readily and therefore carry the majority of the current [12].

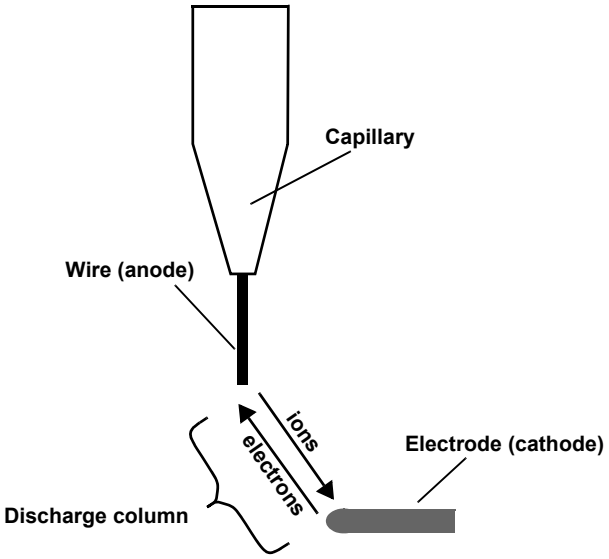

Figure 2: Illustration of the flow of electrons and ions in the NEFO discharge. The wire is the anode and the electrode is the cathode.

The EFO discharge is classified as a low energy, weakly ionized plasma [12]. Therefore, the electron density will be quite low and the voltage drop across the discharge will remain quite high. The voltage during an EFO discharge in air was measured to be 390 V for a 28 mA I_{EFO} [14]. The discharge power is calculated using

$$P = VI_{EFO} \tag{1}$$

where V is the discharge voltage and I_{EFO} is the EFO current [16]. The gas atmosphere that the EFO discharge is produced in has an effect on the power. Different gases will have different ionization energies and therefore, the gap between the electrode and the wire will have different resistances. This becomes a factor when shielding gases are used in forming Cu FABs which will be discussed in more detail in section 4.0.

1.3.1.2 Electrical Flame Off Parameters

The main parameters in the EFO process are the I_{EFO}, EFO firing time (t_{EFO}), pre-spark voltage, wire tail length, and the discharge gap (or electrode to wire distance).

The I_{EFO} and t_{EFO} are adjusted in order to adjust the energy input. The electrical energy input for the EFO process can be defined as

$$E = RI^2t \ , \tag{2}$$

where *E* is the energy input, *R* is the resistance across the discharge, *I* is the EFO current, and *t* is the EFO time [9]. The diameter of the FAB is dependent on the energy input during the EFO, therefore the I_{EFO} and t_{EFO} are optimized to obtain the desired FAB size. Note that in industry the time is often held constant so that the duration of the bonding process is not changed. A shorter time is often desired to speed up the process.

The pre-spark voltage ranging from 1500 V to 6000 V is applied in order to initiate the discharge by electrically breaking down or ionizing the gas in the gap to create a continuous plasma discharge [1]. The breakdown potential and ionization energy properties of the gas atmosphere in the gap affect the properties of the discharge and how much energy is required to initiate it.

The wire tail length and gap parameters are illustrated in Fig. 3 a).The tail length is usually between 300 - 550 µm for 25 µm (1 mil) wire diameters. It has an effect on the FAB diameter where a larger tail length has a higher resistance producing more resistive heating in the wire tail and therefore a larger FAB. The tail length must not be too short so that the wire is melted back to the capillary tip during the formation of the FAB. During Cu ball bonding the tail length is more critical because the molten metal on the end of the wire must always be surrounded by a protective atmosphere. For example, if the tail length is too short the molten metal can leave the path of the shielding gas flow as it rolls upward due to surface tension causing oxidation issues.

The gap influences the discharge length and the angle at which the discharge travels. When optimizing the gap a good starting point is to have the discharge axis at 45 ° relative to the wire tail

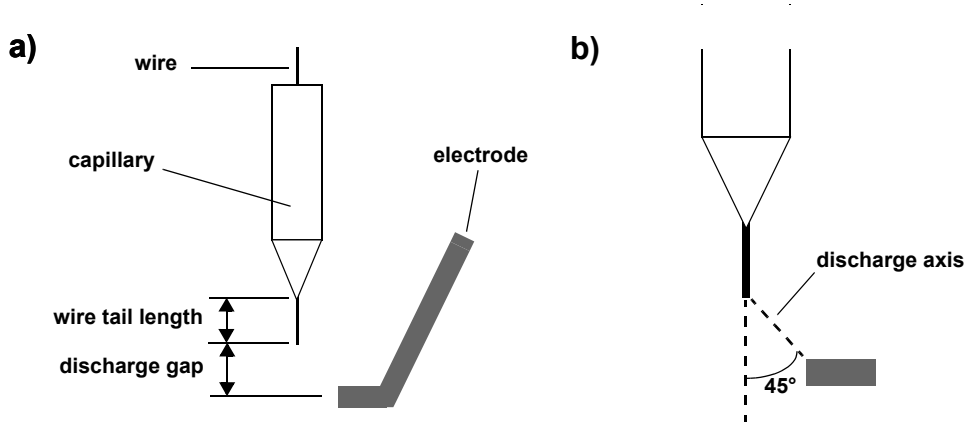

Figure 3: Schematic illustration of EFO process highlighting: a) Wire tail length and discharge gap, and b) 45 ° angle between discharge axis and wire axis.

as illustrated in Fig. 3 b). Shorter gap (i.e. shallower discharge angle) can lead to FAB defects. Coated and insulated wires are less sensitive to the discharge gap. It has been suggested that the higher resistance of the coating material than the base wire material leads to a higher current density at the tip rather than the discharge spreading up the wire tail [7].

1.3.1.3 Copper Wire Electrical Flame Off Process

One of the main disadvantages of Cu wire is that it readily oxidizes in air. Oxidation can occur very rapidly on the surface of the molten Cu during the EFO process. Oxidation on the surface of the FAB degrades bond quality and can even lead to non-stick-on-pad (NSOP) failures causing stoppages in production and therefore, reducing production yield [9-11]. Oxidation has also been found to increase the hardness of the FAB itself [17]. The oxidation of Cu wire during the EFO process is reduced by supplying a shielding gas to the EFO site during FAB formation. The major machine manufacturers now offer Cu kits which are essentially a means of supplying the shielding gas to the EFO site. An illustration of the Cu kit on the Esec 3100 thermosonic ball bonder manufactured by Besi Esec, Cham Switzerland is shown in Fig. 4. A picture of the bondhead is shown in Fig. 5. The shielding gas is supplied through a nozzle attached to the electrode.

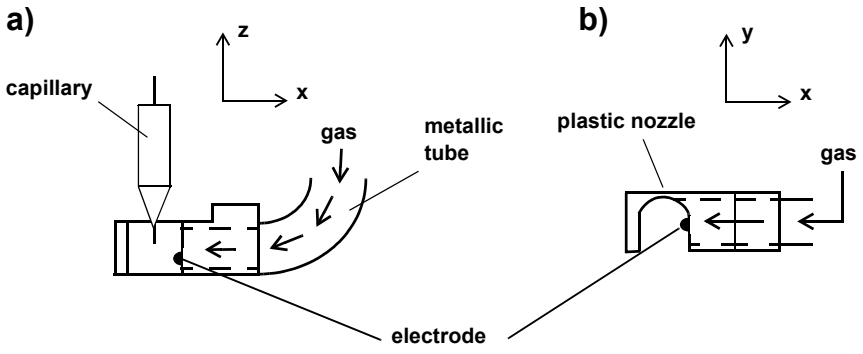

Figure 4: Illustration of the Cu kit on the Esec 3100 thermosonic ball bonder: a) front view, and b) top view. The metallic tube has an inner diameter of 1 mm.

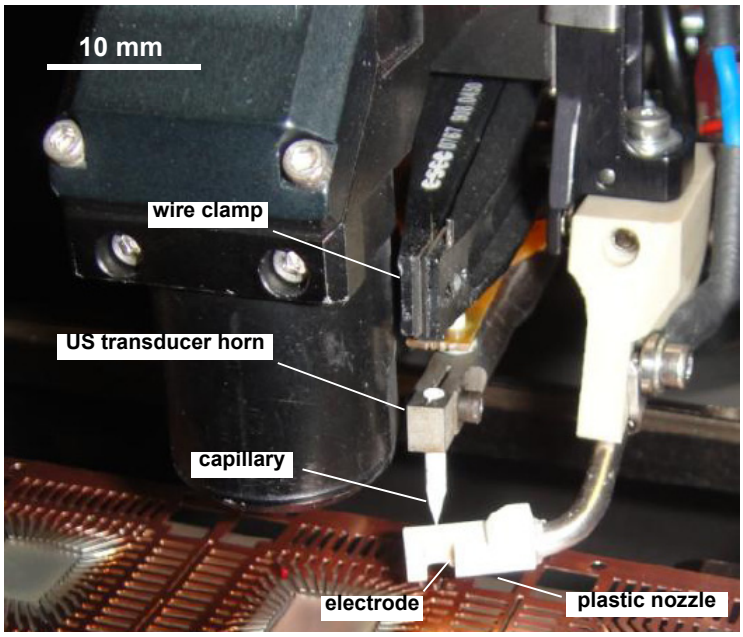

Figure 5: Besi Esec 3100 thermosonic wire bonder bondhead.

The shielding gasses used are usually a mixture of H_2 and an inert gas such as Ar or N_2 [18]. These gas mixtures are termed forming gasses in the wire bonding industry. A mixture of 5 % H_2 and 95 % N_2 is the most common forming gas mixture used today. The hydrogen is added to the gas mixture to reduce the oxide on the wire surface during the EFO process.

The melting and solidification of the FAB during the EFO process has been studied extensively for Au wire [12, 14, 19]. Complex models have been developed to help understand the formation of the Au FAB during EFO [19]. A simulation of the melting and solidifying of a 25 µm (1 mil) Au wire during FAB formation is shown in Fig. 6 [19]. The formation of a Cu FAB however is even more complex due to the effects of oxidation and the use of a shielding gas. Factors such as extensive oxidation and convective cooling affect the formation of the FAB and can cause FAB defects [9, 11, 20]. Two new variables are introduced in Cu ball bonding; the shielding gas type and the flow rate.

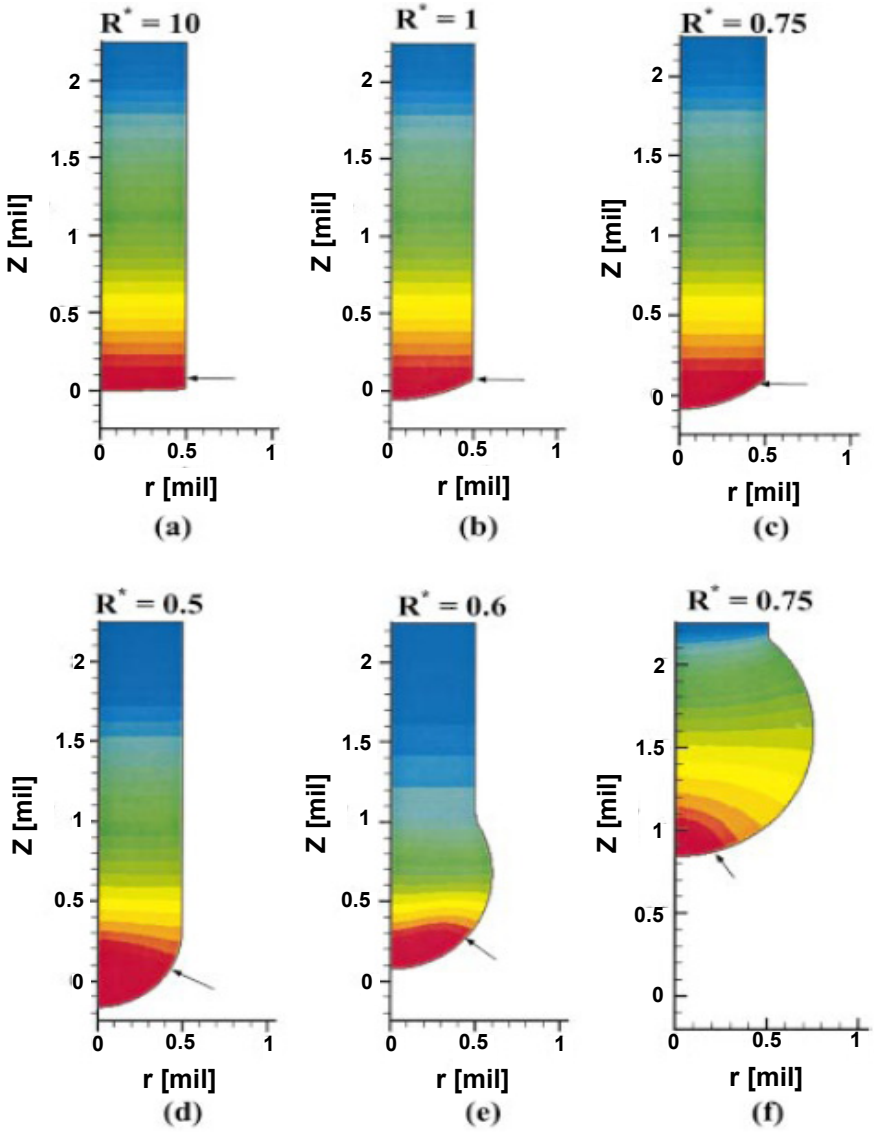

Figure 6: Simulation of the evolution of the FAB during melting and solidification of a 25 µm (1 mil) Au wire anode where R^* = radius of curvature and the arrow denotes location of the solid-liquid interface. Time increases from (a) to (f). From (a) → (d), the tip of wire melts and the gap between the electrode and wire decreases by 0.2 mil. From (e) to (f), the molten metal rolls up into a ball due to surface tension and the electrode to wire gap increases by 0.8 mil [19].

1.4 Proposed Bonding Mechanisms

Both the ball and wedge bonds of the thermosonic wire bonding process are solid state joining processes where no melting occurs. In thermosonic wire bonding the bonds are not created as a result of the applied heat during bonding nor are they created from the heat generated by the US energy. The temperatures reached during bonding are well below the melting temperature of the materials and even below the temperatures required for thermocompression bonding (< 300 °C) [8]. Temperature measurements during US bonding indicate that the temperature does not rise above 250 °C [21, 22]. As further proof that high temperatures are not required, US bonding has been performed in liquid N_2 (77 K) [21, 23]. Therefore, the US energy transmitted through the atomic lattice is suggested to be sufficient to overcome the activation energy required for joining [8].

In general the thermodynamic driving force for materials joining is a decrease in Gibbs free energy. For materials joining the change in Gibbs free energy can be expressed as:

$$\Delta G = \gamma_{12} - \gamma_1 - \gamma_2 \tag{3}$$

where, ΔG is the change in Gibbs free energy, γ_{12} is the interfacial free energy, and γ_1 and γ_2 are the surface free energies of the wire and the metallization, respectively. The energy of adhesion can also be expressed in terms of the interfacial and surface free energies as defined by Duprè:

$$E_{ad} = \gamma_1 + \gamma_2 - \gamma_{12} \tag{4}$$

where, the energy of adhesion is defined as the work required per unit area to separate two solids [24, 25]. A small interfacial free energy is desired in all materials joining processes. In wire bonding the interfacial free energy is increased by contaminants or oxidation at the interface, excessive roughness, or large lattice mismatch between the wire material and the metallization material.

In the thermosonic ball bonding process intimate contact between the bare materials and therefore, low interfacial free energy is obtained by deformation with US, heat, and the selection of bonding partners/materials with "compatible" lattice constants. Oxidation and contaminants are broken up during deformation and local straining due to US. The contaminants are displaced to the bond perimeter or into asperities on the surface by plastic flow. Excessive surface roughness or large asperities are deformed and collapsed. Deformation epitaxy leads to a reduction in crystallographic mismatches by crystallographic rearrangement of the contacting surfaces by plastic deformation [24]. The absence of bonded area in the center of US wedge bonds where little deformation takes place is a common occurrence [2]. In thermosonic ball bonding where a large degree of deformation and plastic flow takes place causing the unbonded regions to be more dispersed and random [2]. This indicates the importance of plastic deformation and flow in removing contaminants and reducing lattice mismatch allowing for a bond to be created.

Heat and US aid in deformation and plastic flow in the thermosonic wire bonding process. It is well known that heating bulk materials provides some of the additional energy required for plastic deformation. The homogeneous heating of the materials being joined aids in deformation by reducing the required deformation stress. Superimposing US during the plastic deformation of a metal can also reduce the required deformation stress. This temporary reduction in strength is referred to as acoustic softening [29-31]. Langenecker shows this temporary reduction in strength by performing tensile tests on Al single crystals while applying various levels of US irradiation as shown in Fig. 7 a) [29]. The reduction in strength due to US irradiation is compared to the reduction in strength caused by heating in Fig. 7 b) [29]. From dislocation theory, it is proposed that the preferential absorption of acoustic energy by lattice imperfections such as dislocations or grain bound-

aries will cause localized heating in the regions around the imperfections [29]. The localized heating activates the dislocations and reduces the resolved shear stress required for substantial dislocation migration in the slip plane resulting in acoustic softening [29, 30]. The activation of dislocations by acoustic softening is much more efficient than heating the bulk materials [29].

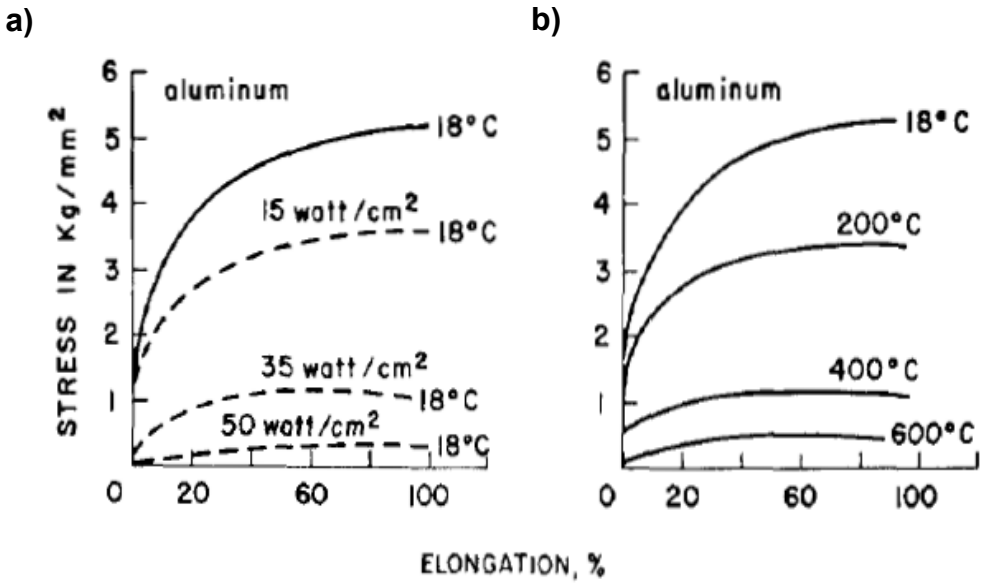

Figure 7: Stress-strain curves from tensile tests performed on Al single crystals while applying various levels of US (a) and various test temperatures (b) [29].

1.5 Quality Assessment

The traditional quality assessment methods are often quite manual and tedious. Many of these tests are replaced with "online" methods, where data is collected from the wire bonder during bonding. Online methods will be discussed in subsequent sections.

1.5.1 Destructive Bond Pull Test

Wire pull testing is most commonly used to measure the pull strength of the wedge bond and the strength of the neck of the ball bond. The pull test values are obtained using a pull tester that uses a hook to pull on the wire at a specified rate while measuring the force at failure. For measuring the pull strength of the wedge bond the hook is placed 1/3 of the ball to wedge distance (BWD) from the wedge bond as illustrated in Fig. 8 a). Interfacial failure of the wedge bond or the ball bond during pull testing indicates poor bond quality even if the measured pull force at failure is quite high [1]. When the pull hook is placed 1/3 of the BWD from the ball bond as illustrated in Fig. 8 b) the strength of the heat affected zone (HAZ) in the ball neck is obtained. The ball neck strength is of particular interest when ball bonding with new wire materials [32]. Destructive wire pull testing is governed by the MIL-STD-883E standard [33].

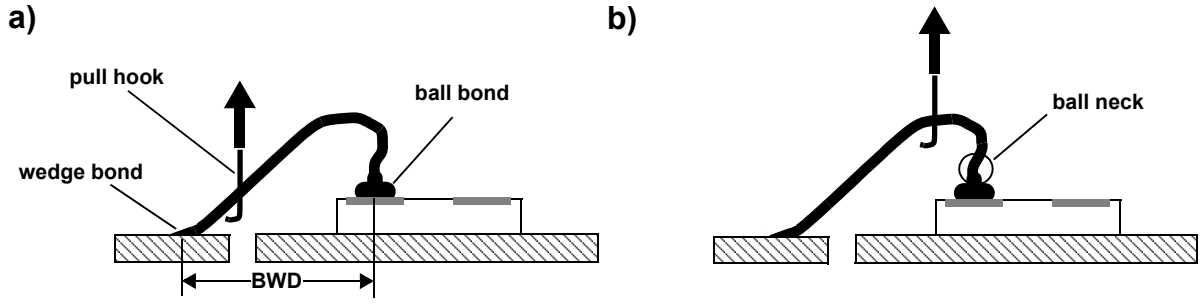

Figure 8: Illustration of pull testing a) for measuring wedge pull force and b) for measuring HAZ or neck breaking force.

1.5.2 Ball Bond Shear Test

Shear testing is a destructive test that quantifies the strength of the ball bond at the interface between the bonded ball and pad metallization. A shear tool applies tangential force to the ball bond and measures the shear force at failure as illustrated in Fig. 9. The shear force is then divided by the bonded area to calculate the shear stress which is often given in units of gf/mil^2 (1 gf/mil^2 is equal to 15.2 MPa). Since the bonded area is difficult to measure directly, the ball diameter at capillary imprint (BDC) where the capillary makes contact to the top of the ball during bonding is often used to estimate the bonded area. The BDC is illustrated in Fig. 9.

For a proper shear test the bottom of the shear tool should sit about half the ball height from the pad surface [1]. In the shear testing there are many different failure modes. The most common being interfacial shear, ball shear, and cratering [1, 2]. Interfacial shear is undesirable in fine wire Au ball bonding often indicating a poor bonding process or excessive intermetallic growth [2]. Ball shear indicates that the bond is stronger than the wire material itself. This failure mode is often desired for fine wire Au ball bonding. However, as the wire diameter is increased or stronger wire materials such as Cu are used ball shear will not occur. A higher shear stress value is desired in this

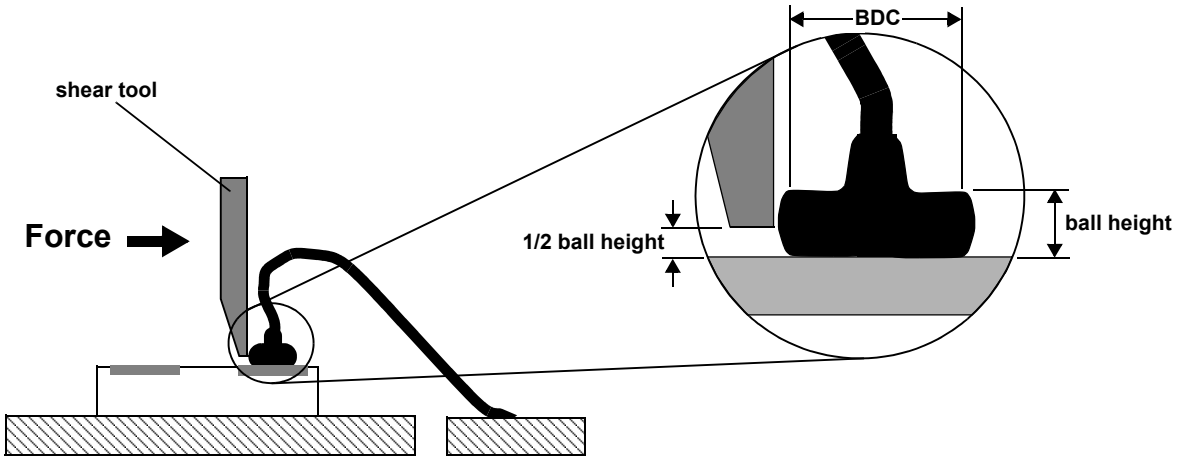

Figure 9: Illustration of ball bond shear testing.

case. With stronger (harder) materials such as Cu, the cratering failure mode can occur. Cratering indicates that the bondpad has been weakened or cracked by the bonding process. Cratering is often a result of hard FABs and/or excessive US during bonding [1, 2, 34, 35]. The destructive shear testing method is governed by the JEDEC JESD22-B116 standard [36].

1.5.3 Visual Inspection of Free Air Balls

The shape and surface quality of the FAB is essential for ball bond reliability and high yield. Assessing the quality of the FAB can be done indirectly by shear testing. However, optical or scanning electron microscopy (SEM) images are required to confirm FAB quality or identify defects. Visually inspecting FABs is a highly manual process and can be quite tedious. It is necessary when optimizing a new EFO process or for troubleshooting ball bond failures. In order to observe the FAB shape and quality, first a FAB is formed on the wire tail [Fig. 10 a)], then the wire tail is bent [Fig. 10 b)] and a bond-off (wedge bond) is performed to fix the FAB to the substrate. This process is often referred to as the cherry-pit method. The FAB now sits upright on the substrate ready to be inspected as illustrated in Fig. 10 c).

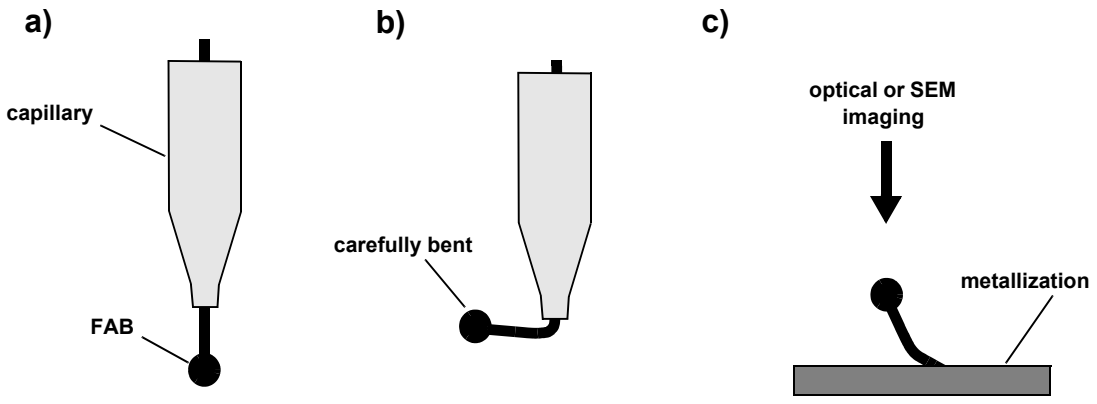

Figure 10: Illustration of free air ball (FAB) sample preparation for visual inspection. a) EFO process, b) bend wire tail, and c) bond-off (wedge bond).

1.5.3.1 Common Free Air Ball Defects

There are two different categories of FAB defects; shape defects and surface contamination. Common shape defects include size variation, golf-clubbing, and pointed shape. Size variation is an indication of an unstable EFO process and is usually a result of an unstable discharge. This type of defect is often observed when the voltage and current parameters are too low. The golf-clubbed FAB defect is when the wire is formed off-center or non-symmetrical to the wire axis as illustrated in Fig. 11 b). The pointed FAB defect is when the FAB is not round and solidifies in a pointed shape as illustrated in Fig. 11 c).

Variation in FAB size is undesirable because weak bonds or NSOP failures can occur as well as undesirable changes in ball bond geometries. Non-symmetrical golf-clubbed FAB defects can lead to shorting issues in fine pitch applications. The resulting bonded ball will also be non-symmetrical and can make contact with adjacent bond pads or ball bonds. An examples of a golf-clubbed FAB and a bonded golf-clubbed FAB are shown in Fig. 12 a) and b), respectively [11]. Pointed FAB defects lead to higher stresses on the bondpad during the impact portion of the ball bond process which increases the likelihood of underpad damage and cratering. An example of a pointed FAB and cratering caused by bonding a pointed FAB are shown in Fig. 13 a) and b), respectively [11].

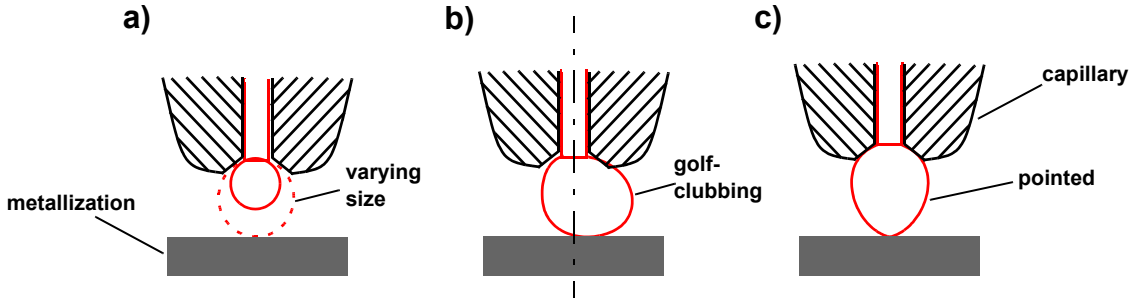

Figure 11: Common FAB defects. a) Variation in size, b) golf-clubbed FAB defect, c) pointed FAB defect.

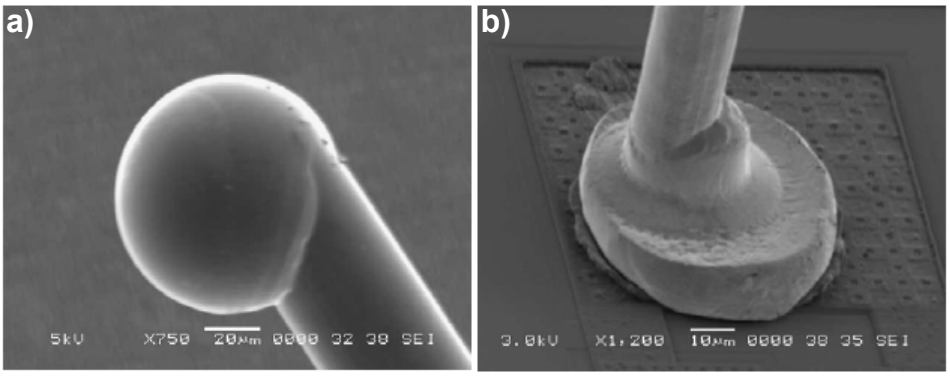

Figure 12: SEM image of a golf-clubbed FAB (a) and a bonded golf-clubbed FAB (b) [11].

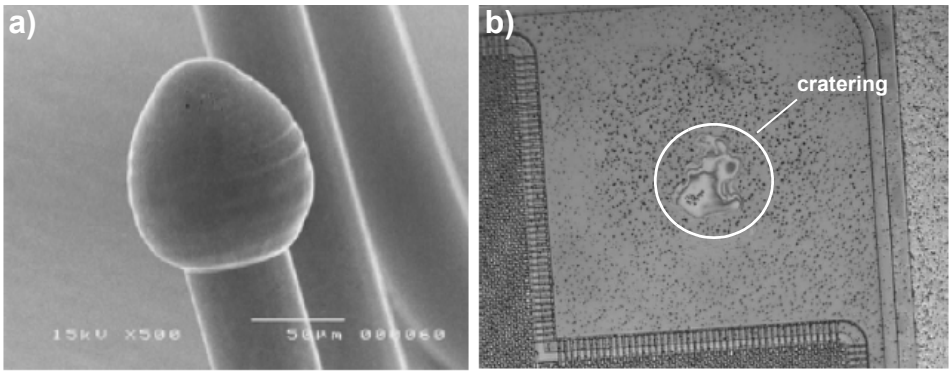

Figure 13: SEM image of a pointed FAB defect (a) and a cratered bond pad resulting from bonding a pointed FAB [11].

Surface contamination makes ball bonding with Cu, insulated, and coated wires more challenging. Surface contamination leads to decreases in shear strength and process yield. Contaminants at the bond interface prevent bond formation by preventing the deformed metal surfaces from coming into intimate contact.

One example of a surface contaminant is surface oxidation of the Cu FAB. Thin, hard oxides on a soft material such as Al wires will be broken up and displaced with deformation and US as occurs during the ultrasonic wedge bonding process. However, soft oxides on hard metals such as Cu oxide on Cu can serve as a lubricant during deformation during bonding, remaining on the surface and degrading bond quality [2]. Example optical and SEM images of Cu FABs are shown

in Fig. 14. An example of a Cu FAB with minimal surface oxide is shown in Figs. 14 a) and b). In the optical image the surface appears smooth and light in colour. The grain boundaries can be identified in the SEM image. In Figs. 14 c) and d) the Cu FAB is slightly more oxidized the surface appears rough with an orange peel like texture and the oxide is dark orange in colour. Also, holes start to appear on the surface of the FAB and the grain boundaries become less obvious. In Figs. 14 e) and f) the oxidation is sever and the surface appears very rough with many holes. In the optical image the oxide become brown in colour and in the extremely oxidized areas appears blue.

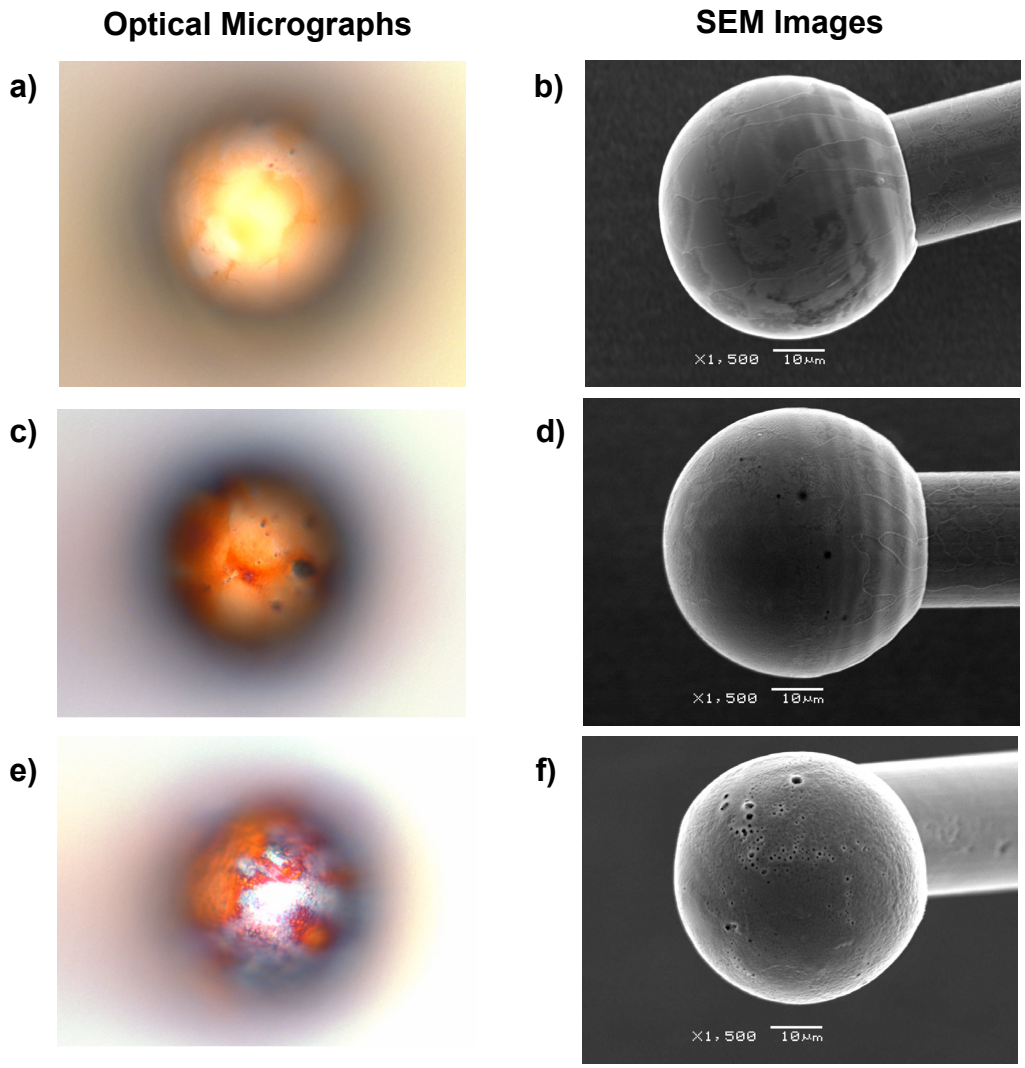

Figure 14: Optical and SEM images of Cu FABs in various stages of oxidation. Little oxidation (a & b), medium amount of oxidation (c & d), severely oxidized (e & f).

For insulated wires the insulation that is not removed during EFO acts as a contaminant and degrades the ball bond quality. In order to remove the insulation during EFO a certain amount of energy is required. Fig. 15 shows optical and SEM images of insulated Cu FABs where the insulation has not been fully removed from the FAB surface. The insulation is identified in the optical images by white or grey regions highlighted in Fig. 15 a) or by the rippled/creased surface as seen in Fig. 15 c). In the SEM images the insulation is dark in contrast and will also have a rippled or creased appearance in some cases as shown in Figs. 15 b) and d).

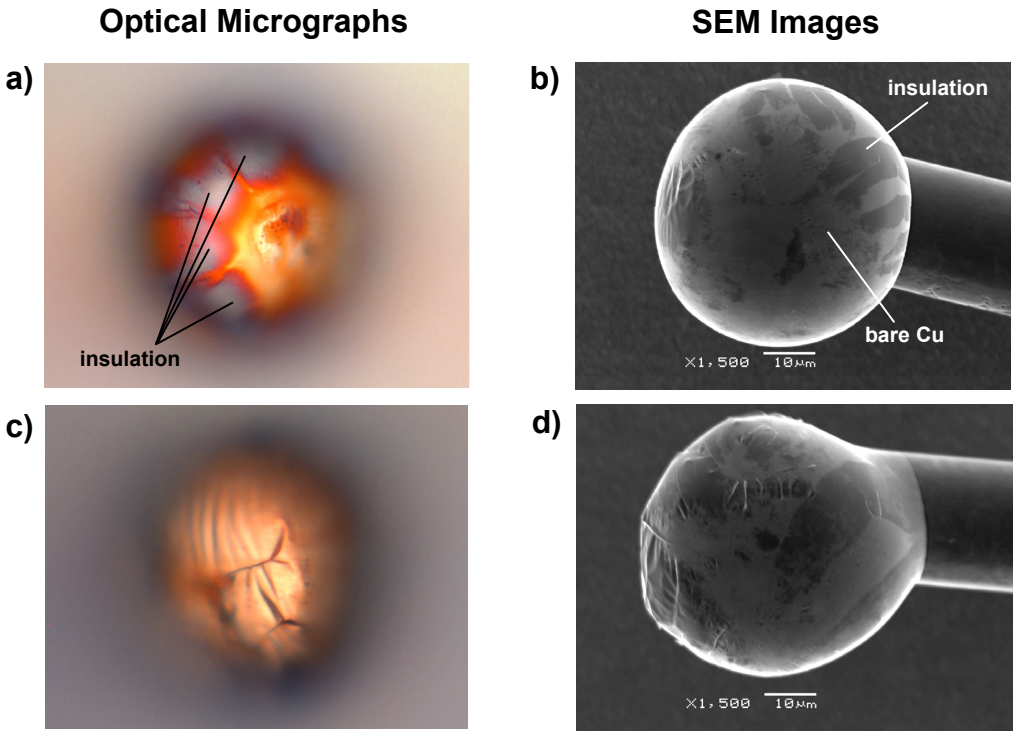

Figure 15: Optical and SEM images of insulated Cu FABs where the insulation has not been fully removed during EFO. In the SEM images the insulation is dark in contrast to bare Cu.

1.5.4 Vickers Hardness Testing

The hardness of the base wire material and the FAB influences the likelihood of damage to the IC during bonding. Vickers hardness tests are often performed on cross-sectioned wire, FABs, and Bonded balls as shown in Fig. 16 a), b), and c), respectively [35-38].

Due to the small size and thickness of the cross-sectioned samples low forces must be used during Vickers hardness testing. In this study a 49 mN (5 gf) force with a 15 s dwell time is used.

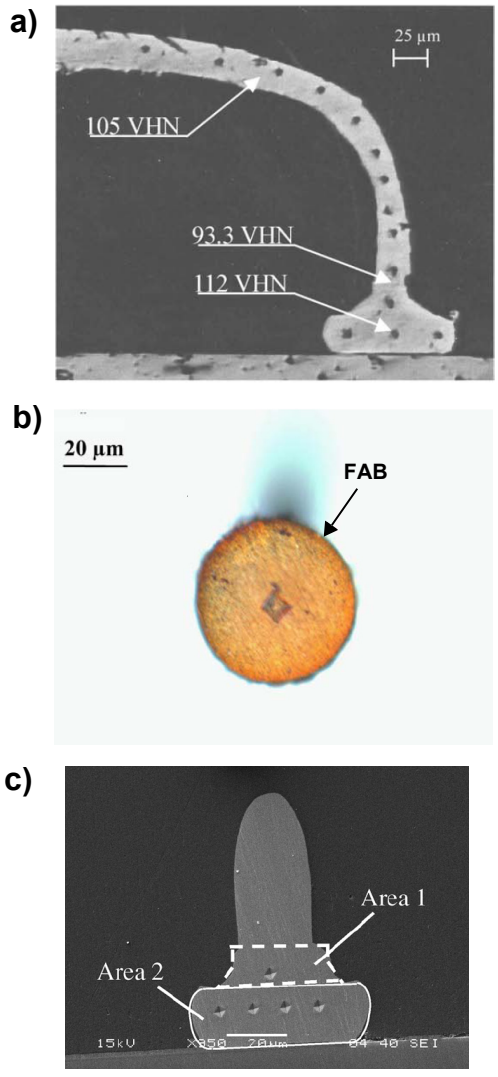

Figure 16: Vickers hardness tests performed on a) Cu wire and bonded ball, b) Cu FAB, and c) Cu bonded ball [35-38].

The measurements are made using either an optical microscope or SEM and the vickers hardness is calculated using:

$$HV = \frac{1854.4 \times P}{d^2} \tag{5}$$

where P is the applied load in gf and d is the average length in μm of the two diagonals measured from the microhardness indentation [39].

1.6 Online Characterization Methods

Online methods have been developed to reduce the time required for characterizing new wire materials and study the effects of process parameters on the wire materials during bonding. The online methods use signals from the wire bonder sensors to quantify deformability of the wire and the FAB, measure tail breaking force (TBF), measure heat affected zone (HAZ) breaking force, and even investigate the temporary and residual effects of US on hardness and deformability of the FAB during bonding [32-35, 40-45]. For each case the Esec 3100 thermosonic wire bonder, manufactured by Besi ESEC, Cham, Switzerland shown in Fig. 17 is used. The two sensors used for the online methods are the z-position encoder located on the back of the rocker arm and the proximity sensor fixed below the wire clamp as illustrated in Fig. 18 [46]. The z-position encoder is used to derive the position of the capillary tip with sub micron precision [40]. The proximity sen-

Figure 17: Besi Esec 3100 automated thermosonic wire bonder.

sor measures changes in the gap between the clamp and the horn due to deflection of either the horn or the clamp when they are placed under a specific load [41]. The change in the gap distance is proportional to the load applied to either the horn or the wire clamp.

1.6.1 Online Deformability Measurement

For the online deformability measurements the amount of deformation is quantified by the z-position of the capillary tip after a certain deformation force has been applied. This method can be used to measure both the deformability of the FAB and the wire itself [40]. The height measurements required for calculating the deformability of both the FAB and the wire are illustrated in Fig. 19 [40]. A reference wedge bond (RW) is required in order to measure the deformability of the FAB. Therefore, a column of reference bonds is placed next to the test bonds as illustrated in Fig. 20. The deformed ball height (BH) and deformed wire height (WH) are calculated by:

$$BH = Z_B - Z_{BR} \text{ and} \tag{6}$$

$$WH = Z_W - Z_{WR}. \tag{7}$$

Example signals for z-position, force, and US provided by the bonder for the deformability measurements are shown in Fig. 21.

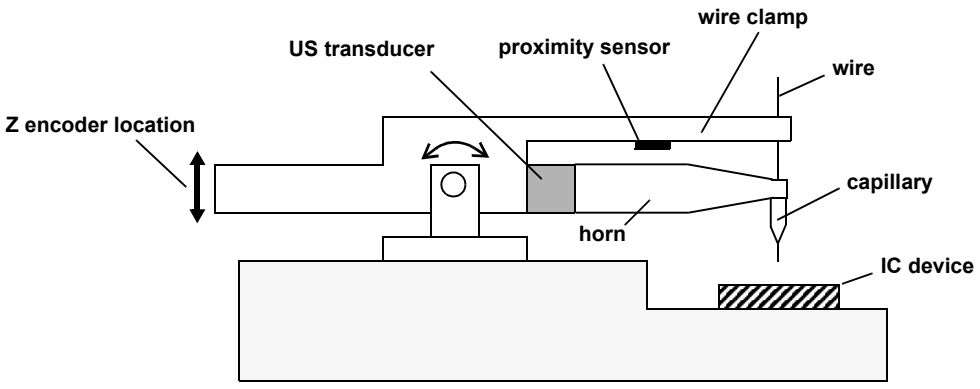

Figure 18: Schematic drawing of the Esec 3100 bondhead rocker arm assembly. Dimensions not to scale [46].

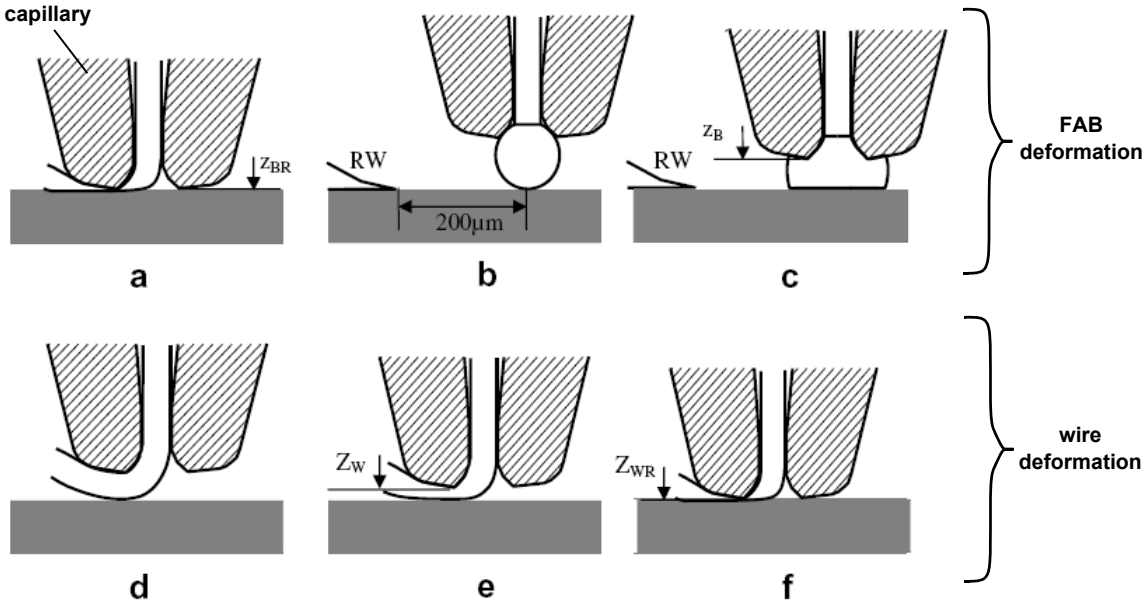

Figure 19: Height measurements: a) reference wedge bond (RW) with capillary touching the substrate surface, b) FAB contacts the substrate without deformation, c) FAB deformed under a predefined deforming force, d) wire side contacts the substrate without deformation, e) wireside deformed under a predefined deforming force, and f) ultrasonic wedge bond with capillary touching the substrate surface for reference [40].

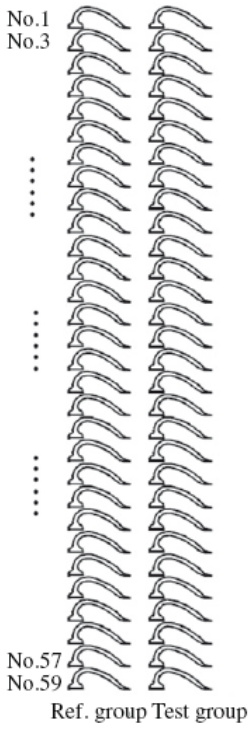

Figure 20: Bonding diagram for measuring online FAB deformability [42].

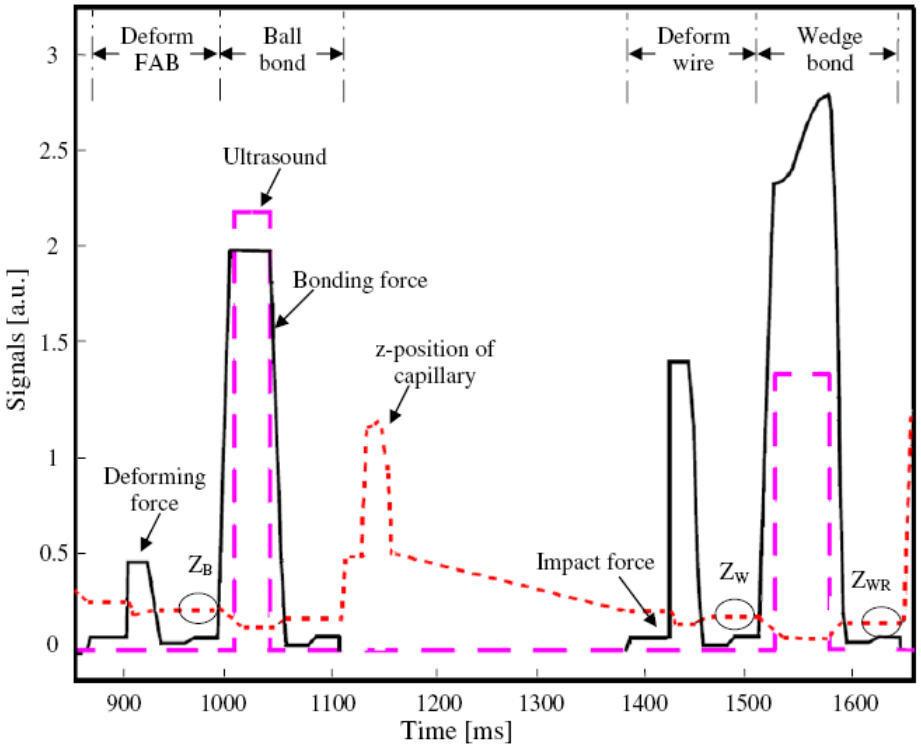

Figure 21: Representative signals for z-position, force, and ultrasound provided by bonder. Periods for Z_B, Z_W, and Z_{WR} evaluation indicated by circles. Period for Z_{BR} evaluation obtained from reference wedge bond (not shown) [40].

1.6.1.1 Characterizing the Influence of Ultrasound on Deformability

A modified version of the online deformability method [34, 45] is used to identify the effects of US on the hardness and deformability of the FAB. The temporary acoustic softening effect on the FAB is quantified by simply applying US during the deformation step of the online deformability measurement, as illustrated in Fig. 22 [34]. The residual acoustic softening effects on the deformability of the FAB is quantified by adding a second step (Step 2) where the deformed ball is deformed a second time as illustrated in Fig. 22 [34]. The effects of US on both the deformed Cu ball heights H_1 and H_2 are shown in Fig. 23 and Fig. 24, respectively[34]. The temporary acoustic softening and residual softening effects increase with increasing US power for both Cu and Au FABs [34, 45].

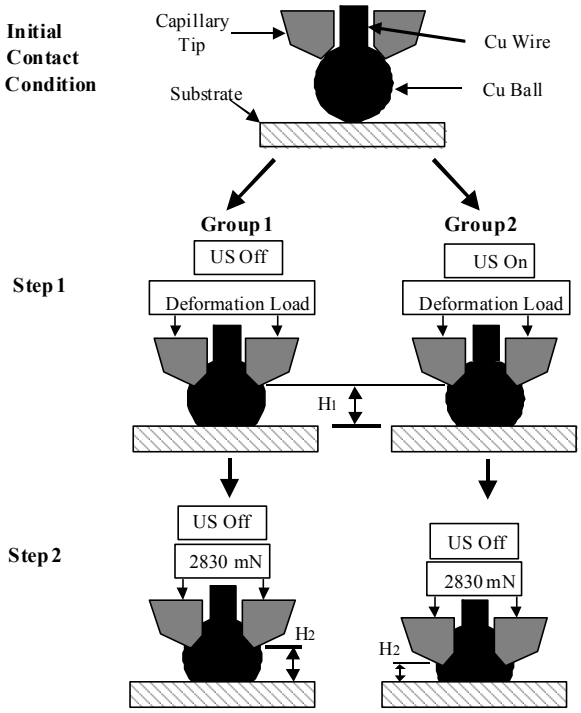

Figure 22: Illustration of a modified online deformability method that is used to characterize the temporary acoustic softening effects (Step 1, Group 2) and the residual acoustic softening effects of applying US during initial deformation (Step 2, Group 2) [34].

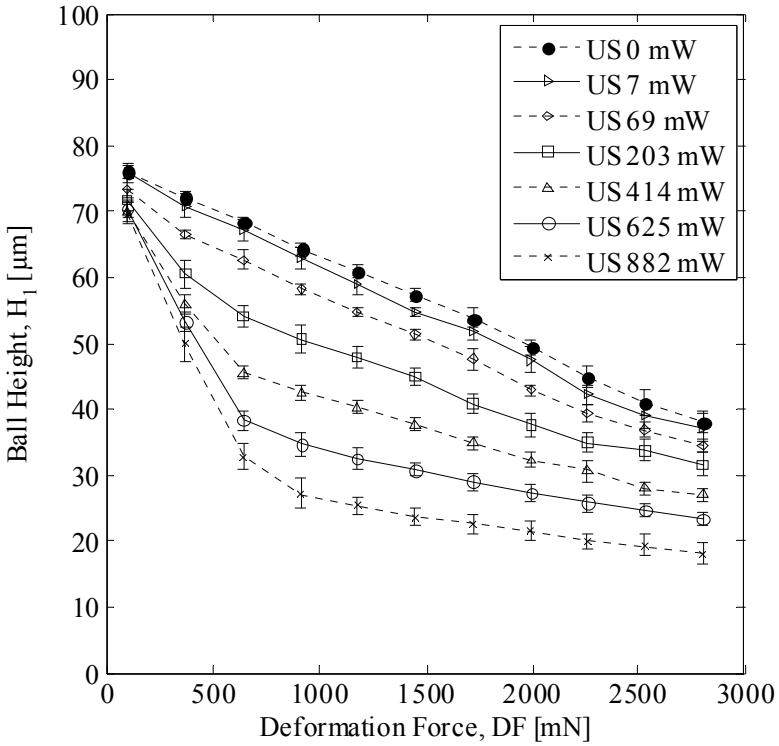

Figure 23: Temporary acoustic softening effect on Cu FABs. Effect of increasing US power on ball height H_1. Error bars indicate standard deviation [34].

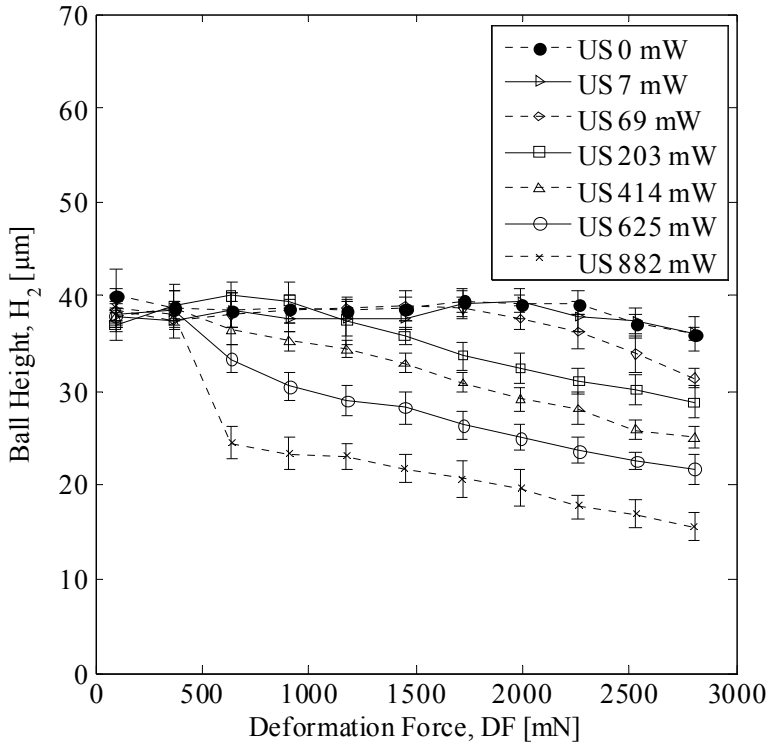

Figure 24: Residual acoustic softening effect on Cu FABs. Effect of increasing US power on ball height H_2. Error bars indicate standard deviation [34].

1.6.2 Online Tail Breaking Force Measurement

The formation of a consistant tail is essential for reliable high yield ball bonding. The TBF must be strong enough so that the tail bond illustrated in Fig. 25 does not break until the capillary moves upwards to the correct position [41]. If the tail bond is too weak the tail length will be in-consistent or the wire will be blown out of the capillary and the wire must be re-threaded causing stoppages in production. The TBF is measured online during bonding by measuring the change in the signal provided by the proximity sensor as the clamp deflects due to tension in the wire up until the tail bond breaks. Example signals from the proximity sensor are shown in Fig. 26 a) and b). Fig. 26 b) shows the proximity signal when the tail bond is broken [41].

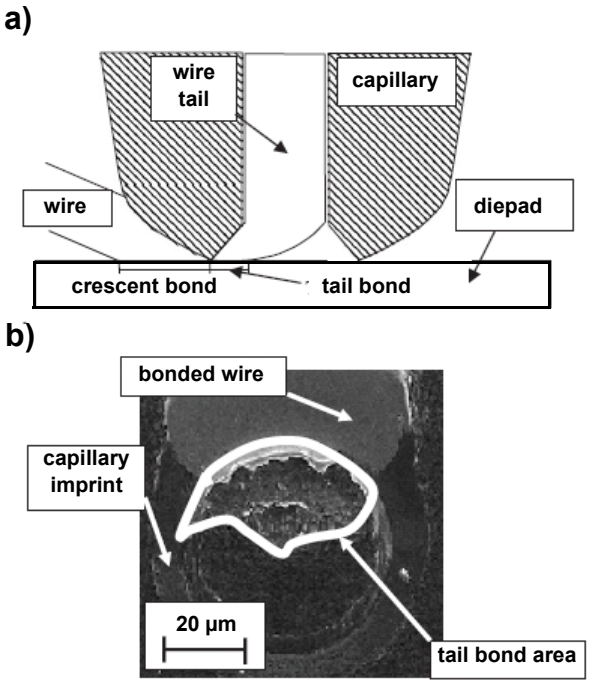

Figure 25: Illustration (a) and SEM image of tail bond (b) [41].

1.6.3 Online Heat Affected Zone Breaking Force Measurement

A short and strong HAZ is often required for advanced microelectronic packaging. If the HAZ is too long or very weak low loop heights that are necessary for decreasing package thickness can cause the wire to break during looping. The wire type and EFO parameters both affect the HAZ length and strength [32, 42]. It has been shown that larger I_{EFO} applied for shorter t_{EFO} produce a stronger HAZ during Cu wire bonding as shown in Fig. 27. This was shown to be a result of larger grain sizes produced during longer t_{EFO} [42, 43].

Similarly to the online TBF measurement the HAZ breaking force is obtained from the change in the proximity sensor signal as the clamp deflects. A ball bond is made followed by the closing of the wire clamp and the upward motion of the bondhead causing the wire to break in the HAZ. Fig. 28 shows a SEM image of a Cu ball bond after the online HAZ breaking force measure-

ment [42]. An example of the proximity sensor signal during the online measurement of the HAZ breaking force is shown in Fig. 29 [42].

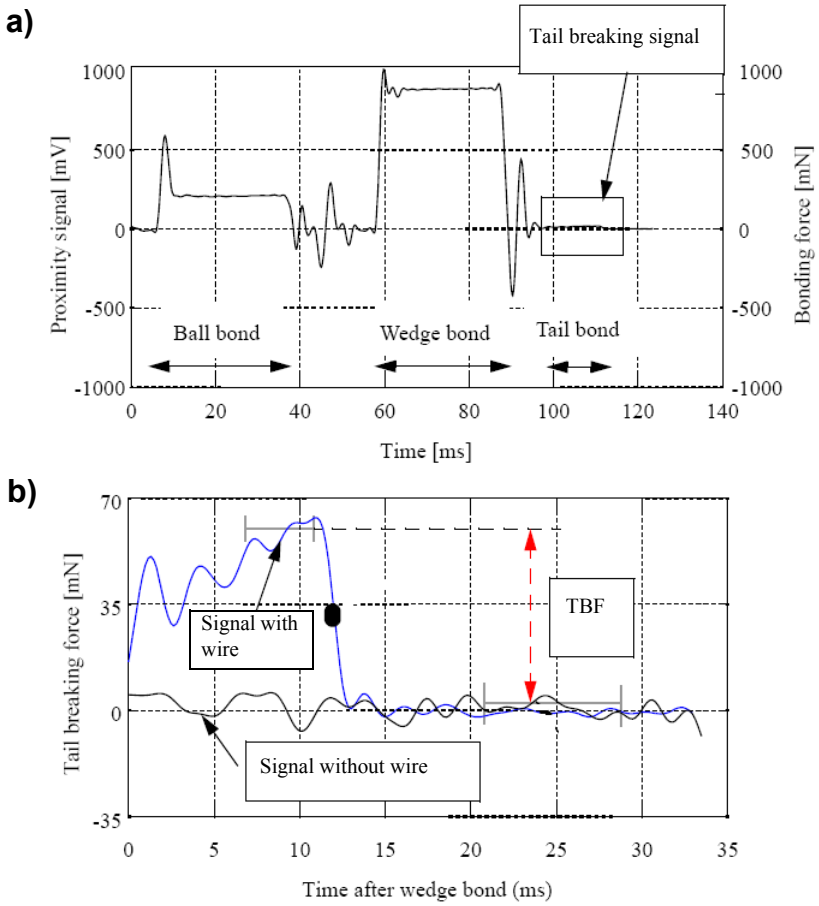

Figure 26: Proximity sensor signal: a) during one bonding cycle and b) during tail break.

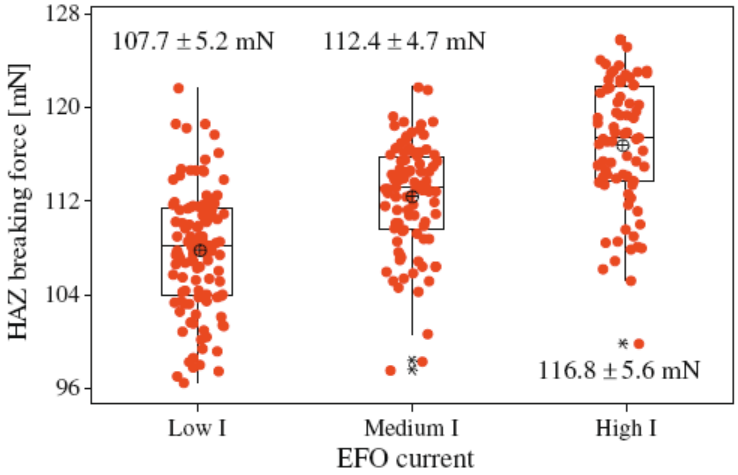

Figure 27: HAZ breaking force obtained from online measurement. Low I_{EFO} = 45 mA, t_{EFO} = 0.9 ms. Medium I_{EFO} = 80 mA, t_{EFO} = 0.39 ms. High I_{EFO} = 250 mA, t_{EFO} = 0.11 ms [42].

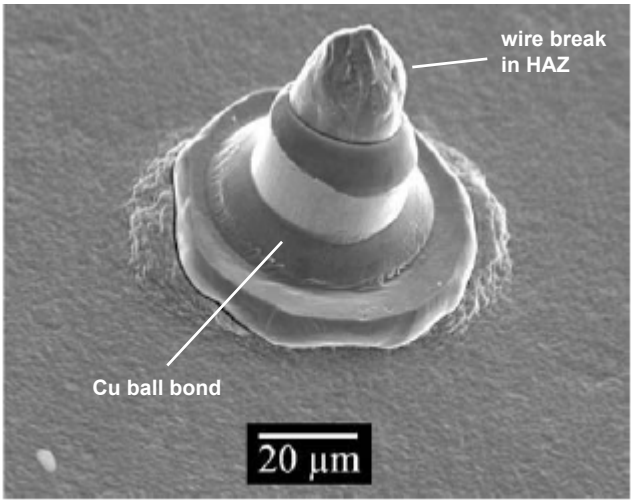

Figure 28: SEM image of Cu ball bond after HAZ breaking force measurement [42].

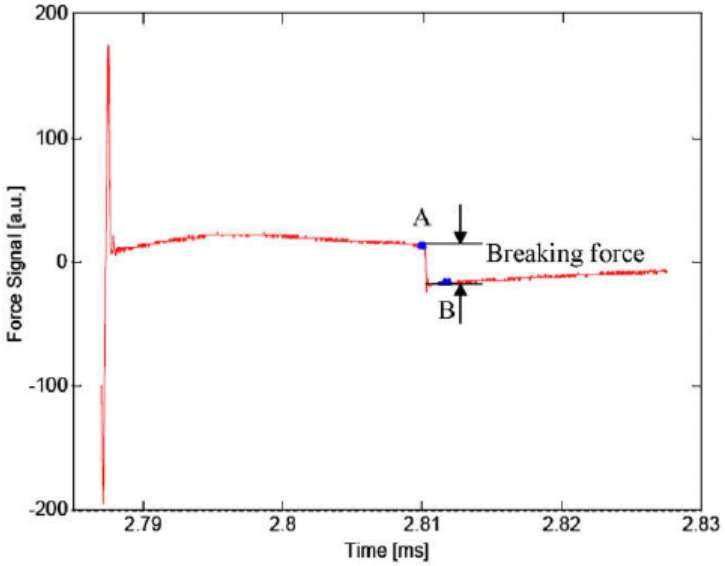

Figure 29: Proximity sensor signal during online HAZ breaking force measurement [42].

1.7 Bonding Wire Materials

The wire bonding technology has continuously evolved to meet the demands of the modern device while remaining the cheapest first level interconnect technology [1]. A modern approach for meeting the industry demands for higher performance, lower costs, and miniaturization is the development of new wire types and materials. The most promising of which being Cu, and insulated bonding wire materials. Although there are many advantages of these novel wire materials there are also some challenges that must be addressed before they will be fully accepted in many applications.

1.7.1 Copper Bonding Wire

Copper bonding wire has become a very promising alternative to the conventional Au wire due to its potentials for economical and performance advantages. Relative to Au wire, Cu has superior electrical and thermal conductivities as well as higher tensile strength and elongation. A comparison of Cu and Au properties is shown in Table 1.

Table 1: Comparison of Copper and Gold bonding wire material properties.

Properties	Wire Material	
	Gold (Au)	Copper (Cu)
Electrical Conductivity [Ω m][a]	4.55×10^7	5.88×10^7
Thermal Conductivity [kW/m^2K][a]	31.1	39.5
Tensile Strength [MPa][b]	135	210-370
Modulus of Elasticity [MPa][b]	79 000	123 000
Elongation to Failure [%][c]	2-8	4-18
Wire Hardness [HV][c]	50	57

[a]Ref. [47]
[b]Ref. [1]
[c]Ref. [35]

1.7.1.1 Advantages of Cu Bonding Wire over Au

The 23 % higher electrical conductivity and 21 % higher thermal conductivity of Cu makes it an excellent wire material for high performance applications that require wire bonds with high current carrying capacity. The higher thermal conductivity also leads to a shorter and stronger HAZ improving performance during looping [47].

The higher tensile strength and modulus of elasticity of Cu allows for longer distances between the first and second bonds having greater resistance to wire sag and wire sweep during encapsulation of the package [1, 2, 5, 18, 47]. Wire sweep caused by the viscus flow of the encapsulant is shown in Fig. 30. Wire sag and wire sweep become a major issue with finer pitch applications and in extreme cases lead to electrical shorting and device failure.

The Cu wire-Al bondpad system is more reliable than the Au wire-Al bondpad system which is the standard in the microelectronics industry [47]. Even though there are five possible Cu-Al intermetallics it is found that they grow at less than half the rate of the Au-Al intermetallics [48].

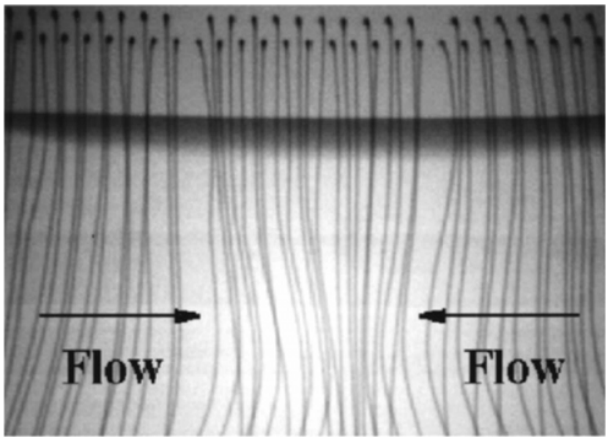

Figure 30: X-ray image of wire sweep during molding of package with encapsulant. Wires sweep and in some areas may even touch causing electrical shorts.

The growth of the intermetallic layer at various temperatures is shown in Fig. 31 a) and b) for the Cu-Al and Au-Al systems, respectively [48]. It is also found that Cu oxide helps improve reliability by preventing or inhibiting the growth of Kirkendall voids [2, 49].

In addition to the performance advantages of Copper wire, there is also a significant economical advantage when compared to Au wire. Cost savings are the most significant driving force in semiconductor assembly [47]. Copper is cheaper than Au and due to its superior tensile strength, elastic modulus, and electrical and thermal conductivities, thinner wires and therefore less material can be used for each device [47].

1.7.1.2 Challenges of Copper Wire Bonding

Despite all of the advantages of Cu wire there are two main drawbacks that have retarded its replacement of Au wire. Copper wire is harder than Au wire and it oxidizes readily in air. As a result of the higher hardness of Cu wire, larger deformation forces and US levels are required for

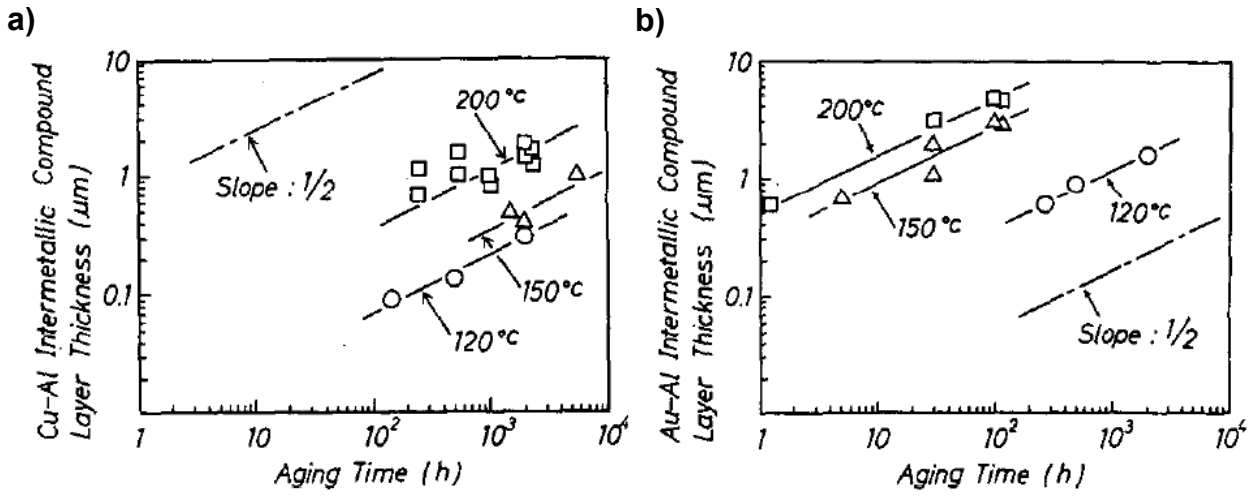

Figure 31: Relationship between intermetallic compound layer thickness and time for a) the Cu-Al system and b) the Au-Al system when aged at various temperatures ranging from 120-200 °C [48].

bonding [2, 17, 50, 51]. Larger bonding forces and US levels lead to an increase in the likelihood of underpad damage such as cracking, delamination, and underpad cratering [2, 17]. The relationship between the occurrence of underpad damage and bonding load and US level is shown in Fig. 32 a) and b) [17]. The underpad stresses during Cu wire bonding are 30 % higher than in Au wire bonding [50, 51]. Cracks and cratering refer to damage to the passivation and silicon underneath bond pad metallization. They cause electrical degradation and reduced reliability of the device [18]. Underpad cracks and cratering are illustrated in Fig. 33 a) and b), respectively [17]. The

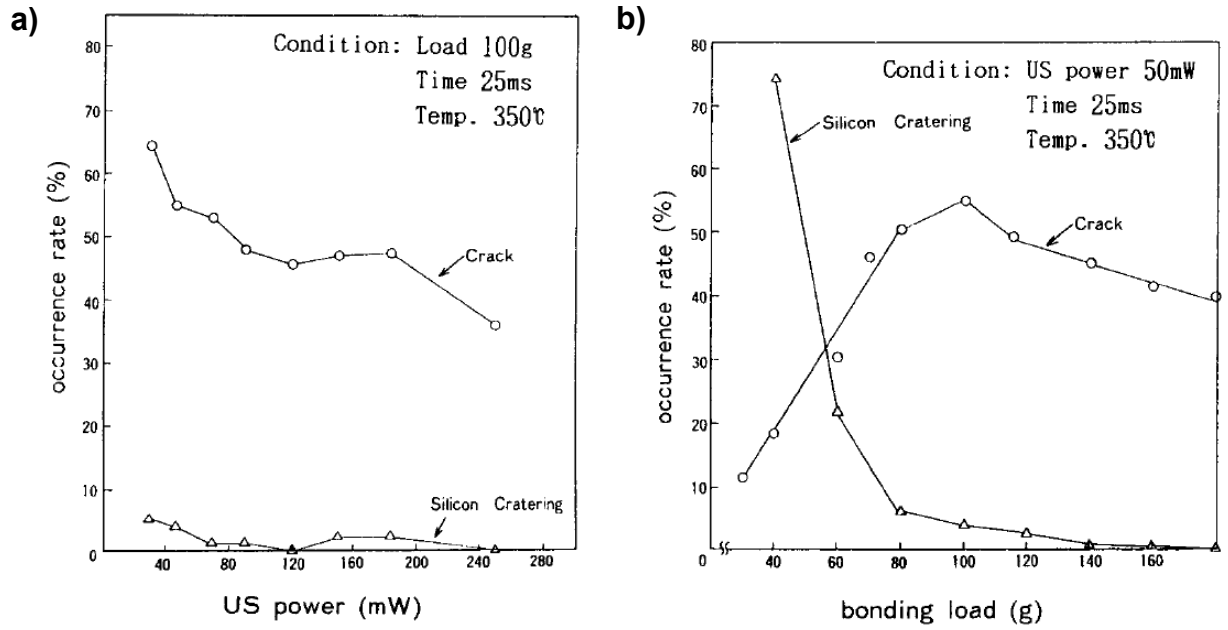

Figure 32: a) Chip damage vs. US power for conventional copper wire bonding, b) chip damage versus bonding load for conventional coper wire bonding [17].

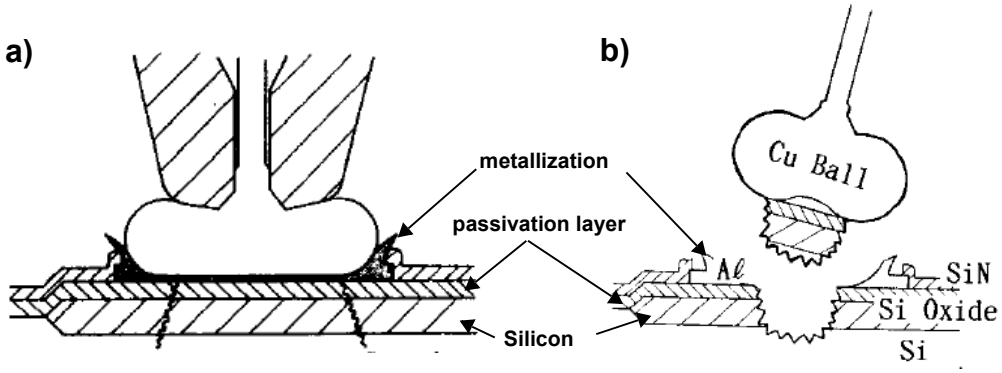

Figure 33: Illustration of underpad cracking (a) and cratering (b) caused by the ball bonding process [17].

higher bonding forces and US levels makes bonding to ICs produced from low-*k* materials very challenging [52, 53]. As the microelectronic industry moves towards higher performance ICs and spacing between interconnect lines decreases, low-*k* dielectrics are becoming more popular. Low *k* value dielectric materials are required to overcome the signal delays that result from the higher resistance and capacitive coupling associated with less spacing between the interconnect lines on the IC [53, 54]. Low *k* materials have high porosity and therefore lower strength which can result in easy chip damage.

There are many complications associated with the oxidation of the Cu wire. Copper oxide degrades bond quality, causes FAB defects, increases the hardness of the FAB, and reduces the shelf life of the wire. Oxidation at the interface between the Cu and metallization degrade bond quality by preventing intimate contact between the bare wire and metallization materials as discussed in section 1.5.3.1. Oxidation becomes more of an issue during EFO due to the high temperatures. Excessive oxidation during EFO leads to FAB shape defects such as golf-clubbed and pointed FABs. Since Cu oxide builds up over time the shelf life of the Cu wire is limited. The second bond strength will degrade and tailing issues will begin to occur as the Cu oxide reaches a certain thickness. Due to the shorter shelf life of Cu wires, less wire can be put on a spool than for Au wire meaning the spools must be changed more frequently and more attention is required for planning wire inventory to prevent waste.

As discussed in section 1.3.1.3 a protective gas atmosphere is required during EFO in order to prevent oxidation of the Cu FAB. The wire bonder must be retrofit with a Cu kit in order to be able to bond with Cu wire. The 5 % H_2 + 95 % N_2 forming gas required to produce spherical, oxide

free Cu FABs is an additional expense to the wire bonding industry. Also, gas mixtures containing larger than 5 % H_2 are considered flammable and are undesirable due to safety and handling purposes [18]. Setting up a wire bonding manufacturing facility to handle forming gasses safely will therefore require a large initial investment.

1.7.2 Insulated Bonding Wire

As the microelectronics industry moves towards high input/output (I/O) density devices, creating electrical interconnects via wire bonds becomes increasingly challenging [6, 53, 55]. In order to achieve high I/O density, higher pin count, finer pitch, multi-row, and multi stack devices are required. With these new device designs, shorting of the wire bonds becomes a major issue which increases device failure and decreases process yield. The wires must span longer distances and thinner wire diameters are required which increases the severity of wire sweep and sag. Two methods in preventing shorting due to wire sweep and sag are by modifying loop profile and using stiffer wire materials. Adding additional kinks to the wire loop and stiffer wire such as Cu or Au alloy materials help reduce wire sweep and sag [55, 57]. A third method is to use Au insulated bonding wires such as X-wire^{TM} developed by Microbonds Inc., Markham, Ontario, Canada. These commercially available insulated wires eliminate the risk of shorting all together.

The X-wire^{TM} insulated wire technology utilizes a sub-micron thick dielectric organic coating to prevent electrical shorting. The coating process is an additive process meaning that any base wire material can be coated [6]. This insulated bonding wire technology was identified on the 2006 ITRS Roadmap for Semiconductors as a viable, cost effective solution to enable complex package designs, enhance package performance, and improve the yield of high-density packaging

[6]. It has been demonstrated that the insulated Au wire can be used to bond long wire loops such as in stack die, high density milti-tier, and same-tier crossed wire applications without electrical shorting as shown in Figs. 34 a), b) and c), respectively [55].

1.7.2.1 Performance Requirements of Wire Insulation

The performance requirements for developing a new insulation include: reliable and quality FAB, bond strength/reliability, dielectric strength, robustness of coating during process, limited effect on base material properties, resistances to common solvents, resistance to high subsequent processing temperatures, no contamination of capillary, and toxic-free during EFO [6, 53, 55, 56].

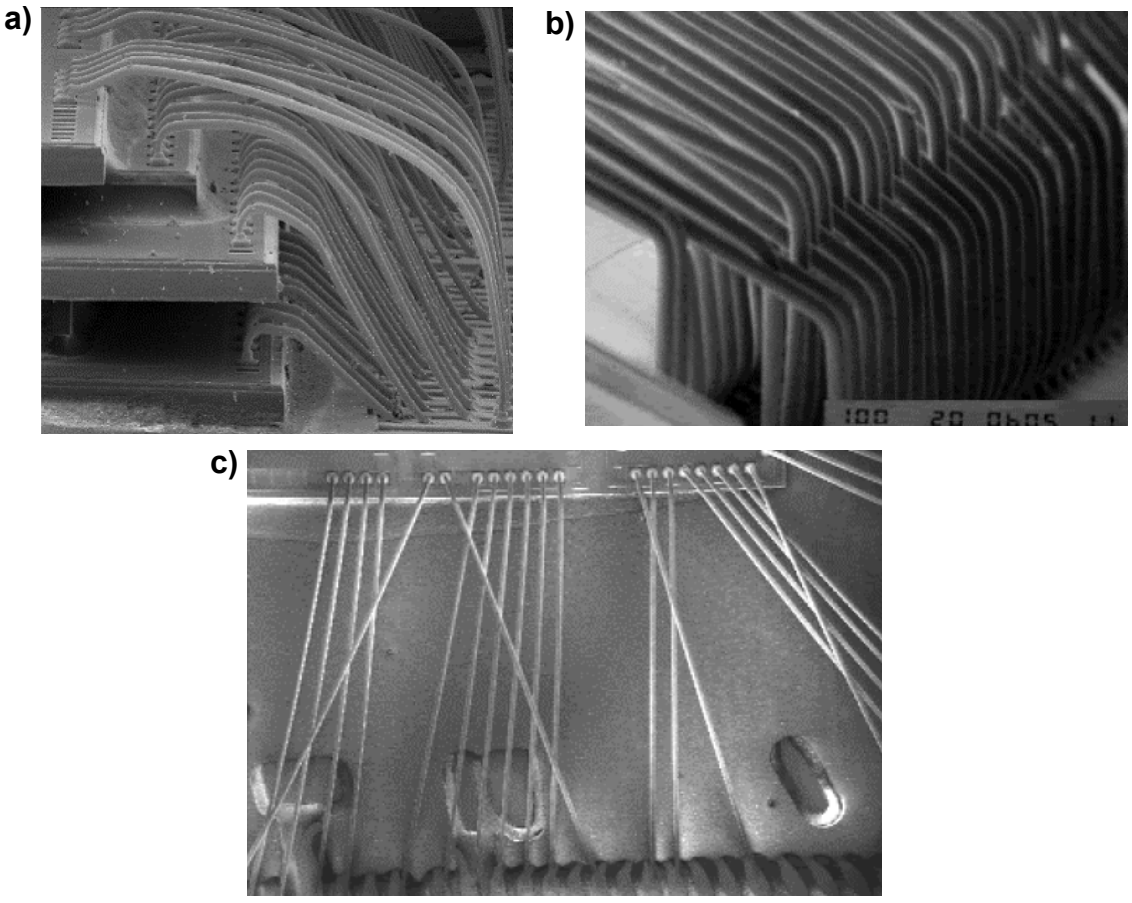

Figure 34: Applications of insulated Au wire with no risk of electrical shorting: a) stack die, b) high density multi-tier, and c) crossed wire same-tier [55].

In addition to performance requirements the insulating process must be low cost and the current wire bonding equipment must be easily adapted to support insulated wires.

The Au X-wire^{TM} insulation meets industry requirements. During EFO the insulation is removed from the bottom of the FAB and remains on the wire due to the higher melting point of the insulation than the base wire material [53]. The FAB has the characteristic "Water-Melon" stripe appearance as shown in Fig. 35 where no coating is present at the bottom of the FAB and hence, ball bond performance is equal to that of the bare wire [55]. The insulation has a breakdown voltage that exceeds 25 V, no cracks occur if bent to a radius of smaller than 25 μm and the thermal properties and HAZ properties are similar to those of the base metal [32]. Negligible contamination of the capillary is found after making over 1 million wire bonds as shown in Fig. 36. It was also found that during EFO acceptably low levels of volatile organic compounds (VOC) where released into the air [55].

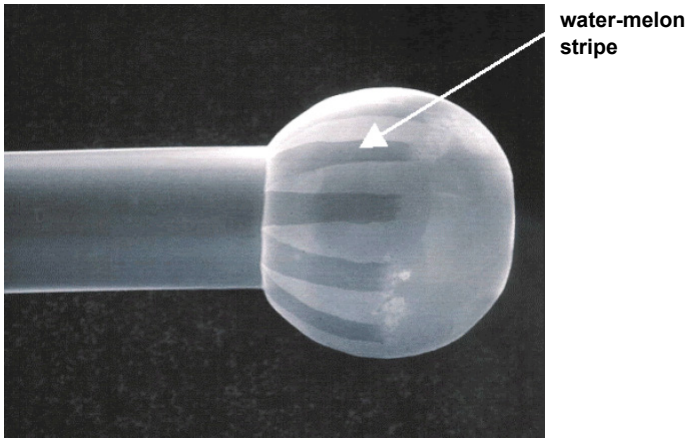

Figure 35: Water-Melon stripe effect, characteristic of the Au X-wire^{TM} FAB. No insulation is present on the portion of the FAB to be bonded [55].

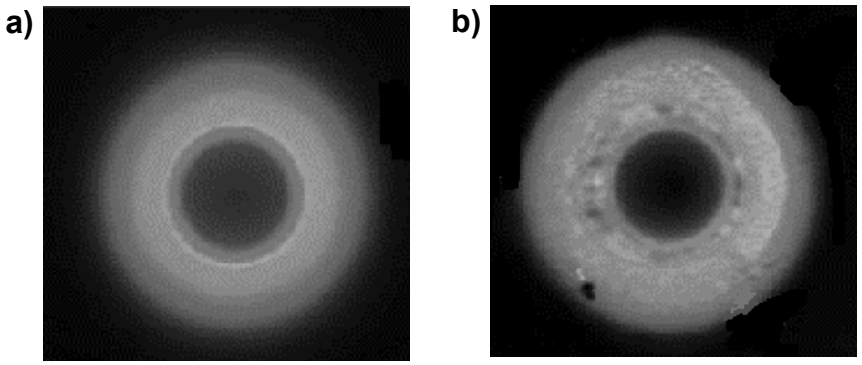

Figure 36: Negligible contaminants found on the capillary tip caused by bonding with insulated bonding wire: a) new capillary (zero bonds), and b) capillary tip after over 1 million bonds [55].

1.7.2.2 Challenges of Insulated wire Bonding

The main challenges associated with bonding insulated wire are forming a good quality FAB, preventing damage to the insulation on the wire during EFO, and making strong second bonds with no wire open stoppages (i.e. good tailing). The performance of an insulated wire depends on both the chemistry of the insulation and its thickness. For example some chemistries burn off more easily allowing for better FAB formation and some are thinner and more brittle and therefore break up and are displaced easily while making the second bond. One of the challenges associated with the development of the insulation is that there is always a compromise between the performance of the wire in one area versus another with varying chemistries and coating thicknesses.

During the EFO process with an insulated wire it is important to ground the end of the wire to prevent the current from jumping to ground though the insulation layer for example at the wire clamp, burning a hole in the insulation layer [6, 53]. Most of the modern wire bonders come with a ground connection near the wire spool. All other wire bonders must be equipped with a low-cost upgrade [6].

The optimization of the EFO parameters can be quite different than for bare non-insulated wire. The first difference is that the insulation slows the cooling of the molten metal during FAB formation and/or increases the plasma temperature resulting in larger FABs than for non-insulated wire [32]. It is also found that the discharge gap can be shorter during EFO and a shorter gap is even sometimes necessary to form good quality FAB. As mentioned in section 1.5.3.1 the correct amount of energy is required to burn off the insulation. Therefore the EFO parameters must be selected more carefully making sure that the coating is fully removed unlike the on the FABs shown in Fig. 15. Insulation remaining on the bottom portion of the FAB which is to be bonded to the metallization acts as a contaminant and degrades the quality of the bond.

The second bond is a weak point in the wire bonding technology. Approximately 80 % of the pull strength of the non-insulated wire bonds can be obtained using conventional second bond techniques [58]. New techniques are required to obtain pull strengths comparable to non-insulated wire and to promote good tailing with no open wire stoppages during production. Some of these techniques include: i) high initial bonding force applied with high strain rate in order to crack the insulation coating, ii) low force scrubbing, and iii) applying a shift part way through bonding in order to scrape the wire along the bonding surface [55, 58]. An example of using such techniques is shown in Fig. 37. Using this bonding process the wedge bond pull strength was found to be comparable to that of the non-insulated wire bonds [58]. The main drawback to such a bonding process is that the bonding time is increased, decreasing the manufacturing throughput.

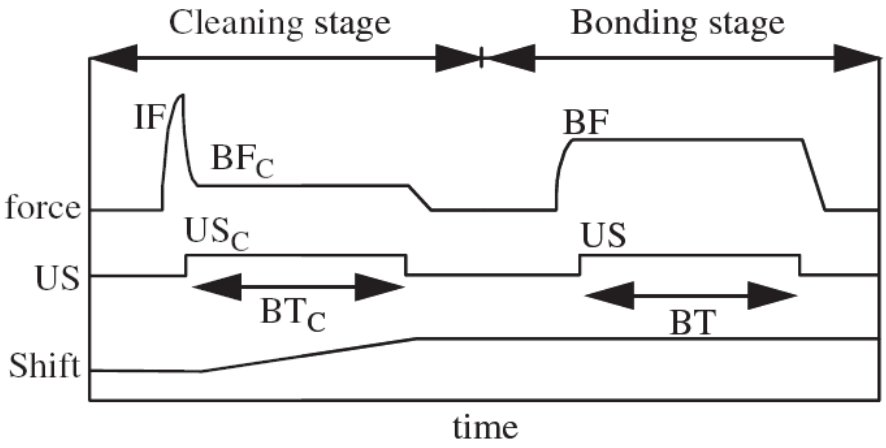

Figure 37: Modified bonding process with cleaning stage for bonding with insulated Au wire. Comparable bond strength to non-insulated wire bonds is achieved using this process [58].

1.7.2.3 Insulated Cu Wire

The future of insulated wire bonding could be insulated Cu wire materials. By insulating Cu wires the superior electrical, thermal, and mechanical properties of the Cu wire is combined with the advantages of insulated wire. The insulation will prevent oxidation of the wire increasing the shelf life of Cu wire. It is also thought that the gases produced during EFO as the insulation is burnt off could act as a protective atmosphere preventing oxidation of the FAB. Forming Cu FABs in N_2 gas or air could then be possible. This would be a huge advance in Cu wire bonding where forming gas mixtures of H_2 and N_2 are no longer necessary to form quality FABs. However, the effect of the gas atmosphere on the EFO discharge must first be better understood.

2.0 Effect of Electrical Flame Off Parameters on FAB Hardness and Work Hardening

The likelihood of underpad damage caused during the wire bonding process increases when bonding with Cu wire. This is especially true when bonding to devices that contains low-*k* dielectric materials. The most common type of underpad damage produced by these stresses are pad peeling, cracking, cratering, or dielectric layer delamination. During wire bonding both compressive forces and cyclic shear forces act on the bond pad due to the bonding force and US, respectively [50, 51]. With a harder FAB higher bonding forces and US levels are required for making the ball bond leading to larger stresses on the device [2].

There are several different approaches in reducing underpad stress and therefore limiting damage during thermosonic bonding with Cu wire. Some approaches to reducing underpad damage are by using softer wire, producing softer free air balls (FABs), optimizing the bonding parameters, and even by changing the bond pad design or material [2, 38, 50]. Electrical flame off parameters and the temperature of the shielding gas can be changed to produce Cu bonded balls and Cu FABs with different hardness [38, 59]. The microhardness of the bonded balls (BBs) has been investigated extensively in Ref. 38. It was concluded that the BB hardness decreases with increasing I_{EFO} with t_{EFO} adjusted to leave the FAB diameter constant. The amounts of US effects and work hardening were not discussed. Possible US effects include acoustic softening and residual hardening that have both been observed in metals that are subject to US energy [29, 34, 44, 45].

In this chapter the effects of EFO parameters on the hardness of FABs are examined. By performing manual microhardness tests and an online deformability study [40] the FAB is characterized before bonding takes place. This eliminates the US effects from the experiment.

2.1 Experimental Procedure

The wires selected for this study are standard 25 µm diameter Au and Cu wires manufactured by MK Electron Co. Ltd., Yongin, Korea. The basic mechanical properties are outlined in Table 2. The wire Vickers hardness is measured on cross-sections orthogonal to the wire axis as shown in Fig. 16 a).

The EFO parameters are determined that will produce 50 ± 1.0 µm diameter FABs for both the Au and Cu wires. In order to find these parameters a total of 30 FABs are measured using three different EFO times (10 FABs for each EFO time) while holding the other EFO parameters constant. A shielding gas of 5 % H_2 + 95 % N_2 with a flow rate of 0.5 l/min is used for Cu wire bonding to prevent the oxidation of the molten Cu during EFO [40]. The gas flows through a tube of 1 mm diameter. A flow rate of 0.5 l/min therefore corresponds to a flow speed of 10.6 m/s. The Cu FABs are examined using a Joel JSM-6460 scanning electron microscope (SEM) to ensure the flow rate of the shielding gas is sufficient to prevent oxidation during EFO. The FAB diameters are measured using an optical microscope and fitted to a second order polynomial as shown for the Cu wire at the high I_{EFO} level in Fig. 38 [50]. This method is performed for each of the low, medium and high I_{EFO} of 45 mA, 80 mA, and 250 mA, respectively. The I_{EFO}, t_{EFO} and the average FAB diameters obtained are presented in Table 3 for the Cu and Au wire, respectively. For a 50 µm FAB

Table 2: 25 µm (1 mil) diameter wire properties.

Property	Cu	Au
Minimum Breaking Load [mN]	49	98
Elongation [%]	4-18	2 - 8
Vickers Hardness	57.8	50.0

produced with I_{EFO} = 45 mA, the t_{EFO} for Cu is 44 % larger than that required for Au. The difference is possibly due to the superior thermal conductivity of Cu. However, as I_{EFO} is increased the difference in the required t_{EFO} between the Cu wire and Au wire decreases. At an I_{EFO} of 250 mA the t_{EFO} required for the Cu FABs is only about 7% larger than that for the Au FABs. Possibly, the rate and magnitude of heat input is large enough at higher current levels to render the heat conducted away through the wire insignificant.

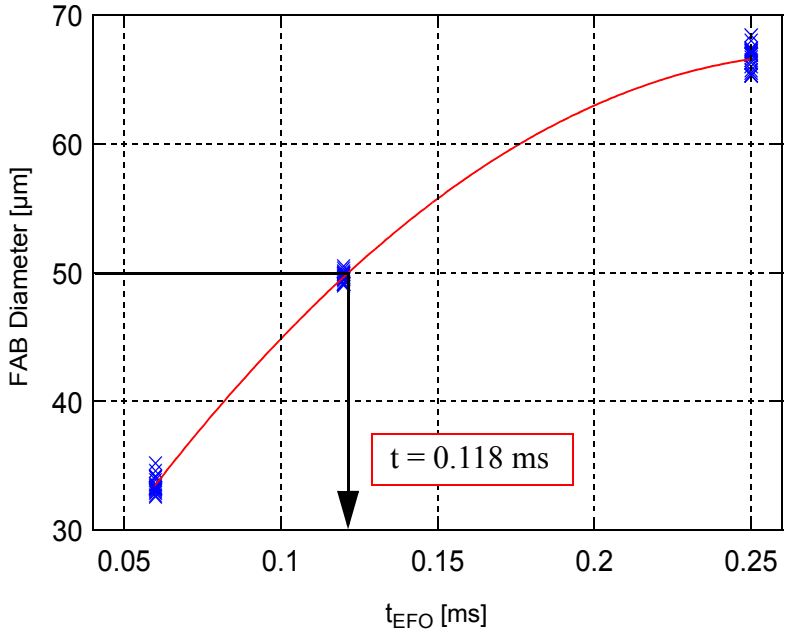

Figure 38: FAB diameter vs. t_{EFO} for Cu wire. The solid line represents a polynomial curve fit. The I_{EFO} = 250mA in this example.

Table 3: Electrical flame off parameters and resulting FAB sizes.

	Cu			Au		
	Low Current	**Medium Current**	**High Current**	**Low Current**	**Medium Current**	**High Current**
EFO current [mA]	45	80	250	45	80	250
EFO time [ms]	1.03	0.43	0.118	0.58	0.3	0.11
Avg. FAB diameter [µm]	49.64 ± 0.44	49.74 ± 0.53	49.74 ± 0.38	49.98 ± 0.42	49.99 ± 0.48	50.27 ± 0.73

2.1.1 Online Free Air Ball Deformability Measurement

The online deformability method as described in section 1.4.1 was performed on a Ag plated Cu leadframe shown in Fig. 39 using an automated Besi Esec 3100 thermosonic wire bonder, shown in Fig. 17. An encoder measures the bondhead position with sub-micron precision along the z-axis. The z-position of the capillary tip is derived from this encoder measurement and recorded during bonding. These signals are used to determine the deformed ball height (BH). The deformed BH is representative of the deformability of the initial FAB [40]. The deformability depends on material hardness and work hardening. FABs produced using low, medium, and high I_{EFO} are deformed using a deformation force of 0.6 N. The signals recorded during bonding are shown in Fig. 40. The deformed BH is measured after deformation with the 0.6 N deformation force.

2.1.2 Vickers Hardness Measurement

The next step is to compare the online deformability results to microhardness measurements made in the center of the polished cross-sections of FABs as shown in Fig. 41 and in the center of the cross-sections of BBs as shown in Fig. 42. The hardness measurements were performed using a LECO DM-400LF hardness tester with Vickers indenter applying a 49 mN (5 gf) load with a 15 s dwell time.

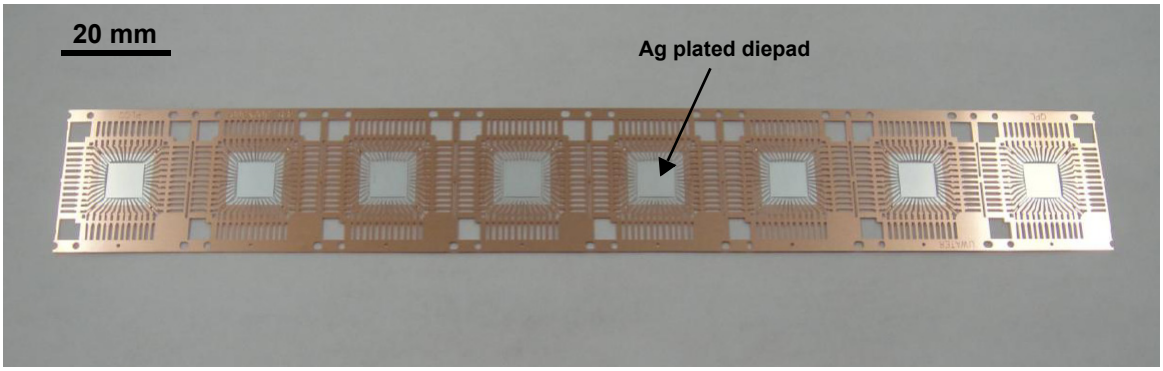

Figure 39: PLCC44 Ag plated Cu leadframe. All bonding was performed on Ag plated bondpad.

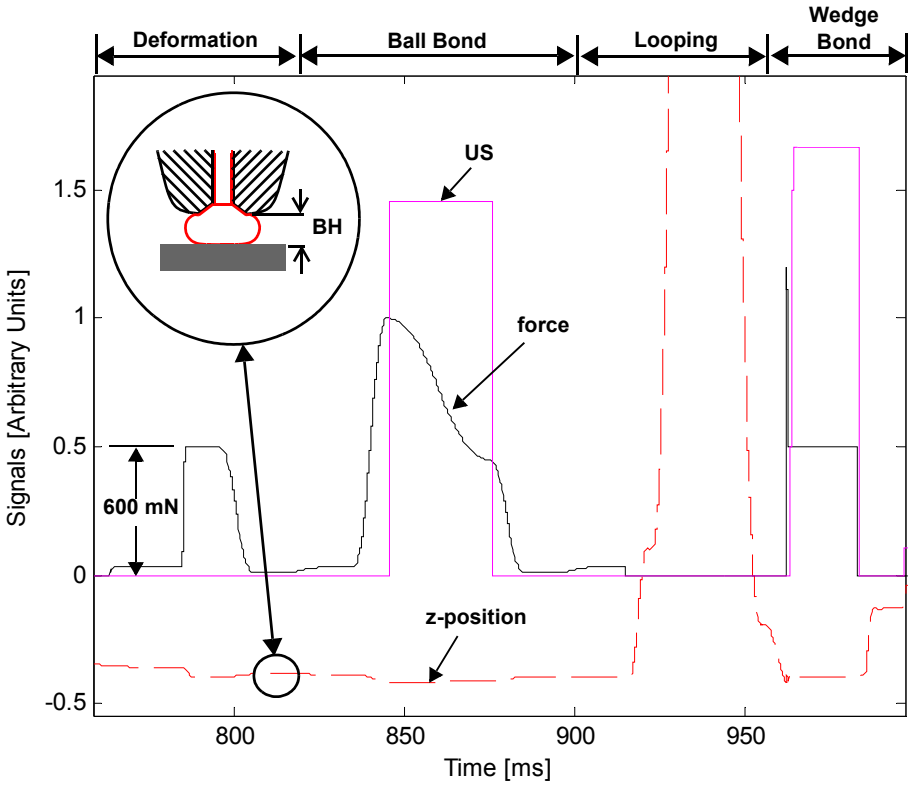

Figure 40: Force, US, and z-position signals recorded during online deformability measurement. The force and z-position signals are the actual recorded signal. The US is the control amplitude that the real A.C. US tries to follow.

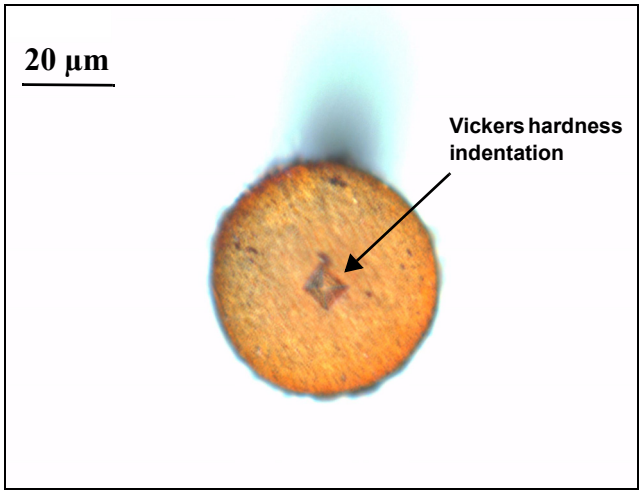

Figure 41: Cross-section of a Cu FAB with Vickers hardness indentation.

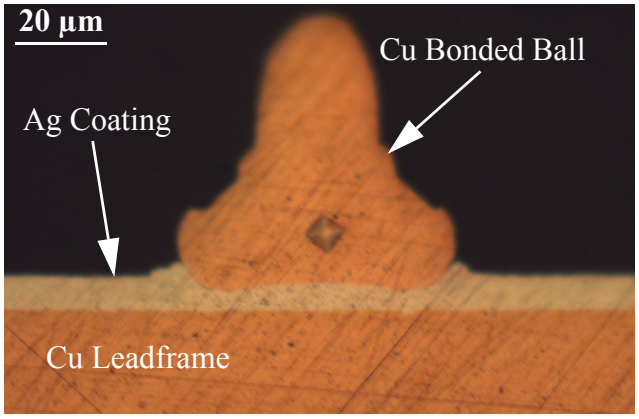

Figure 42: Cross-section of a Cu BB with a Vickers hardness indentation.

2.2 Online Free Air Ball Deformability Measurements

Deformability results are shown in Fig. 5, where the BH decreases as the I_{EFO} increases. The average BHs and their associated errors are shown in Table 4 for both Au and Cu at each of the I_{EFO} levels. The amount of deformation increases with increasing the I_{EFO} for both Au and Cu.

The online deformability results are consistent with BB microhardness results from Ref. 38, which were subject to US energy. Both the online deformability study and Ref. 38 suggest that FABs produced with a higher I_{EFO} and lower t_{EFO} will have a lower hardness. However, no

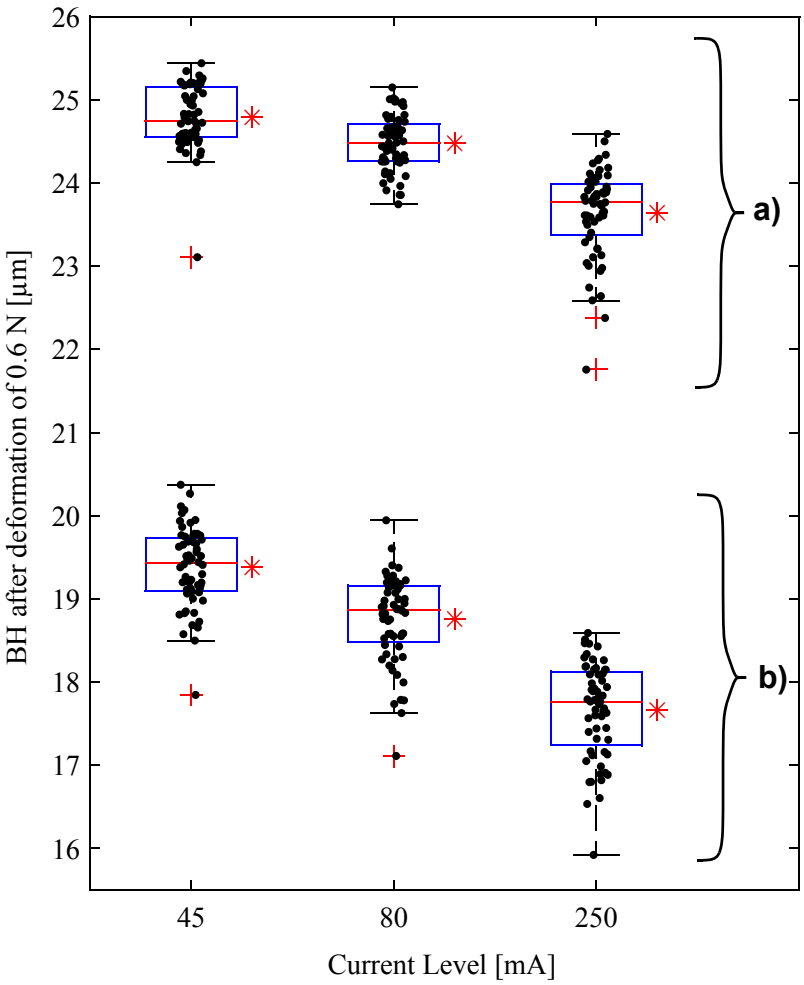

Figure 43: Online deformability results for Au and Cu 50 µm diameter FABs. a) Cu BH after deformation, b) Au BH after Deformation. Mean values are represented by star symbols.

conclusion regarding the FAB hardness before deformation can be made as of yet. In order to reach such a conclusion, the amount of work hardening needs to be characterized.

Table 4: Average BHs and error values from online deformability study.

	Current Level		
	45 mA	**80 mA**	**250 mA**
Au BH [μm]	19.38 ± 0.06	18.76 ± 0.07	17.66 ± 0.07
Cu BH [μm]	24.79 ± 0.05	24.48 ± 0.04	23.64 ± 0.07

2.3 Free Air Ball Microhardness

During EFO, the wire end is heated until molten into a droplet of desired diameter. The longer t_{EFO}, the more the wire adjacent to the droplet is heated, resulting in a larger heat affected zone (HAZ). While heat is radiated and convected to the atmosphere, the main driver for the solidification after EFO is the heat conducted to the unmolten wire [60]. In the case of the higher I_{EFO} value coupled with the shorter t_{EFO}, it is expected that the droplet peak temperature is higher [38], followed by higher cooling rates and gradients. The resulting FAB is expected to have a higher residual stress, dislocation density, and therefore hardness.

The Cu FAB microhardness results presented in Fig. 44 and Table 5 confirm this reasoning. Cu FABs produced with the lower I_{EFO} (45 mA) have a substantially lower microhardness (14.29 HV lower) than that of FABs produced with the higher I_{EFO} (250 mA). However, considering the Au FAB results in Fig. 44 and Table 5, it is found that there is no significant hardness difference of the Au FABs with 95 % confidence as shown by the t-test results in Table 6. This might be due to the fact that between FAB solidification and microhardness testing, the FABs are subject to elevated temperatures. Bond-offs are made to a 220 °C hot substrate with the FABs

Table 5: Average FAB and BB Vickers hardness.

	Current Level		
	45 mA	**80 mA**	**250 mA**
Au FAB [HV]	45.34 ± 0.53	44.59 ± 0.91	47.63 ±1.07
Cu FAB [HV]	67.46 ± 0.95	78.45 ± 0.58	81.75 ± 0.71
Cu BB [HV]	105.66 ± 0.98	102.27 ± 0.85	101.39 ± 0.71

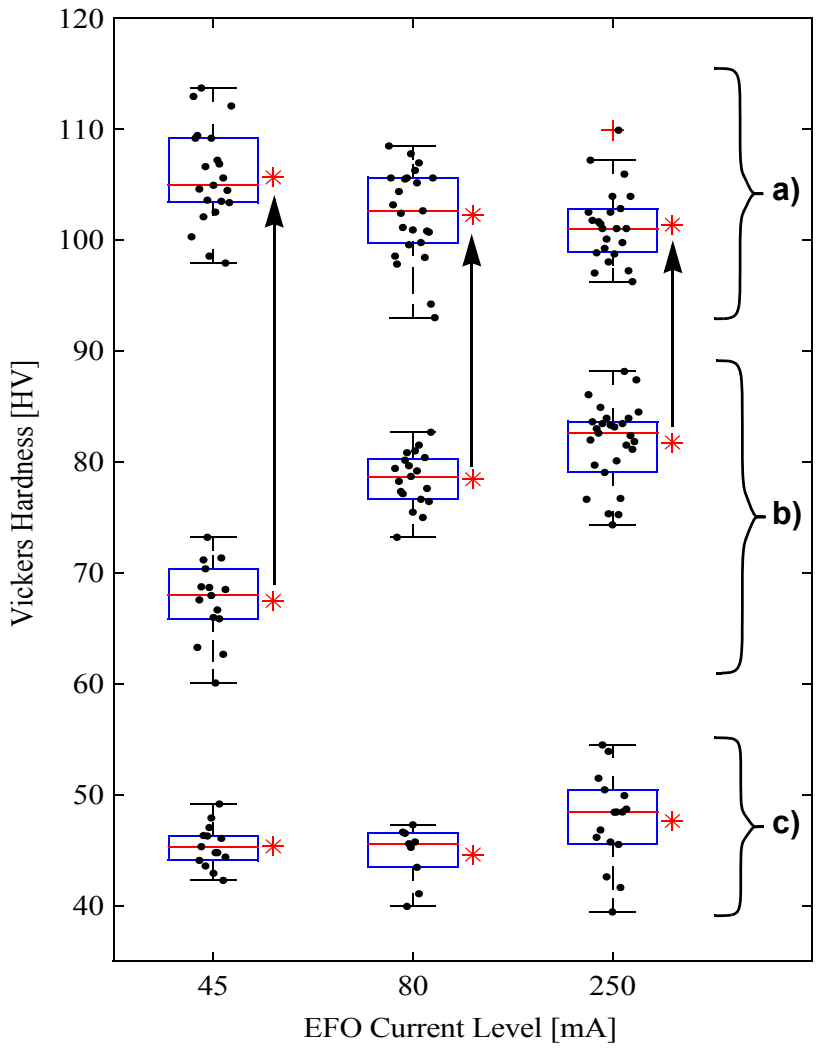

Figure 44: Vickers hardness results: a) Cu BB, b) Cu FAB, c) Au FAB. Mean values are represented by star symbols.

Table 6: Student's t-test results for Au FAB Vickers hardness (95 % confidence).

t-test Comparison	P-value
Low I vs. Medium I	0.4355
Medium I vs. High I	0.0579
Low I vs. High I	0.0688

hanging at the wire ends less than 0.5 mm away from the substrate. Therefore, the FABs remain at an elevated temperature for more than 20 min before the substrate is removed from the wirebonder hot plate. The FABs further experience elevated temperatures during the preparation steps for the

microhardness test. The recovery and recrystallization temperature range for pure Au is between 150 - 200 °C [61], but highly deformed Au has even been observed to recover and recrystallize at room temperature [61, 62]. Dopants are added to the Au wire to increase the annealing temperature and improve the thermal properties of the Au wire [61, 63]. Even though dopants have been added, some recovery and recrystallization in the Au FAB may have occurred resulting in no change in microhardness at the different I_{EFO} levels.

The relation of microhardness of the Cu FAB with the I_{EFO} level has the opposite trend of what was found for the BBs hardness in Ref. 38 and in the online deformability study [Fig. 43]. This opposite trend suggests different amounts of work hardening on the FABs when produced with different process conditions. The work hardening effect during deformation is larger for Cu FABs produced at lower I_{EFO} levels. The FABs have a lower microhardness but deform relatively less during the online deformability test. The opposite trend observed could be due to different grain sizes in the FABs produced with different I_{EFO} levels or differences in the recovery and re-crystallization. Further investigation is required to determine the actual cause of this phenomenon.

2.4 Bonded Ball Microhardness

The microhardness of cross-sectioned Cu BBs with respect to the I_{EFO} level, shown in Fig. 44 and Table 5 follow the same trend as the microhardness results in Ref. 38 and the online deformability test (Fig. 43). The BBs that are produced with a higher I_{EFO} level FAB have a lower hardness than BBs that are produced using a lower I_{EFO}. The observed difference in microhardness of the Cu BBs produced using I_{EFO} = 45 mA and I_{EFO} = 250 mA is 4.27 HV. A difference of 9.28 HV was observed between BBs produced using FABs using I_{EFO} = 30 mA and I_{EFO} = 105 mA in Ref. 38.

The difference between the change in hardness in this study compared to Ref. 38, possibly is due to US effects. In the current study an ultrasonic generator current (USG) of approximately 590 mA was used where as Ref. 38 only used an USG current of 90 mA. Even if the USG current values obtained from two different wire bonder types cannot be directly compared, the BBs in the current study were severely overbonded compared to those in Ref. 38. More US will result in larger effect on the mechanical properties of the BB due to acoustic residual softening as shown in Fig. 45 a) and b) for Au and Cu, respectively [34]. The higher level of US used in this study will diminish the effects of varying I_{EFO} during FAB formation. The amount of hardening related to strain hardening or ultrasonic effects cannot be distinguished between in this study.

In order to reduce the underpad stress that can cause underpad damage during bonding, more than the hardness of the Cu FAB should be considered. The EFO parameters that effect the hardness of the FAB also effect the magnitude of work hardening that occurs during bonding. The

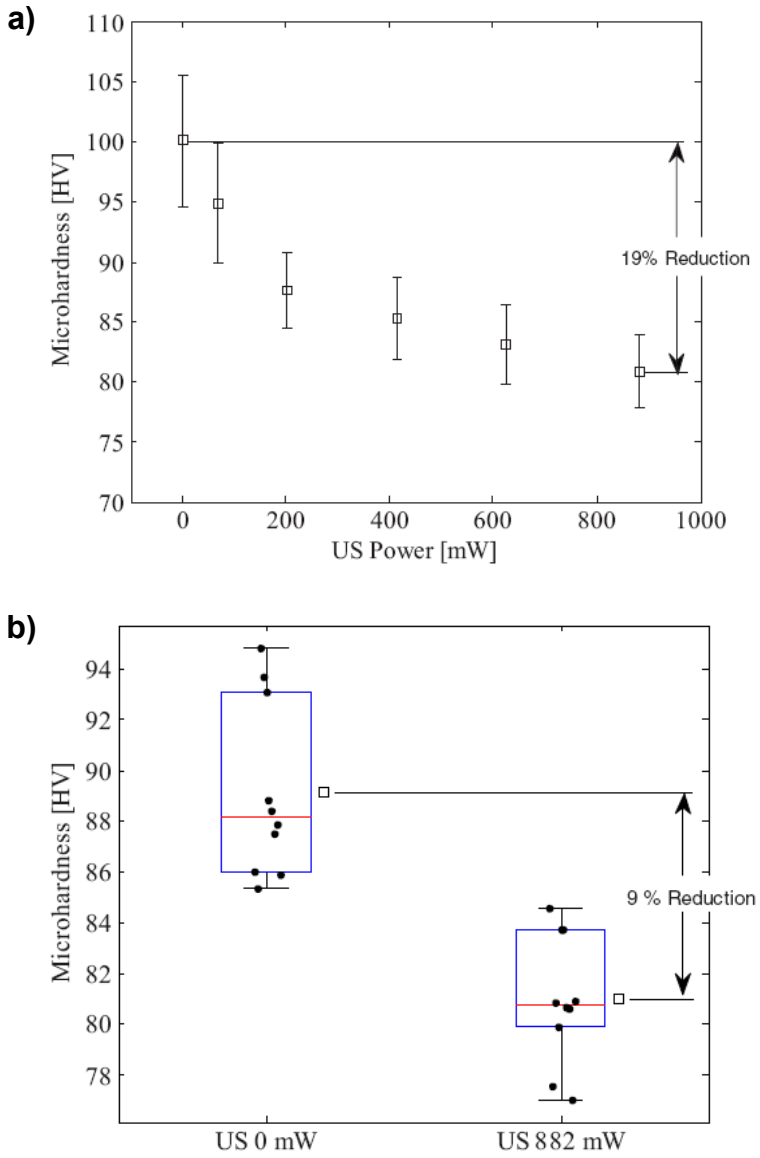

Figure 45: Microhardness of (a) Cu BBs and (b) Au BBs deformed with different US power levels. The error bars in (a) indicate one standard deviation [34].

harder FAB produced at a high I_{EFO} will produce a softer BB relative to softer FABs that are produced with lower I_{EFO}. Therefore, a harder Cu FAB will be more desirable because it will work harden less, producing a softer deformed ball and reduces diepad stresses during subsequent bonding [51].

2.5 Comparison of Online Deformability Measurements with Vickers Hardness Tests

The results obtained from both the online deformability test and the Vickers hardness test show that Cu FABs produced with higher I_{EFO} will be relatively softer either, after being deformed using the online method or, both deformed and bonded when using the Vickers hardness method. Since, both of the methods give similar trends with respect to the level of I_{EFO}, a correlation between the results can be obtained. Using the averages for each I_{EFO} level from both of the methods the correlation coefficient is calculated to be $r = 0.83$. The US effects experienced by the BBs may be responsible for weakening the correlation between the two methods.

In order to determine which method of measuring hardness is more precise the error of the differences between the mean values at each I_{EFO} level is taken. The percentage of the error of difference is a measure for the precision of the test method. The percentages of the error of difference are outlined in Table 7 for both the online and Vickers hardness methods. The online method when comparing the difference between the low vs. medium I_{EFO}, medium vs. high I_{EFO}, and low vs. high I_{EFO} is therefore approximately 2 times, 12.5 times, and 4 times, respectively, more precise than the Vickers hardness method. There is naturally more error built into the Vickers hardness

Table 7: Percent error of difference for online deformability and Vickers hardness method

Cu Wire I_{EFO} Comparison	% Error of Difference	
	Online Deformability	Vickers Hardness
Low vs. Medium	21.3	38.3
Medium vs. High	9.8	126.1
Low vs. High	7.5	28.3

method, as error can arise from specimen preparation and mounting, inadequate optical measurements or even by the effects of the specimens structure [39]. The second factor affecting the accuracy is that the US effect which, is not present during the online deformability test. The US effect does, however, become a factor when performing the Vickers hardness test on the Cu bonded balls and may be responsible for adding additional error to the microhardness results.

2.6 Summary

While no significant effect of EFO parameters on the microhardness of Au FABs was observed, it has been shown that the EFO parameters have a substantial effect on Cu FABs. Upon initial deformation as typically observed in microelectronic ball bonding, work hardening occurs for both materials and depends on EFO parameters in a similar way for both materials. The work hardening effect is stronger with FABs produced with lower I_{EFO} levels, reversing the difference in hardness that exists before deformation. These results contribute to an improved understanding of FAB formation and deformation effects which are affecting the US stress levels present during the bonding process. Such understanding can help find a way how to reduce the underpad damage in Cu ball bonding processes on sensitive substrates.

3.0 Effect of Shielding Gas Type and Flow Rate on Free Air Ball Quality

This chapter focuses on oxidation and the complications associated with adding a shielding gas to the EFO process. Excessive oxidation can lead to process reliability issues and further increases the hardness of the Cu FAB [9-11, 17]. The oxidation of Cu wire during bonding is reduced by supplying a shielding gas to the EFO site during FAB formation. The shielding gasses used are usually a mixture of H_2 and an inert gas such as Ar or N_2 (forming gas) [18]. A mixture of 5 % H_2 and 95 % N_2 is the most common forming gas mixture used today. The hydrogen in the gas mixture reduces the oxide on the wire surface during the EFO process [11].

The melting and solidification of the FAB during the EFO process has been studied extensively for Au wire. Complex models have been developed to help understand the formation of the Au FAB during EFO [19]. The formation of a Cu FAB is even more complex due to the effects of oxidation and the use of a shielding gas. Factors such as extensive oxidation and convective cooling affect the formation of the FAB and can cause FAB defects [9, 11, 20]. Forming gas reduces the oxidation of the Cu FAB but is an additional expense and a safety concern for the wire bonding industry. A novel Cu alloy or wire type that can eliminate the need for H_2 in the shielding gas or even eliminate the shielding gas all together would be a huge breakthrough for Cu wire bonding. However, developing new wires is very time consuming and there is not yet a solid understanding of how the shielding gas effects the formation of the Cu FAB.

Online methods have been developed to characterize wire deformation/hardness and the resulting in-situ underpad stresses during bonding. They are especially useful for characterizing new prototype wires and optimizing process parameters [35, 40, 41, 44, 46, 50]. A prototype wire that does not meet certain standards can be discarded early preventing wasted time performing tedious manual characterization techniques. In this study an online method is used that can characterize the shape and deformability of 380 FABs in one hour [46]. This online FAB characterization method is used in parallel with SEM images to develop a method of determining optimal shielding gas flow rates using 5 % H_2 + 95 % N_2 forming gas and a 100 % N_2 gas. The common types of FAB defects and the conditions at which they occur are identified.

3.1 Experimental Procedure

Various 25 µm diameter wires are used along with the SBNE-35BD-AZM-1/16-XL capillary manufactured by Small Precision Tools Ltd., Lyss, Switzerland. Two different Cu wires were chosen (Cu1 and Cu2) as well as a Au wire that is used as the base case where oxidation is not a factor during EFO. All of the bonding is performed on a Ag plated Cu leadframe shown in Fig. 39 using an automated Besi ESEC 3100 thermosonic wire bonder shown in Fig. 17. The EFO performance of each of the wires is investigated using the 5 % H_2 + 95 % N_2 forming gas as well as an inert N_2 gas.

The EFO parameters are optimized to give a FAB diameter of approximately 50 µm [46]. Sets of EFO parameters are found for each wire in the forming gas and N_2 gas atmospheres and are presented in Table 8. A larger I_{EFO} is required for forming the Cu FABs due to the superior thermal conductivity of Cu compared to Au.

3.1.1 Online Free Air Ball Characterization Method

For the online FAB characterization method, an encoder measures the bondhead position with sub-micron precision along the z-axis [40, 46]. The z-position of the capillary tip is derived

Table 8: EFO parameters for 50 µm diameter FAB using forming gas and N_2 gas with a shielding gas flow rate of 0.5 l/min and a tail length of 500 µm.

	EFO parameters: Forming gas			**EFO parameters: N_2 gas**		
	Cu1	**Cu2**	**Au**	**Cu1**	**Cu2**	**Au**
Electrode to Wire Distance [µm]	300	300	500	300	300	500
EFO Current [mA]	80	80	52	80	80	52
EFO Time [ms]	0.43	0.43	0.5	0.46	0.46	0.51

from the encoder measurements and recorded during bonding. Rows of ball-stitch bonds are made where the z-position is used to derive a reference height (H_{ref}) of the bonding surface, the Z_1 height of the undeformed FAB, and the Z_2 height of the deformed FAB as shown in Fig. 46. The bonding direction is alternated from east to west in order to eliminate the need for a column of reference bonds as previously done in the deformability studies [Fig. 20]. The reference height (H_{ref}) is measured from the wedge bond of the adjacent wire bond. This bond orientation allows each wire bond to be a test bond and doubles the amount of measurements that can be taken compared to the deformability method presented in section 1.4.1 and used in chapter 2.0.

The Z_1 height is taken when the FAB is touched down with 20 mN force. The 20 mN force is too low to cause significant deformation of the FAB [44]. The Z_2 height is taken after the FAB

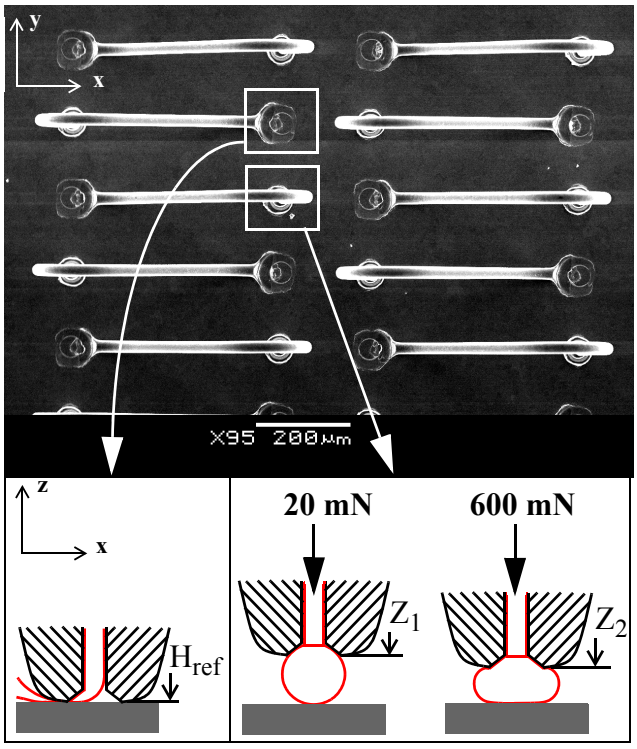

Figure 46: SEM image of rows of ball-stitch bonds for height measurements and schematic illustration of reference height, Z_1, and Z_2 measurements.

has been deformed with a force of 600 mN. This is a suitable force value for the type of wire and materials used. Once the Z_2 height has been measured, the deformed ball is bonded by applying the bonding force and ultrasound (US) in order to complete the process. The FAB height (H_{FAB}) can now be calculated using

$$H_{FAB} = Z_1 - H_{ref} \tag{8}$$

and the deformed ball height (H_{def}) can be calculated using

$$H_{def} = Z_2 - H_{ref}\,. \tag{9}$$

Fig. 47 shows an example of the online force, US level, and z-position signals recorded during each bonding cycle [46].

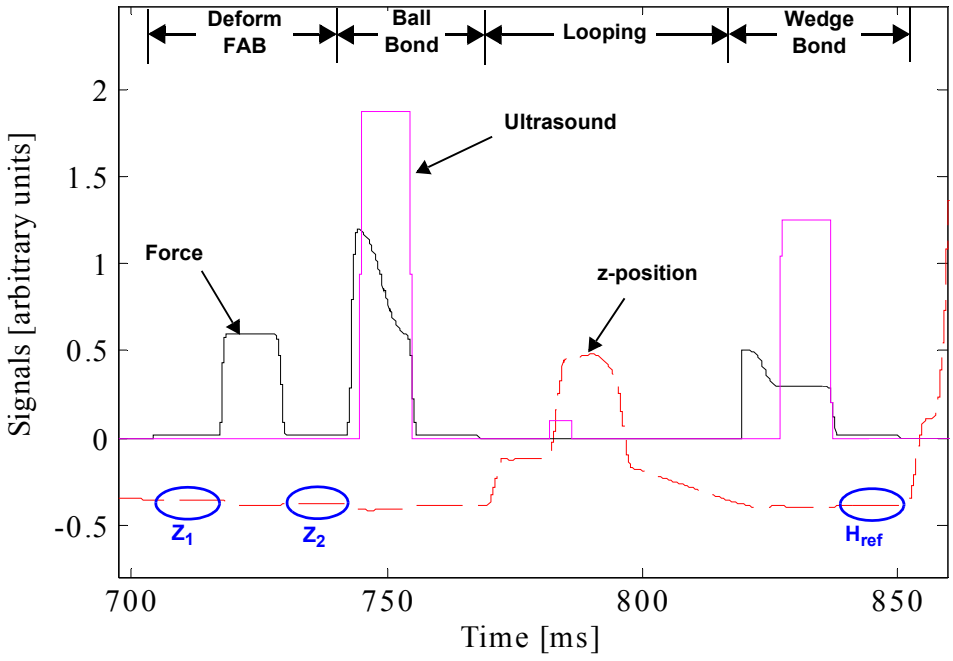

Figure 47: Representative signals for force, US level, and z-position recorded from the wire bonder. The measurement periods for Z_1, Z_2, and H_{ref} are indicated by circles. The force and z-position signals are the actual recorded signal where the US is a control signal that the real A.C. US tries to follow [46].

The H_{FAB} and H_{def} measurements are taken for each of the three wire types using both forming gas and N_2 gas. The wire bonder is not capable of reading flow rates below 0.2 l/min and flow rates above 1.0 l/min promotes severely defective FABs and NSOP failures where ball bonds can not be made. Therefore, a total of 180 ball-stitch bonds are made at each of the flow rates from 0.2 l/min to 1.0 l/min at 0.05 l/min increments.

3.1.2 Visual Characterization of Free Air Balls

SEM images are used to characterize the FABs size, shape and surface condition at various flow rates. SEM images also help identify the possible mechanism for a defective FAB. Free air ball defects such as variation in diameter or shape are identified using the online method in parallel with SEM images. Observed shapes are spherical, pointed, or golf-clubbed, as illustrated in Fig. 48 a), b), and c), respectively. In the spherical case, the ball is spherical and the wire axis projects through the ball center. In the pointed case, the ball shape has a point usually at the far end from the wire. While the ball might be almost spherical in the golf-clubbed case, its center point is substantially off the extended wire axis.

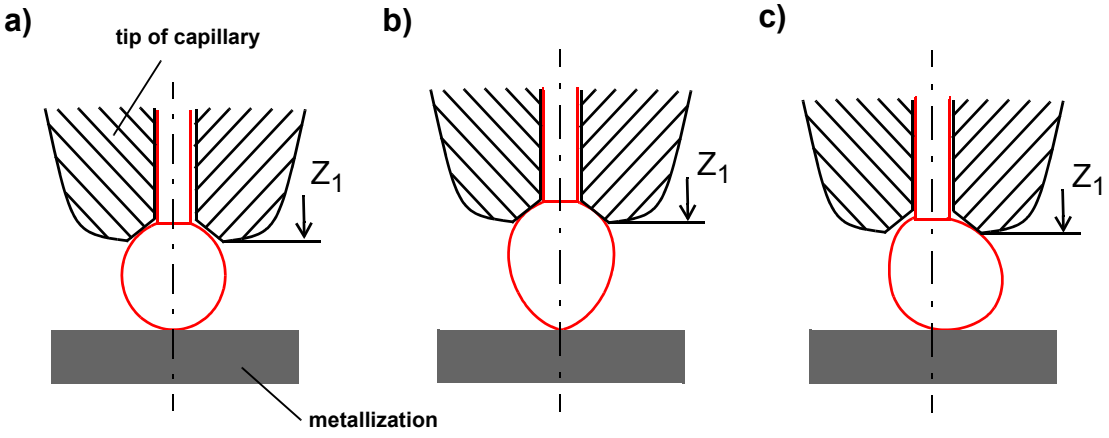

Figure 48: Common FAB shapes: a) spherical FAB, b) pointed FAB defect, and c) golf-clubbed FAB defect.

3.1.3 Measuring Forced Convective Cooling Effect of Shielding Gas

Oxidation of the surface of the molten Cu FAB or excessive forced convective cooling due to high shielding gas flow rates can produce these FAB defects [20]. The forced convective cooling effect is measured using a thermocouple as the flow rate of the shielding gas is increased as shown in Fig. 49. A k-type (chromel-alumel) thermocouple manufactured by OMEGA, Laval, Quebec, Canada, is used.

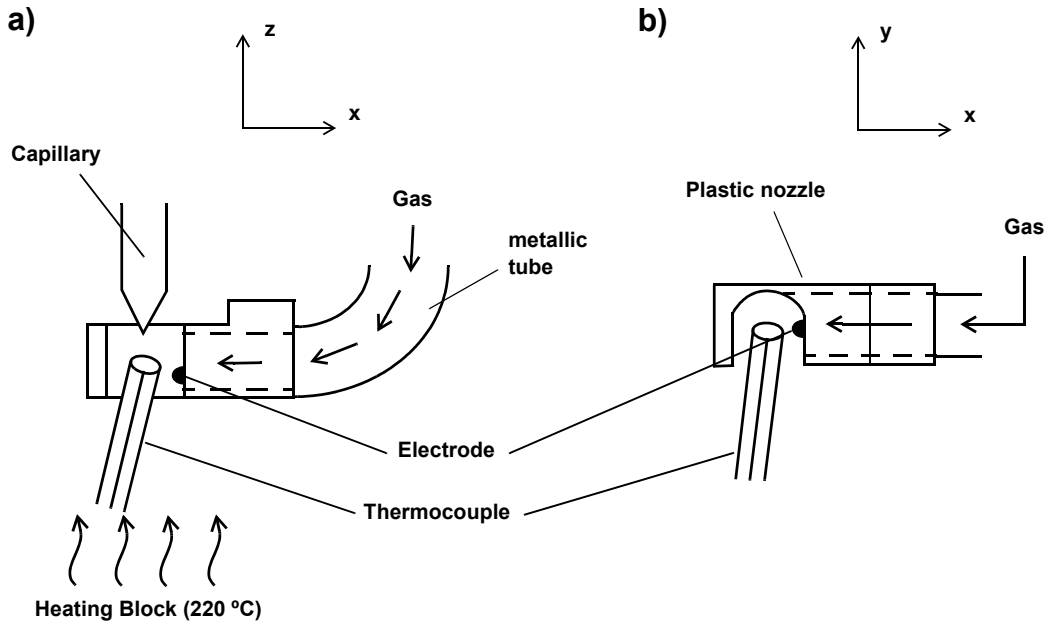

Figure 49: Setup for measuring forced convective cooling effect of shielding gas with increasing flow rate; a) front view of electrode, b) top view of electrode. Metallic tube has an inner diameter of 1 mm.

3.2 Free Air Balls Produced in Forming Gas

3.2.1 Copper Wire 1 (Cu1)

The FABs are characterized using the online FAB characterization method in parallel with SEM images. The results for the online FAB characterization are shown in Fig. 50. From the online measurements no monotonic trend in H_{FAB} is observed with increasing the flow rate. For flow rates above 0.7 l/min, the H_{FAB} does not change and the standard deviation increases drastically. The

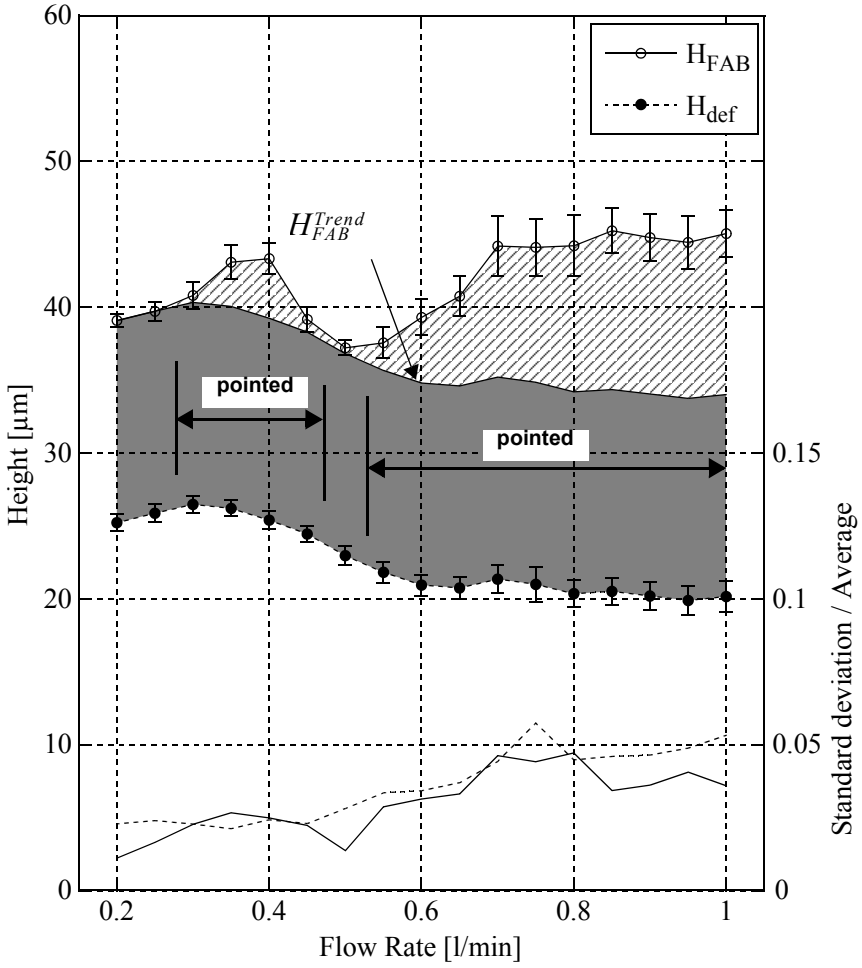

Figure 50: Cu1 wire height measurements from online FAB characterization in forming gas. The mis-shaped FAB area is identified by the hatched region. The normalized standard deviation for both the H_{FAB} and H_{def} measurements are plotted with a solid line and dashed line, respectively.

standard deviation of the H_{FAB} and H_{Deaf} measurements is normalized by dividing by the averages and plotted on Fig. 50 for each of the flow rates.

Using SEM images the actual shape and quality of the FAB is determined at each of the different flow rates. From the SEM images in Fig. 51 a) and c) it can be seen that the FAB is of good quality at flow rates of 0.2 l/min and 0.5 l/min. The standard deviation of the H_{FAB} measurements are the lowest at 0.2 l/min and 0.5 l/min with values of 0.44 µm and 0.51 µm respectively. Insignificant surface oxidation is observed and the grain boundaries are clearly visible. The FABs are pointed at flow rates of 0.4 l/min and 0.75 l/min as shown in Fig. 51 b) and d), respectively. The standard deviation of the H_{FAB} measurements at flow rates of 0.4 l/min and 0.75 l/min increases to 1.08 µm and 1.95 µm, respectively. Oxidation is identified visually on the pointed FABs shown in Fig. 51 b) and d), where a scale like oxide is observed on the FAB surface.

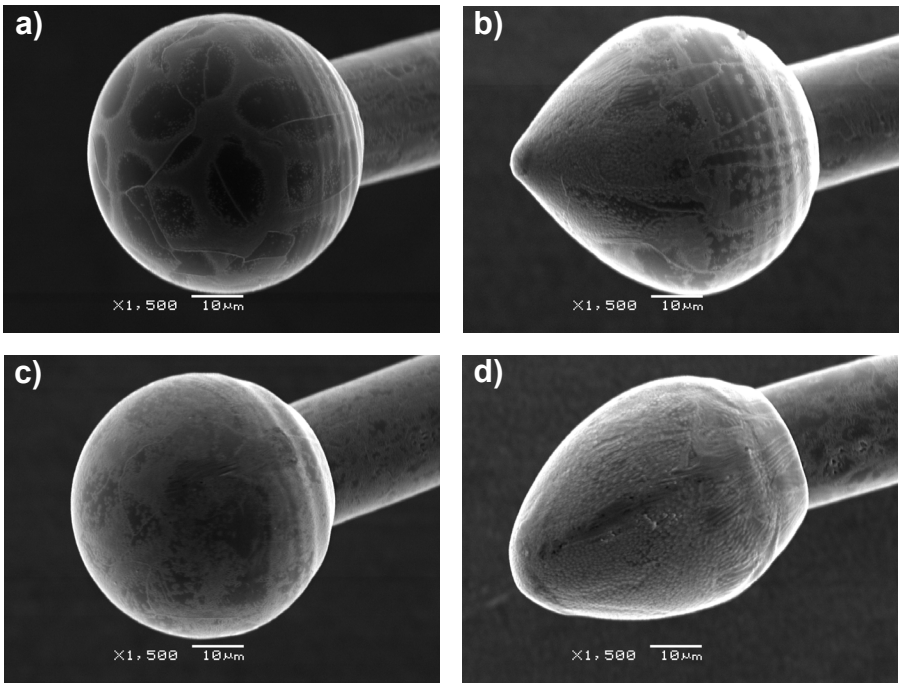

Figure 51: SEM images of Cu1 FABs produced in forming gas at flow rates of a) 0.2 l/min, b) 0.4 l/min, c) 0.5 l/min, and d) 0.75 l/min.

From the SEM images the changes in H_{FAB} measured using the online method are due to changes in the FAB shape, where as the H_{def} measurements are more dependent on the volume of the FAB. Spherical Au FABs with different H_{FAB} measurements are deformed and plotted against the H_{def} measurements as shown in Fig. 52. A linear correlation is found between the H_{FAB} and H_{def} measurements and with a deformation force of 600 mN the slope approaches unity. Therefore, in a process where a spherical FAB is produced at all flow rates, the H_{FAB} measurements only vary due to changes of FAB diameter and follow the same trend as the H_{def} measurements. Such H_{FAB} measurements are named H_{FAB}^{Trend} and are calculated by

$$H_{FAB}^{Trend} = H_{def} + \Delta H_{min} \tag{10}$$

where, ΔH_{min} is the minimum difference between H_{FAB} and H_{def} from all flow rates [46]. When H_{FAB} is approximately equal to H_{FAB}^{Trend} as illustrated in Fig. 50 for the Cu1 wire at flow rates of 0.2 l/min, 0.25 l/min and 0.5 l/min, the FAB is spherical and of good surface quality. All other flow

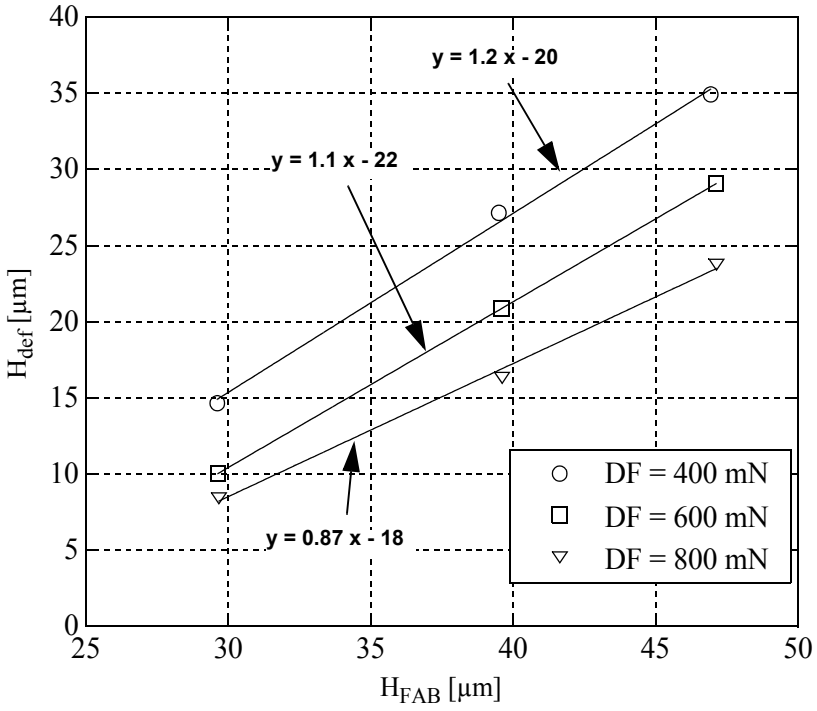

Figure 52: Correlation between H_{FAB} and H_{def} measurements for various sized Au FABs deformed with deformation forces of 400, 600, and 800 mN.

rates where pointed FABs are produced are identified by the hatched area above H_{FAB}^{Trend} termed the mis-shaped FAB area [46].

3.2.2 Copper Wire 2 (Cu2)

The results for the online FAB characterization of Cu2 are shown in Fig. 53. For the Cu2 wire there is an obvious trend in the H_{FAB} with increasing flow rate. This trend with increasing flow rate is similar to the results found in Ref. 20. The FAB height increases from 0.2 l/min to 0.3 l/

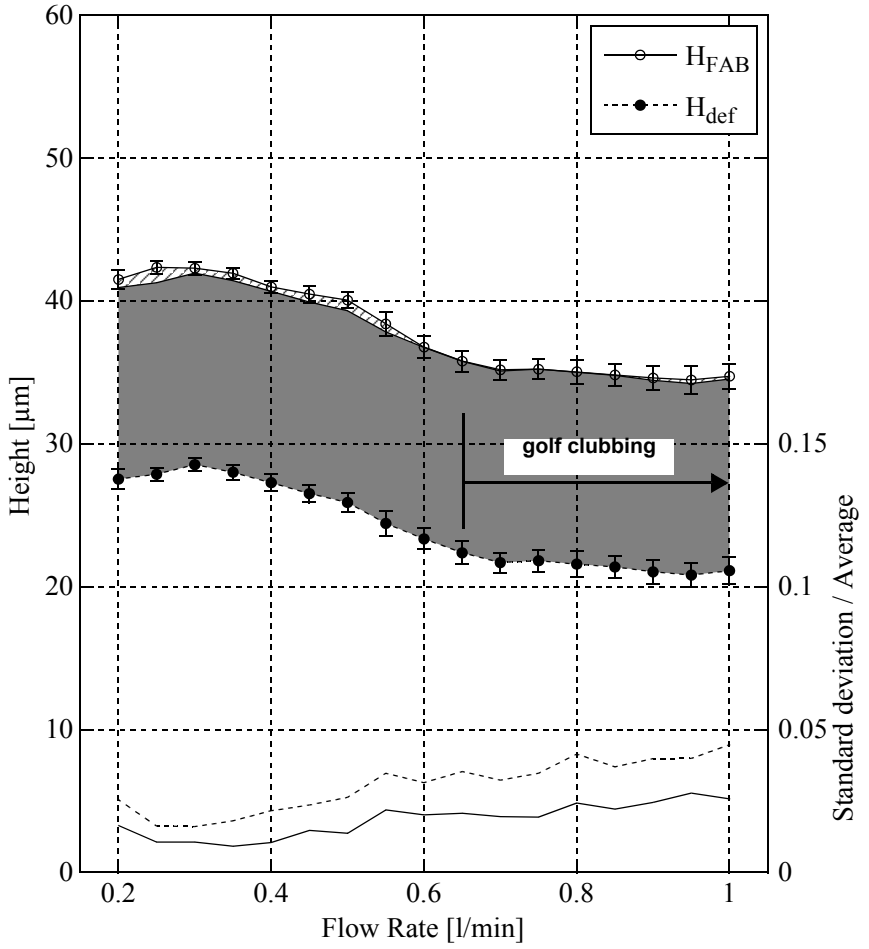

Figure 53: Cu2 wire height measurements from online FAB characterization in forming gas. The mis-shaped FAB area is identified by the hatched region. The normalized standard deviation for both the H_{FAB} and H_{def} measurements are plotted with a solid line and dashed line, respectively.

min before decreasing until a flow rate of 0.7 l/min. However, at flow rates above 0.7 l/min the slope in the H_{FAB} trend changes and H_{FAB} remains approximately constant.

Images of the FABs produced at various flow rates are shown in Fig. 54. The FABs produced with flow rates below 0.65 l/min are of good quality which correlates well with the low standard deviation values calculated from the online measurements. However, as seen in Fig. 54 c) and d), golf clubbed defects start to occur at flow rates above 0.65 l/min. Also, at higher flow rates more severe oxidation is observed on the FAB as observed in Fig. 54 d).

The measured H_{FAB} values follow the calculated H_{FAB}^{Trend} values closely for all flow rates and the mis-shaped FAB area is small, as shown in Fig. 53. As expected this indicates that spherical FABs are produced. However, golf clubbed defects occur at flow rates above 0.65 l/min even

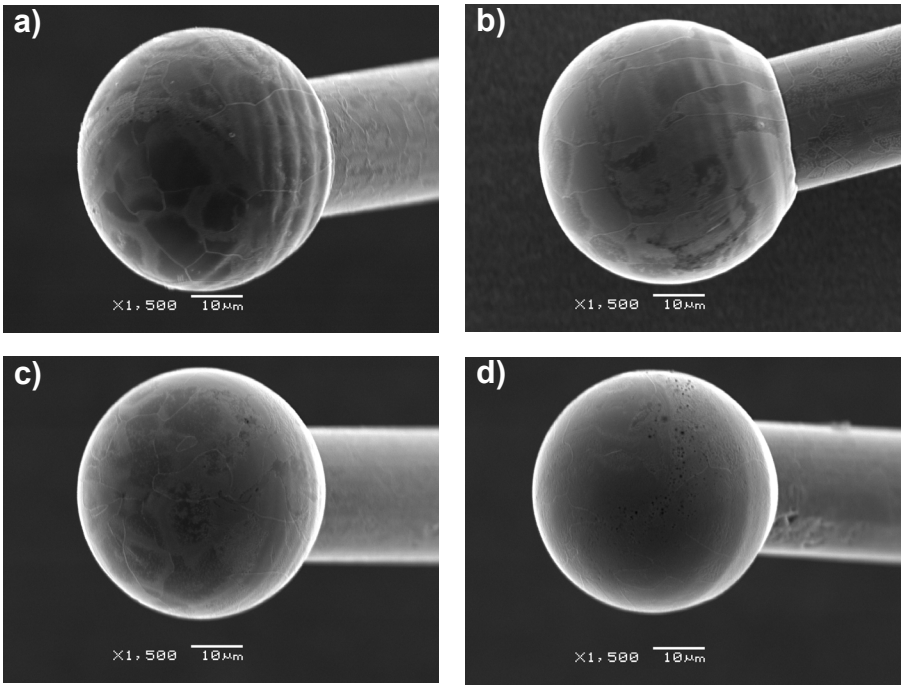

Figure 54: SEM images of Cu2 FABs produced in forming gas at flow rates of a) 0.2 l/min, b) 0.5 l/min, c) 0.65 l/min, and d) 0.8 l/min. Golf-clubbed shapes in c) and d) pointing towards observer.

though the H_{FAB} measurements follow the H_{FAB}^{Trend} values closely. However, the slope in the H_{FAB} and H_{def} curves decreases at 0.65 l/min, indicating a change in the EFO process and the occurrence of FAB defects.

3.2.3 Gold Wire

Since Au does not oxidize the effects of the forming gas and the flow rate can be more easily identified. The online FAB characterization results are shown in Fig. 55. Since it is possible to bond Au FABs with no forming gas because oxidation is not an issue, the online characterization

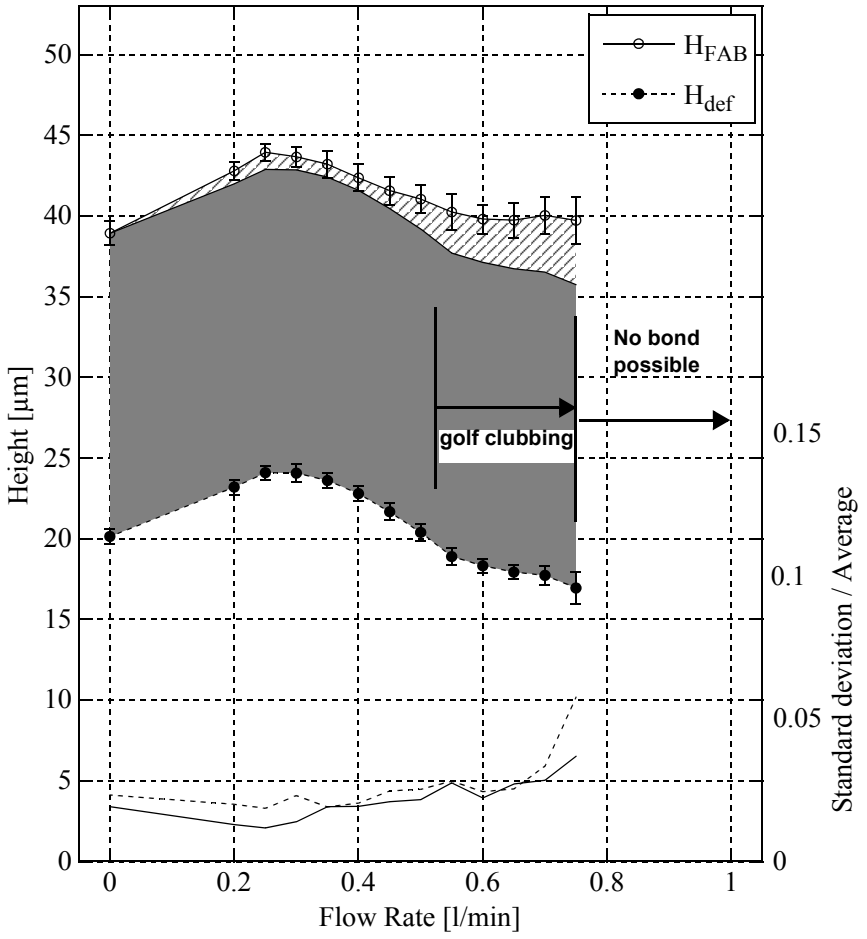

Figure 55: Au wire height measurements from online FAB characterization in forming gas. The mis-shaped FAB area is identified by the hatched region. The normalized standard deviation for both the H_{FAB} and H_{def} measurements are plotted with a solid line and dashed line, respectively.

method is performed at a flow rate of 0 l/min. The H_{FAB} and H_{def} increase from flow rates of 0 l/min to 0.25 l/min and then decrease steadily until about 0.65 l/min. This trend is again similar to the results found for the Cu2 wire and in Ref. 20.

The H_{FAB} and H_{FAB}^{Trend} values are similar for flow rates up to 0.5 l/min as shown in Fig. 55. Spherical FABs are produced at flow rates up to 0.5 l/min as shown in Fig. 56 a) and b). Above 0.5 l/min the FAB becomes golf clubbed and at 0.8 l/min spherical FABs can no longer be formed as shown in Fig. 56 c) and d), respectively. At flow rates above 0.5 l/min the mis-shaped FAB area increases, and also, the slope in H_{FAB} and H_{def} changes at flow rates above 0.55 l/min where H_{FAB} remains constant.

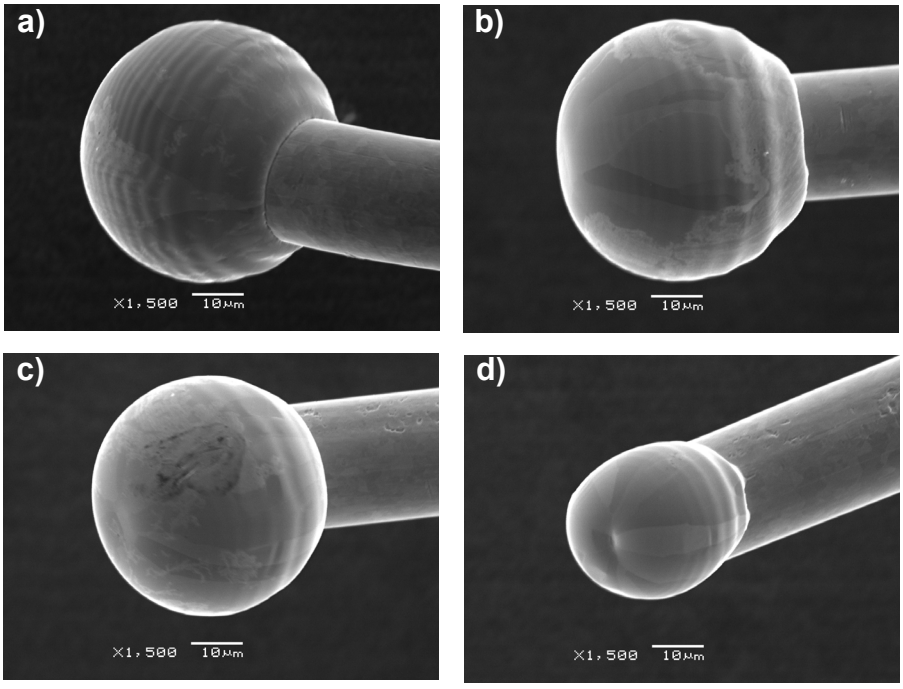

Figure 56: SEM images of Au FABs produced in forming gas at flow rates of a) 0.25 l/min, b) 0.4 l/min, c) 0.6 l/min, and d) 0.8 l/min.

3.3 Free Air Balls Produced in Nitrogen Gas

3.3.1 Copper Wire 1 (Cu1)

The quality of the FABs is expected to decrease when they are formed in N_2 gas. This is due to the fact that there is no H_2 present to reduce the Cu oxide during EFO. The online FAB characterization results in N_2 gas are shown in Fig. 57. The standard deviation of the H_{FAB} is approximately double that of the FABs produced in forming gas. An abrupt jump in H_{FAB} occurs at a 0.65 l/min flow rate and again, the H_{FAB} remains constant above a flow rate of 0.65 l/min.

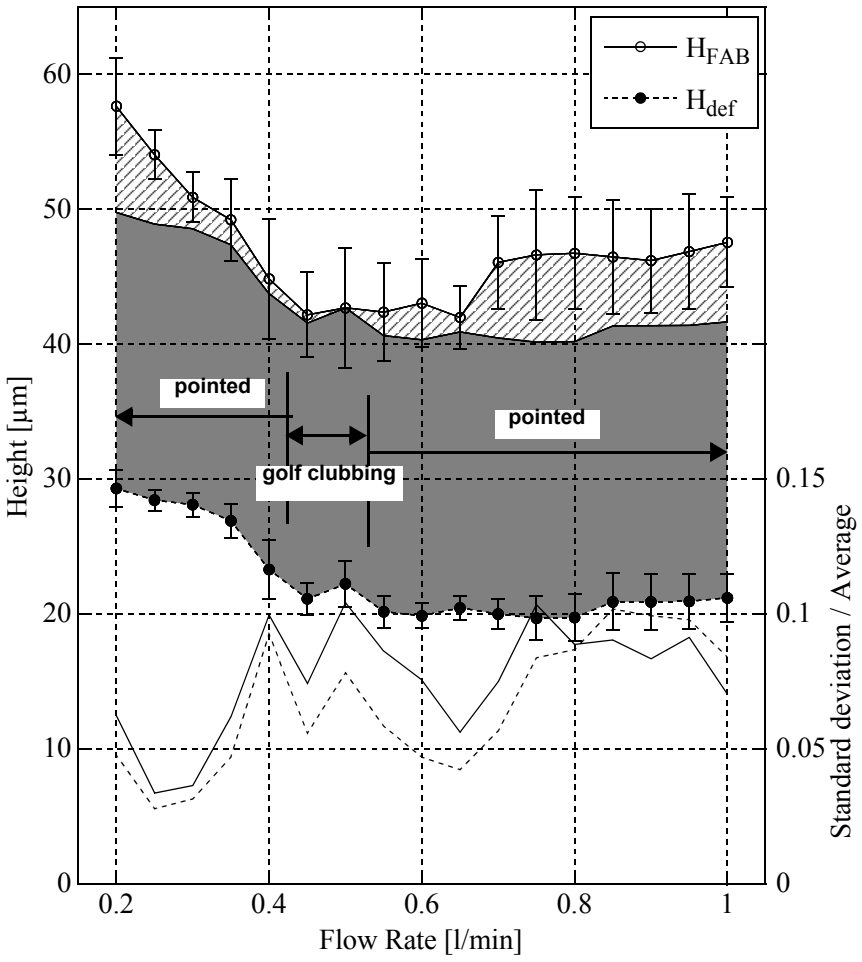

Figure 57: Cu1 wire height measurements from online FAB characterization in N_2 gas. The mis-shaped FAB area is identified by the hatched region. The normalized standard deviation divided for both the H_{FAB} and H_{def} measurements are plotted with a solid line and dashed line, respectively.

SEM images of the Cu1 FABs produced in N_2 gas are shown in Fig. 58. Every FAB is defective and severe oxidation is observed on its surface. The FAB shapes changes from severely pointed at 0.2 l/min flow rate to slightly ovalized at 0.55 l/min and then again becomes pointed at a flow rate of 0.7 l/min.

The H_{FAB} and H_{def} trends have several changes in slope, and the mis-shaped FAB area is large. Therefore, it is expected that the FABs will be defective at all flow rates. With flow rates from 0.45 l/min to 0.55 l/min the FABs are golf-clubbed and the H_{FAB} and H_{FAB}^{Trend} values are similar but the slopes of the H_{FAB} and H_{def} trends change abruptly in this region identifying an unstable EFO process.

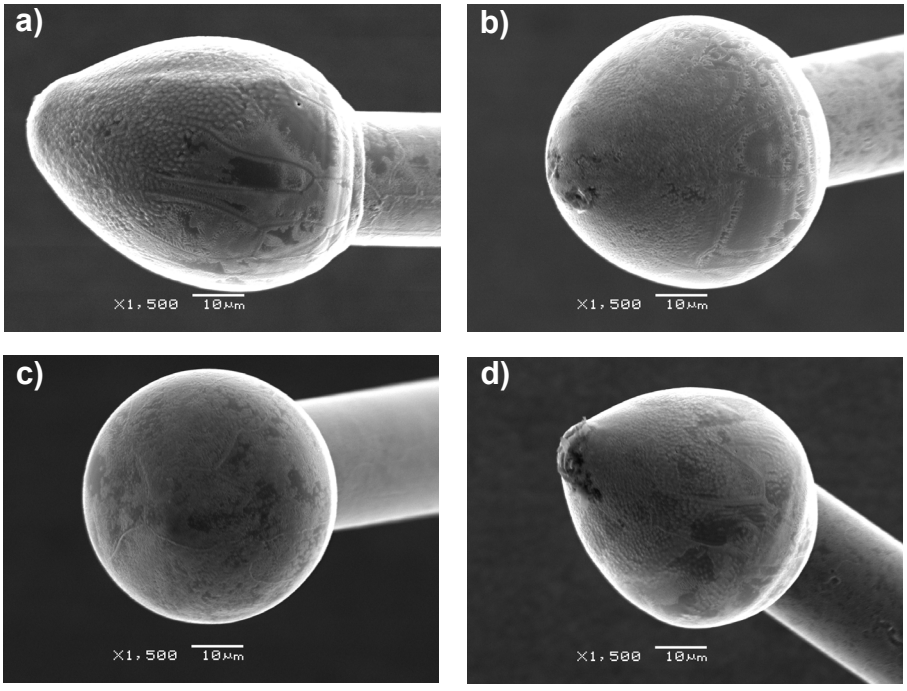

Figure 58: SEM images of Cu1 FABs produced in N_2 gas at flow rates of a) 0.2 l/min, b) 0.35 l/min, c) 0.55 l/min, and d) 0.7 l/min.

3.3.2 Copper Wire 2 (Cu2)

The online FAB characterization results for the Cu2 FABs produced in N_2 gas are shown in Fig. 59. The online test could not be performed for flow rates below 0.4 l/min due to NSOP failures where ball bonds could not be made. The standard deviation of the H_{FAB} and H_{def} measurements is more than double that of the FABs produced with forming gas just as was observed with the Cu1 wire. The H_{FAB} and H_{def} measurements decrease up to 0.65 l/min where there is an abrupt increase in both.

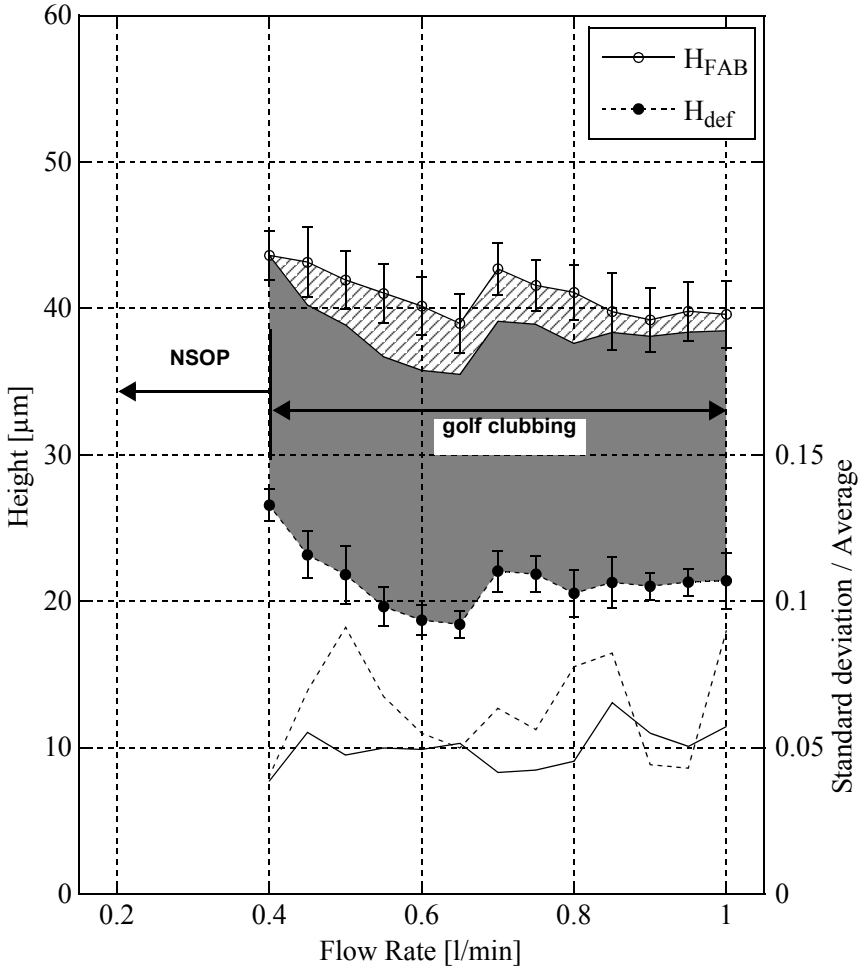

Figure 59: Cu2 wire height measurements from online FAB characterization in N_2 gas. The mis-shaped FAB area is identified by the hatched region. The normalized standard deviation for both the H_{FAB} and H_{def} measurements are plotted with a solid line and dashed line, respectively.

The SEM images shown in Fig. 60 again reveal oxidation of the FABs produced in N_2 gas. The Cu2 wire tends to form golf-clubbed defects varying in severity at all N_2 gas flow rates. Severe golf-clubbing and significant surface oxidation occurs at flow rates below 0.4 l/min where NSOP failures occur and also above 0.65 l/min where the online H_{FAB} and H_{def} measurements increase abruptly.

From the online results shown in Fig. 59 the mis-shaped FAB area is observed to be large. Only golf-clubbed FABs were observed with the Cu2 wire when formed in N_2 gas. The H_{FAB} and H_{FAB}^{Trend} values are equal at 0.4 l/min but spherical FABs were not produced. If the ΔH_{min} used to calculate the H_{FAB}^{Trend} value is from a unstable EFO process where FAB defects occur, H_{FAB}^{Trend} can not be used to identify flow rates where spherical FABs are produced. Since FAB defects were produced at all flow rates in this case, no conclusion can be made from H_{FAB} being equal to H_{FAB}^{Trend}.

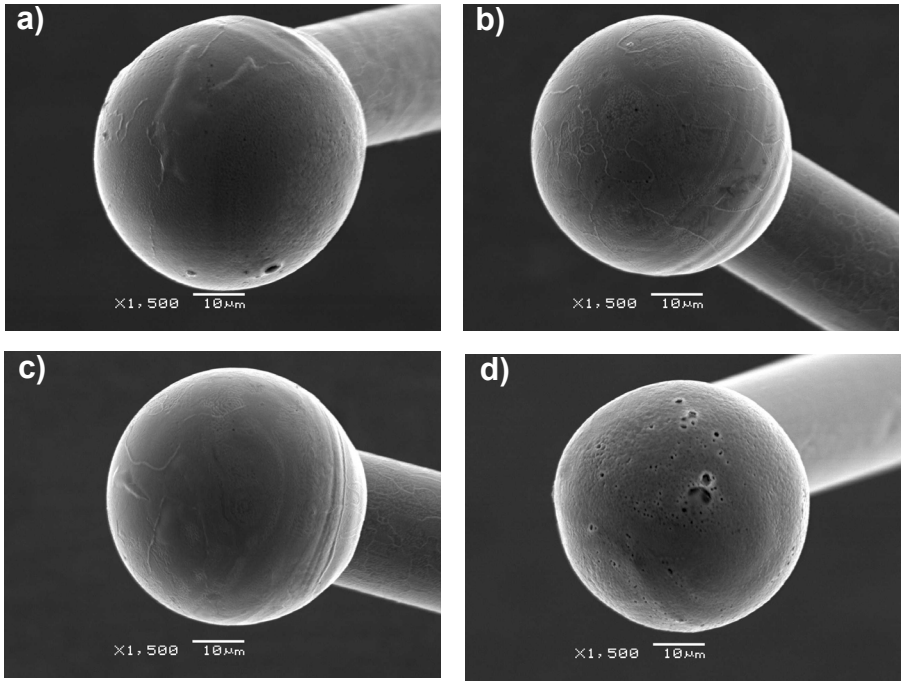

Figure 60: SEM images of Cu2 FABs produced in N_2 gas at flow rates of a) 0.2 l/min, b) 0.5 l/min, c) 0.6 l/min, and d) 0.75 l/min. Golf-clubbed shapes pointing towards observer.

3.3.3 Gold Wire

The two main purposes of studying Au FAB formation in N_2 gas is to understand how the gas flow effects the FAB formation and also to understand the effects of not having H_2 in the gas mixture. The online FAB characterization results for the Au wire are shown in Fig. 61. The H_{FAB} and H_{def} both decrease with N_2 gas. The H_{FAB} decreases up to a flow rate of 0.25 l/min before it increases slightly. The standard deviation increases drastically at 0.4 l/min and bonding could not be done at flow rates above 0.5 l/min due to a large decrease in FAB size.

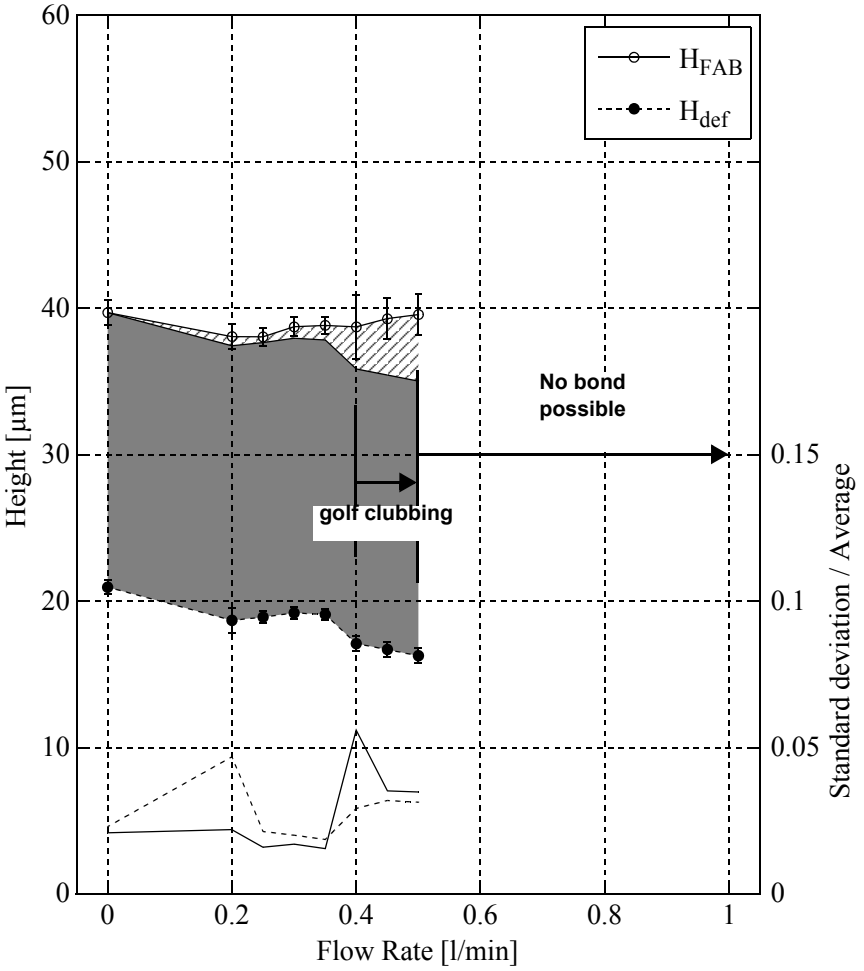

Figure 61: Au wire height measurements from online FAB characterization in N_2 gas. The mis-shaped FAB area is identified by the hatched region. The normalized standard deviation for both the H_{FAB} and H_{def} measurements are plotted with a solid line and dashed line, respectively.

The SEM images of the Au FABs are shown in Fig. 62. Spherical FABs are produced up to 0.35 l/min as shown in Fig. 62 a) and b). At flow rates above 0.4 l/min the FABs begin to become golf-clubbed as shown in Fig. 62 c). Above a flow rate of 0.4 l/min spherical FABs can no longer be formed as shown in Fig. 62 d).

The H_{FAB} and H_{FAB}^{Trend} values are similar for flow rates up to 0.35 l/min as shown in Fig. 61. Above 0.35 l/min where golf-clubbed FABs are observed the mis-shaped FAB area increases and the slopes of both the H_{FAB} and H_{def} trends change abruptly.

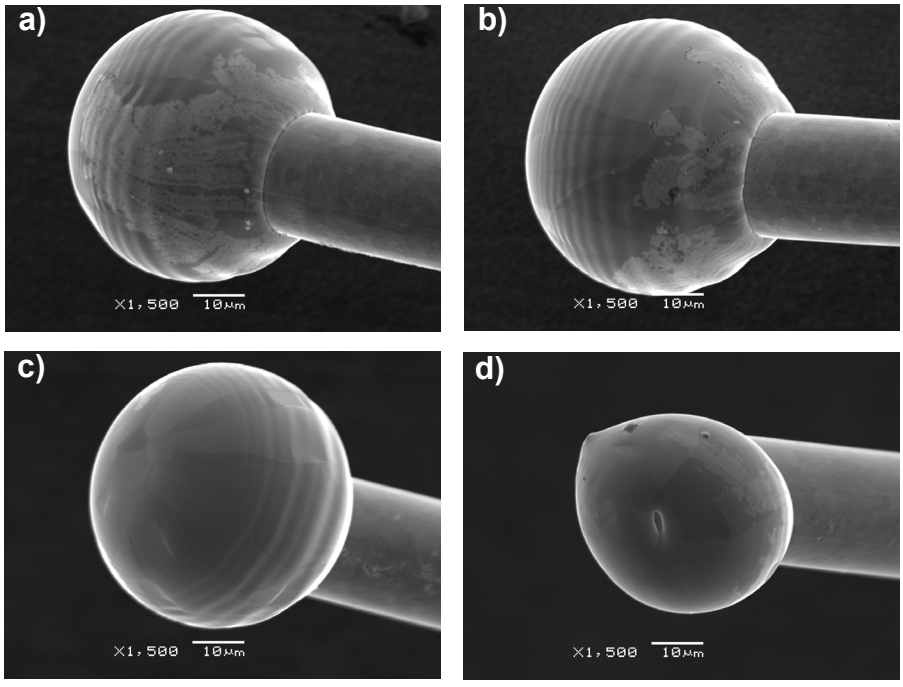

Figure 62: SEM images of Au FABs produced in N_2 gas at flow rates of a) 0.2 l/min, b) 0.35 l/min, c) 0.45 l/min, and d) 0.6 l/min.

3.4 Cooling Effect of Shielding Gas

The thermocouple measurements taken from the EFO site at various flow rates for both forming gas and N_2 gas are shown in Fig 63. With the heating block kept at 220 ºC during bonding and room temperature is approximately 21 ºC the EFO site is at a temperature of 59 ºC when the gas flow rate is 0 l/min. As the flow rate is increased to 0.65 l/min the temperature at the EFO site decreases to temperatures of 40 ºC and 42.5 ºC in forming gas and N_2 gas, respectively. For flow rates above 0.65 l/min the temperatures increases abruptly to 45 ºC in forming gas and 48 ºC in N_2 gas. It is suspected that these increases are due to the gas flow changing from laminar to turbulent.

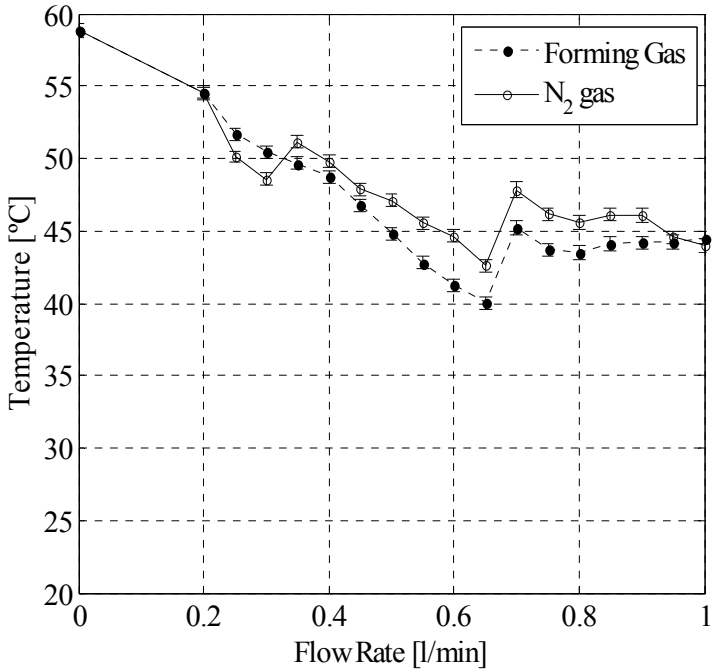

Figure 63: Temperature at EFO site with increasing flow rates of N_2 and forming gas.

3.5 Mechanisms for Free Air Ball Defects

Heavy copper oxide identified by a scale-like texture on the FAB surface in Fig. 51 and Fig. 58 can cause the surface tension of the molten Cu ball to change. The pointed FAB shape as observed with the Cu1 wire is a result of a change in surface tension of the molten ball during the formation of the FAB. Metal oxides generally have a higher melting point and lower surface tension [20]. Therefore, during solidification the oxide on the molten Cu will form first, affecting the geometry of the FAB as the molten Cu rolls up due to surface tension [20].

Another possible mechanism for the formation of pointed FABs is forced convective cooling caused by the shielding gas flow [9, 20]. The surface solidifies prematurely which again effects how the molten metal rolls up during solidification. The forced convective cooling effect of the shielding gas flow can decrease the bulk temperature of a thermocouple at the EFO site by up to 19 ºC as shown in Fig. 63. The surface temperature decrease is expected to be substantially larger. An increase in temperature gradient between the molten metal and the environment increases the likelihood of premature solidification on the surface of the molten metal. Therefore, this convective cooling effect may have played a role in the pointed FABs seen at high flow rates of both forming gas and N_2 gas for the Cu1 wire.

Several different mechanisms have been proposed for the formation of golf-clubbed FABs. Hang [9] proposed that factors such as energy input during EFO, gap length between the electrode and the wire tail, high gas flow rates, as well as the condition of the wire tail can cause golf-clubbed FABs. Energy input during EFO and shielding gas flow rates were also suggested to be a cause of golf-clubbed FABs in Ref. 11.

In this study only the effects of flow rate and gas type are directly linked to golf-clubbing since the EFO parameters have been kept constant. It is found that golf-clubbed FABs appear for both Cu2 and the Au wires at high flow rates of both forming gas and N_2 gas as shown in Fig. 54, 56, 60, and 62. At high flow rates both the drag force on the wire tail and molten metal ball could result in golf-clubbing. If the wire tail is pushed away from the electrode by the gas flow the gap will increase, which as observed in Ref. 9 leads to golf-club defects. Also, the drag force on the molten metal itself can cause the solidifying metal ball to freeze off-center on the wire. In contrast, with Cu1, pointed shapes instead of golf-clubbed shapes are observed under these conditions. The pointed FABs can also freeze off-center from the wire axis as shown in Fig. 58.

Since the I_{EFO} and t_{EFO} are kept constant in this study, the atmosphere that the FAB is formed in is the other significant variable that effects the energy input during EFO. As the flow rate is increased the convective cooling effect increases causing the removal of energy from the EFO site and again a lower energy input leads to under-formed FABs that are golf-clubbed [9]. Also, with different flow rates the composition of the atmosphere at the EFO site will change which can have an effect on the energy transferred to the wire tail via the plasma during EFO.

At flow rates above 0.65 l/min for each of the Cu wire types studied, EFO is observed to be unstable. The EFO site temperature abruptly rises as the gas flow rises above 0.65 l/min and the amount of oxidation increases. Both of these observations can be explained by a change in flow type above the 0.65 l/min threshold. If the flow does in fact become more turbulent at this flow rate, the mixing effect between the air and the shielding gas as well as the convective cooling effect will increase. With this increased mixing of the shielding gas with the air, the shielding provided

by the gasses will lose its effect and oxidation will again occur. In Fig. 51, 54, 58, and 60 the increased oxidation can be easily identified at these high flow rates leading to instability in the EFO process and FAB defects.

3.6 Free Air Ball Formation in Forming Gas Compared to in Nitrogen Gas

The 5 % H_2 in the forming gas helps reduce the Cu oxide during the EFO process and improves the Cu FAB quality [9, 11, 18, 20]. The higher quality of Cu FABs is evident for both the Cu1 and Cu2 wires. For the Cu1 wire less oxide is evident on the FAB surface when comparing the FABs formed in forming gas and N_2 gas as shown in Fig. 51 and 58, respectively. Also, the Cu2 wire had less surface oxide when the FABs are produced in forming gas rather than N_2 gas as shown in Fig. 54 and 60, respectively. Spherical FABs with insignificant surface oxide were only produced in forming gas for both Cu wires.

In addition to the reduction of Cu oxide, the H_2 added to the forming gas also provides additional thermal energy to the EFO process [11, 20]. This added thermal energy is visualized in Fig. 50, 53, and 55 from flow rates of 0 l/min to approximately 0.3 l/min where the H_{FAB} measurements increase with increasing flow rate. The size of the FAB increases with the amount of H_2 present during EFO [20]. Above a flow rate of 0.3 l/min the convective cooling effect is hypothesized to take over and the FAB size again decreases. The increase in H_{FAB} is not observed when the FABs are formed in N_2 gas as shown in Fig. 57, 59, and 61. These results are similar to those found in Ref. 20 and further indicate that the additional heat input is due to the addition of 5 % H_2 to the forming gas.

The thermal energy provided by the forming gas containing H_2 gas could be a result of the reduction of the Cu oxide or by the rapid reaction/combustion of H_2 with stray oxygen [20]. The reduction reactions between hydrogen and Cu oxides are exothermic and therefore provides thermal energy. As found in Ref. 20, an increase in H_{FAB} was also observed for Au wire as shown in

Fig. 55, where no reduction reactions occur. Therefore, the reduction of oxides is not likely the only source of additional thermal energy supplied by the H_2 gas. Since no oxidation or reduction reactions occur during the formation of the Au FAB, less thermal energy is available during EFO. As shown in Fig. 56 and 62, the Au FAB can no longer be formed at flow rates above 0.8 l/min and 0.5 l/min for FABs produced in forming gas and N_2 gas, respectively. The additional thermal energy due to the rapid reaction/combustion of H_2 with stray oxygen is a possible explanation for the ability to form Au FABs up to flow rates of 0.8 l/min in forming gas while FABs can only be formed with flow rates up to 0.5 l/min in N_2 gas. Another possible explanation is a change in the properties of the gas due to the change in gas chemistry as discussed in the following section.

3.7 Characterizing Free Air Balls with the Online Method

The purpose of the online characterization method is to eliminate the need for manual analysis methods such as SEM analysis. Online characterization can be less time consuming than taking SEM images of every FAB produced during process optimization of the EFO process. The trends in H_{FAB} and H_{def} are obtained using the online method and are used to characterize the FABs. Sudden changes in the slope of the H_{FAB} and H_{def} trends, large differences in H_{FAB} and the H_{FAB}^{Trend} values, and a large standard deviation of the H_{FAB} measurements are all indications of unstable EFO processes where FAB defects occur. The size of the mis-shaped FAB area can be used as a measure of the robustness of a wire material during EFO.

For FABs produced in forming gas, abrupt changes of the H_{FAB} measurements with increasing flow rate and large differences in H_{FAB} and H_{FAB}^{Trend} illustrated by large mis-shaped FAB areas, indicate pointed FABs. Golf-clubbed defects can be identified by the change in slope to approximately zero as seen for both the Cu2 and Au wire results shown in Fig. 53 and 55. The mis-shaped FAB area can not always be used to identify FAB defects as shown for the Cu2 wire where golf-clubbed defects occur above flow rates of 0.65 l/min and the H_{FAB} measurements and the H_{FAB}^{Trend} values remain similar.

The Cu FABs produced in N_2 gas are found to be defective and in most cases have excessive oxidation on their surface. For both the Cu1 and Cu2 wires the FAB defects are identified by abrupt changes in H_{FAB}, large mis-shaped FAB area, and the large standard deviation of the measured H_{FAB} values at each flow rates. If the FABs are defective at all flow rates, the H_{FAB}^{Trend} value can not be used to identify the flow rates where spherical FABs result.

The online characterization results for Au FABs formed in both forming gas and N_2 gas are similar. Golf-clubbed defects are identified by the slope of the H_{FAB} measurements decreasing to approximately zero and a large increase in mis-shape FAB area at higher flow rates. The effects of H_2 on the Au FAB size is identified when comparing the online characterization results of Au FABs formed in forming gas to those formed in N_2 gas.

It is important to note that the calculated H_{FAB}^{Trend} value and therefore, mis-shaped FAB area, are approximations and should only be used as indications that defective FABs are being produced. For fully conclusive results, optical or SEM imaging is recommended. Change in the FAB volume, hardness, or deformability with changing flow rate can affect the measured H_{def} value. The difference between H_{FAB} and H_{def} is not necessarily a constant.

3.8 Summary

The effectiveness of the online FAB characterization is demonstrated and the FAB formation during the EFO process has been studied using both forming gas and N_2 gas. The online method identifies the gas flow rates required to produce acceptable Cu FABs and is therefore a useful tool for optimizing the shielding gas flow rate. The flow rate should be optimized for each new wire type used.

The addition of H_2 to the gas mixture provides additional thermal energy to the EFO process and reduces the Cu oxide during EFO decreasing the likelihood of forming defective Cu FABs. The additional thermal energy is determined to not be only a result of the reduction of oxides but of at least one other source.

4.0 Electrical Flame Off Discharge Characteristics

The energy required to melt the end of the wire and form the FAB is supplied by the electrical discharge during the EFO process. The amount of energy supplied has an effect on the FAB size and shape [9, 11]. Therefore, it is of interest to investigate the effects EFO parameters, wire material, and the shielding gas composition on the EFO discharge. For example it is well known in the arc welding industry that changes in arc characteristics caused by different shielding gas atmospheres effect the amount of energy transferred by a plasma discharge [7, 13, 16, 64-71]. In this chapter a preliminary investigation into the effects of shielding gas type, wire material, I_{EFO}, and discharge gap on the EFO discharge voltage and energy transfer to the wire anode will be conducted. The discussion provided in this section provides insight into the factors that effect the energy transferred by the EFO discharge. However, further research is necessary.

4.1 Experimental Procedure

In this study the EFO discharge voltage between the electrode and different types of wires is measured during EFO using 5 % H_2 + 95 % N_2 forming gas and N_2 gas. A 1000:1 high voltage probe, shown in Fig. 64, is used to measure the voltage as in Ref. 14. The voltage probe is connected between the electrode and the wire spool as shown in Figs. 65, a) and b). The spool is used as the ground to prevent damage to sensitive components on the bond head. The wire spool and the wire clamp share a common ground and the resistance between them is 4.3 Ω, which is negligible compared to the resistance of the EFO discharge. The voltage is measured using an oscilloscope with a sampling rate of 500 kS/s. Tests are performed with the 25 µm (1 mil) Au and Cu2 wires used in the shielding gas type and flow rate study of chapter 3.

The EFO parameters used for the voltage measurements are listed in Table 9. A shielding gas flow rate of 0.5 l/min is used. The parameters were kept constant for both Au and Cu wires to

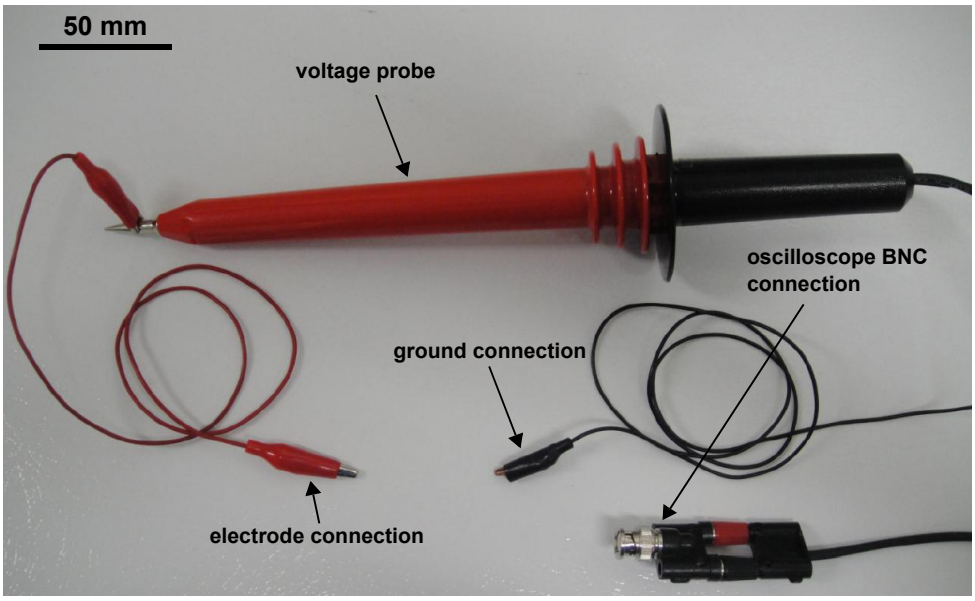

Figure 64: 1000:1 high voltage probe used to make EFO discharge voltage measurements with an oscilloscope.

make voltage comparisons easier. Due to the high thermal and electrical conductivity of the Cu wire no FAB is formed under these conditions. A higher I_{EFO} and/or t_{EFO} is required to cause sufficient melting and the formation of Cu FABs. The condition of the Au and Cu wires after EFO with these parameters is shown in Fig. 66.

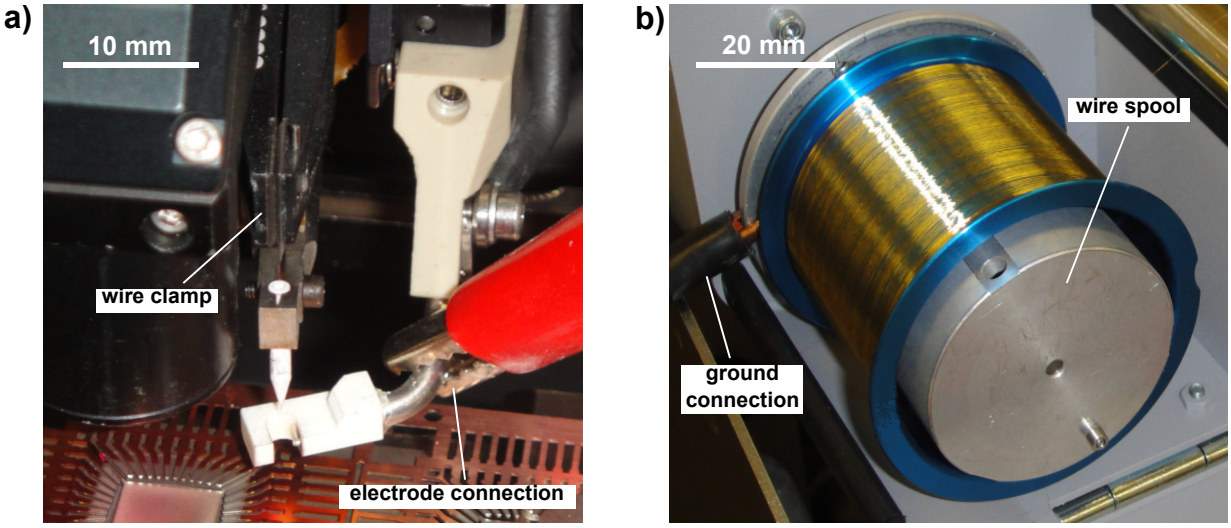

Figure 65: Voltage probe connection points on the Besi Esec 3100 wire bonder: a) ground connected to wire spool that shares a common ground with wire clamp, and b) voltage probe connected to electrode.

Table 9: Electrical flame off parameters for voltage measurements. The shielding gas flow rate is held constant at 0.5 l/min.

Parameter	Value
Gap or Electrode to Wire Distance [µm]	300
Pre-Spark Voltage [V]	4500
EFO current [mA]	50
EFO time [ms]	0.5
Tail Length [µm]	500

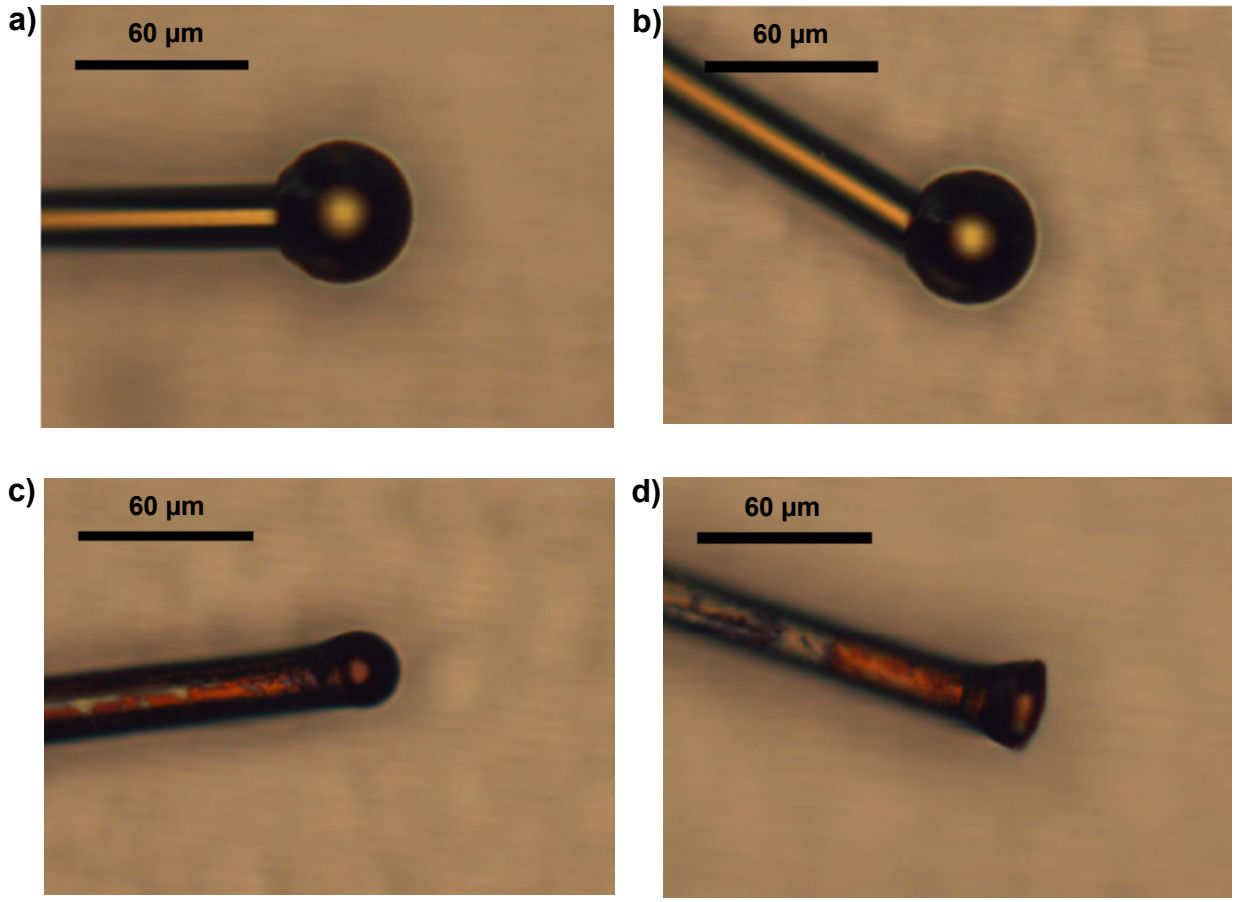

Figure 66: Optical images of wire tail after EFO for both Au and Cu wires. a) Au wire in forming gas, b) Au wire in N_2 gas, c) Cu wire in forming gas, and d) Cu wire in N_2 gas. Note the larger FAB diameter in (a) and the rounded wire tip caused by more melting (c) from the forming gas discharge.

4.2 Voltage Measurement Results

An example voltage measurement taken during the formation of a Au FAB in forming gas is shown in Fig. 67. A much higher sampling rate of 400 MS/s is used to identify the different features in the voltage measurement. The EFO discharge can be divided into 4 phases which include: i) pre-spark phase, ii) ionization phase, iii) voltage stabilization phase, and iv) steady-state voltage phase. In the pre-spark phase the voltage is increased in steps until the breakdown potential of the gap between the wire and the electrode is exceeded and ionization begins. The voltage at breakdown is approximately 1860 V in this case. The maximum pre-spark value of 4500 V from Table 9 is not actually required to start ionization in the gap. The ionization phase is only approximately 1 μs long where the voltage fluctuates greatly as shown in Fig. 68. The breakdown or ionization of a gas insulated gap is quite complex where many different theoretical models have been proposed

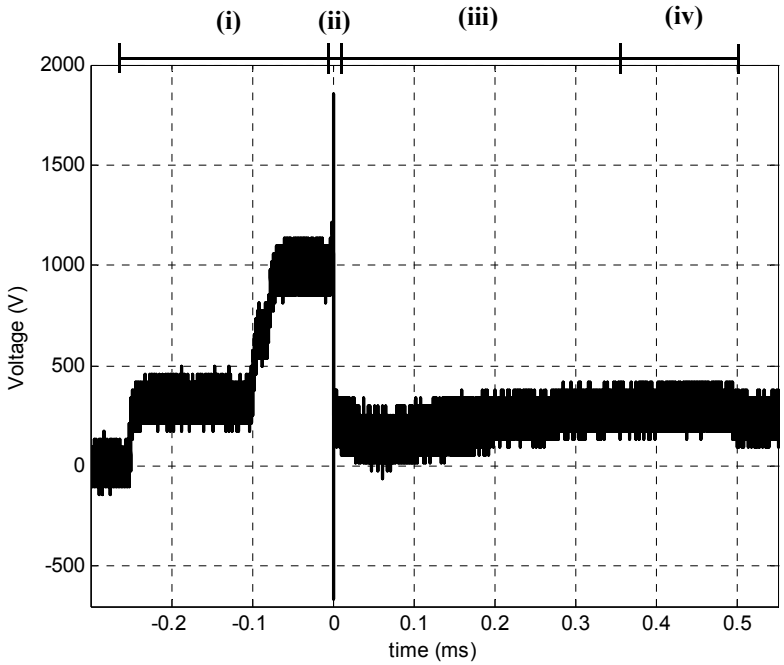

Figure 67: EFO discharge voltage measurement with Au wire anode. Sampling rate of 400 MS/s used for this measurement in order to identify the 4 phases of the discharge which include i) pre-spark phase, ii) ionization phase, iii) voltage stabilization phase, and iv) steady-state voltage phase.

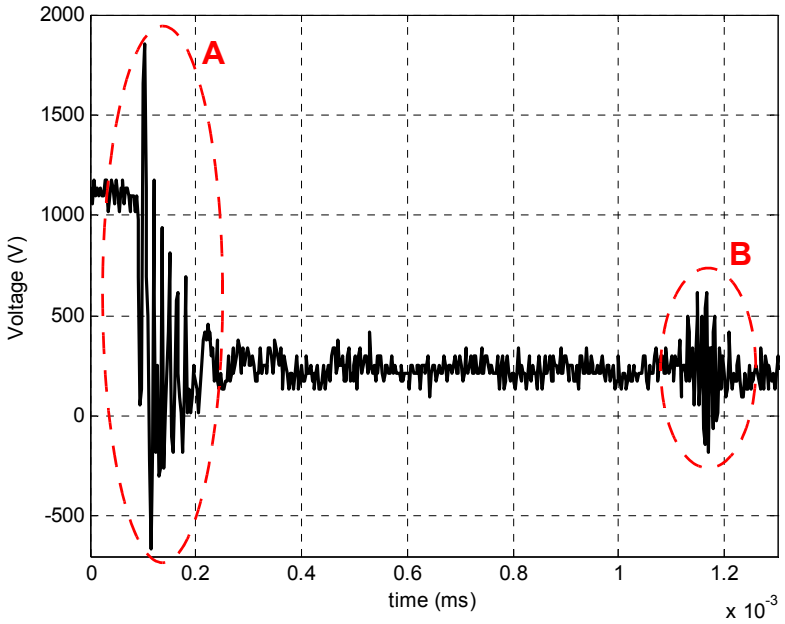

Figure 68: Ionization phase (ii) of the EFO discharge. There are two distinct large fluctuations in voltage during this phase (A & B)

[72]. In the voltage stabilization phase the voltage first drops and then rises until a steady-state is reached and the steady-state voltage phase begins.

4.2.1 Comparison of the Discharge Produced in Forming Gas and N_2 Gas with Au Wire Anode

The voltage measurements taken with the Au wire in forming gas and N_2 gas are shown in Figs. 69 a) and b), respectively. The voltage during the discharge approaches a steady state after approximately 0.36 ms. The steady-state voltage (V_{SS}) determined between 0.4 ms and 0.48 ms for the forming gas and N_2 gas tests are 200 V and 224 V, respectively. The I_{EFO} is controlled at 50 mA, therefore using equation (1) the discharge power in N_2 gas is calculated to be 11.2 W which is 12.2 % larger than that of the forming gas discharge.

By comparing the size of the Au FABs produced in each shielding gas type the amount of energy transferred to the wire anode in each gas can be compared. A larger FAB will indicate that

more energy from the discharge has been transferred to the wire anode during EFO. The FABs formed in N_2 gas are slightly golf clubbed but still remain round and therefore, the diameter can still be compared to those formed in forming gas [Figs. 66 a) and b)]. The average FAB diameter of the FABs that were formed in forming gas and N_2 gas are 48.5±0.38 µm and 45.7±0.45 µm, re-

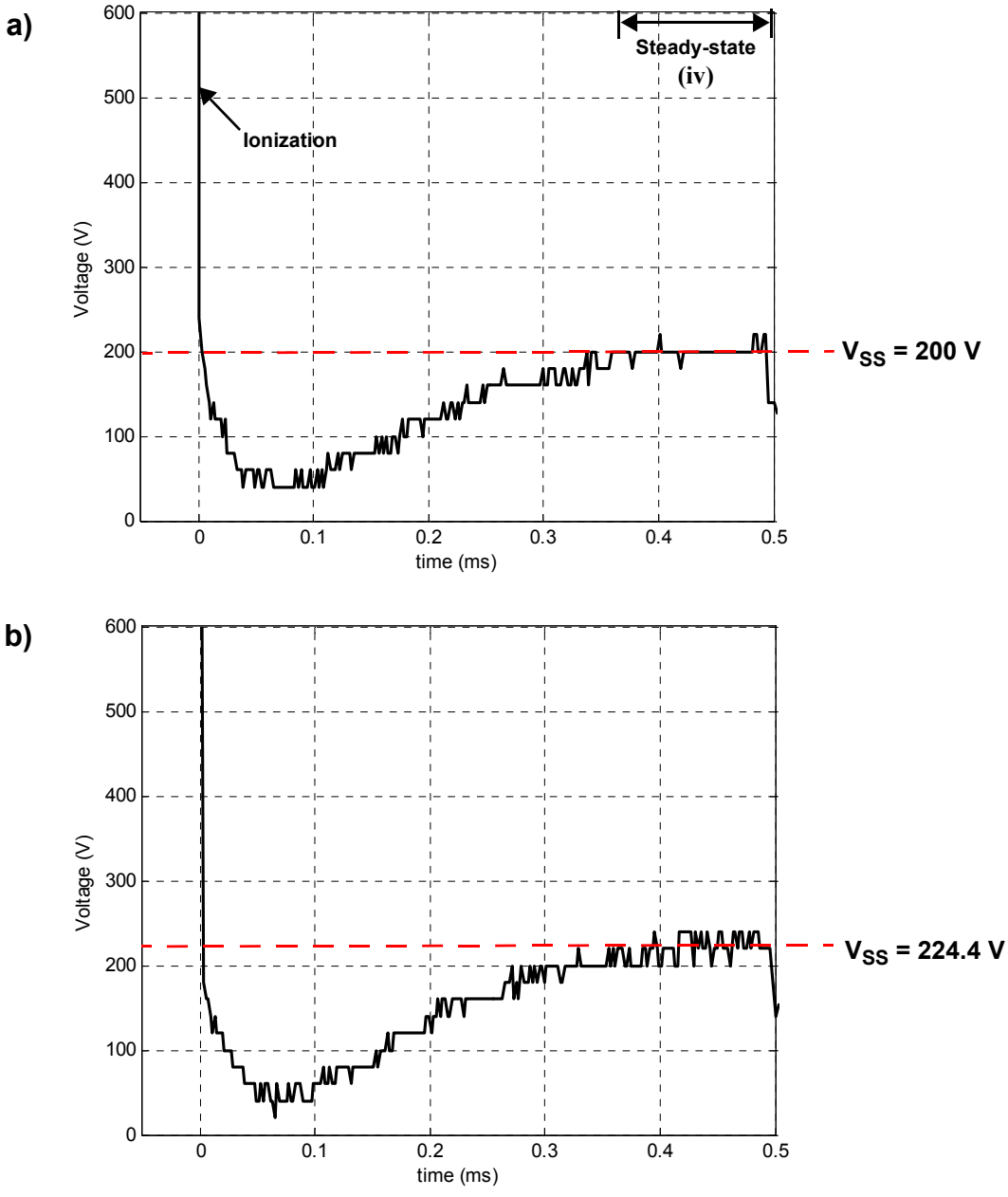

Figure 69: Voltage measurements between electrode and Au wire in (a) forming gas and in (b) N_2 gas during EFO discharge.

spectively. The FABs formed in forming gas are 6 % larger. This suggests that more energy is transferred to the wire anode in the EFO discharge produced in forming gas.

4.2.2 Comparison of the Discharge Produced in Forming Gas and N_2 Gas with Cu Wire Anode

The voltage measurements taken with the Cu wire in forming gas and N_2 gas are shown in Figs. 69 a) and b), respectively. The V_{SS} for the forming gas and N_2 gas tests are 211.7 V and 239 V, respectively. The discharge power in N_2 gas is 12 W which is 12.7 % larger than that of the discharge produced in forming gas. Therefore, the difference in EFO discharge power in the different shielding gases is similar for both the Au and Cu wires.

4.2.3 Effect of EFO current on Discharge Voltage

The I_{EFO} was increased by 60 % to 80 mA and the voltage was measured between the Cu wire and electrode in forming gas. A 5 % decrease in V_{SS} is measured. Knowing that the EFO discharge is a weakly ionized plasma [12], the I_{EFO} is in the mA range, and a 5 % decrease in voltage produces a 60 % increase in I_{EFO}, the EFO discharge most likely falls in the normal glow discharge category of electrical discharges. This is illustrated in Fig. 71 which shows the steady-state voltage versus current characteristic of discharges at a pressure of 100 Pa [13].

4.2.4 Effect of Discharge Gap on Voltage

Voltage measurements were made with Cu wire in forming gas with increasing the discharge gap from 400 µm to 1000 µm at 200 µm increments. The resulting V_{SS} values plotted against the length of the discharge gap are shown in Fig. 72. As expected the voltage increases with the gap due to the higher resistance of the longer discharge.

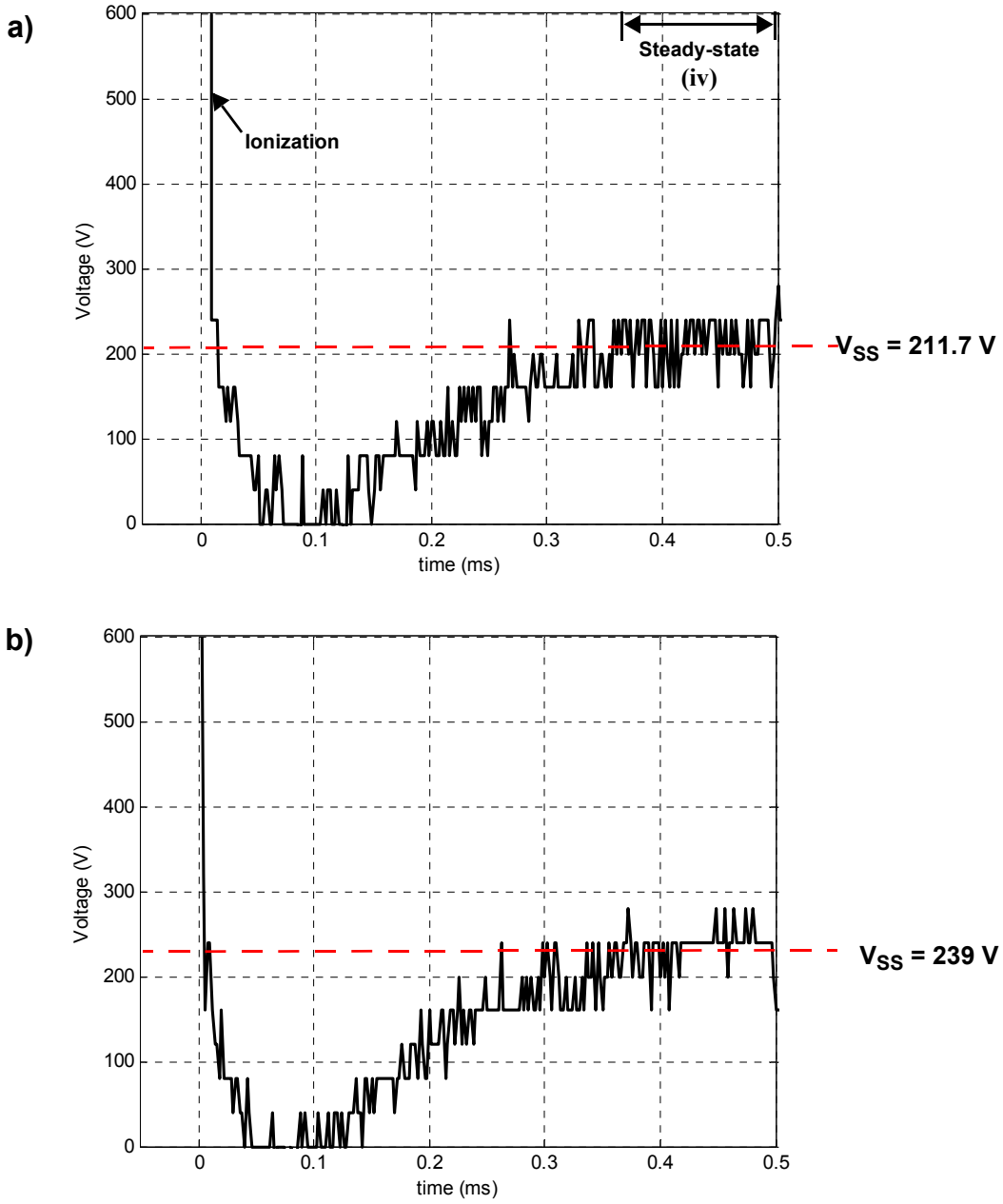

Figure 70: Voltage measurements between electrode and Cu wire in (a) forming gas and in (b) N_2 gas during EFO discharge.

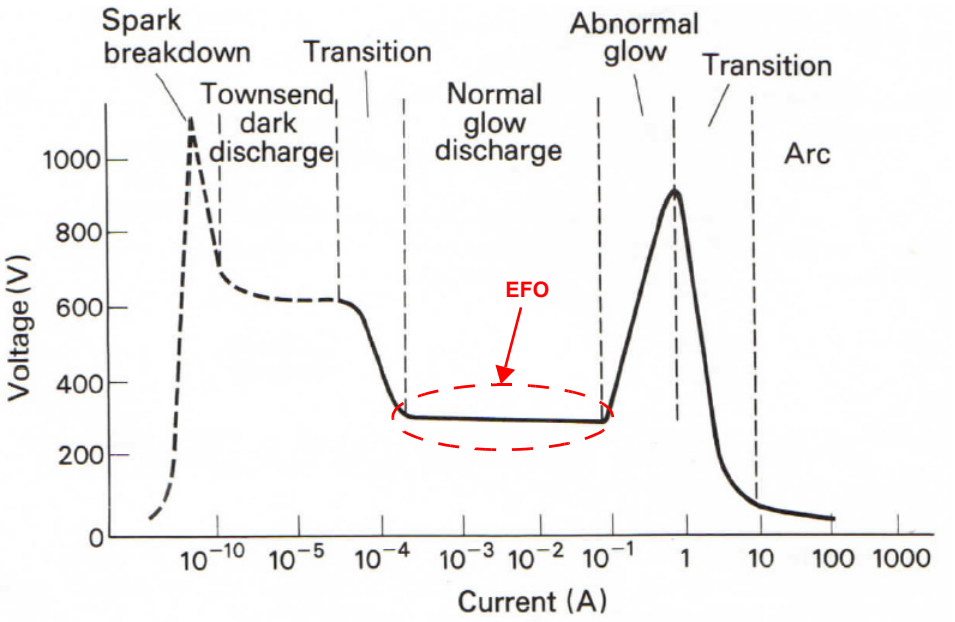

Figure 71: Steady-state voltage versus current characteristic of a discharge at approximately 100 Pa [13].

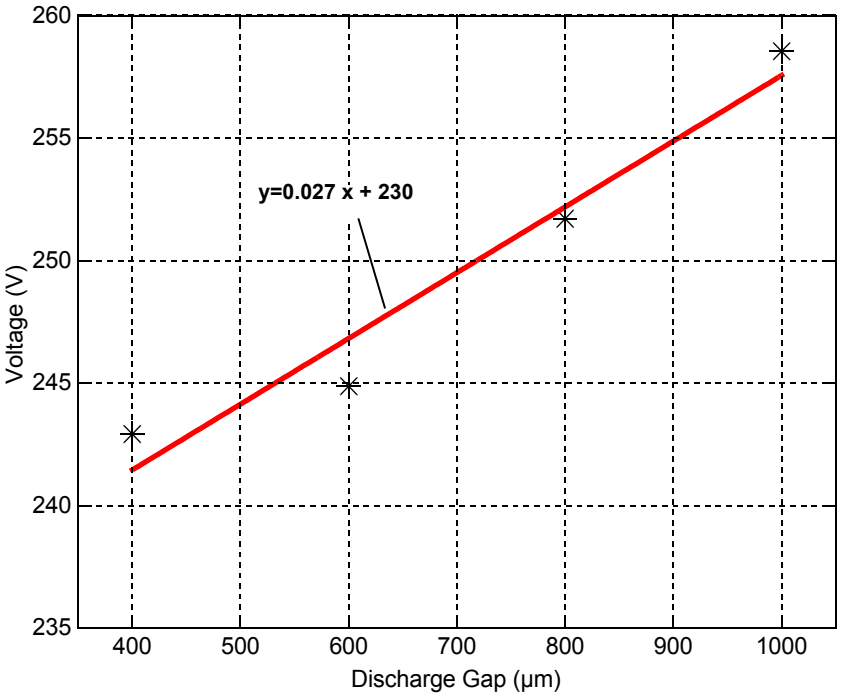

Figure 72: Steady-state voltage (V_{SS}) versus the length of the discharge gap for EFO between the electrode and Cu wire in forming gas.

4.3 Effect of Shielding Gas Type on Energy Transferred to Wire Anode

The higher power of the N_2 discharge is explained by the ionization energy of N_2 compared to H_2. Nitrogen and H_2 have ionization energies of 14.54 eV and 13.595 eV, respectively [13, 16]. By adding 5 % H_2 to the shielding gas, the gas mixture will become more ionized meaning that the electron and ion densities are higher in the discharge plasma [13, 14]. The more ionized a gas becomes, the lower the resistance across the discharge. This leads to the lower voltage required to achieve a 50 mA I_{EFO} in the forming gas discharge.

Since the Au FAB diameter is 6 % larger when formed in forming gas, the discharge power does not necessarily represent the energy transferred to the wire anode during EFO. The temperature of the discharge is determined by a balance between the electrical power input and the energy losses due to conduction, diffusion, convection, and radiation [16]. The different properties of the shielding gases have a large effect on this energy balance. For example, properties such as the thermal conductivity of the shielding gas and the percentage of energy loss due to radiation between the different types of shielding gases effects the discharge temperature [16]. The thermal conductivity of H_2 and N_2 gases for various temperatures are shown in Fig. 73, where it can be seen that the thermal conductivity of H_2 is very high compared to the other gases [16]. Radiation losses are also expected to be different between the two gases [16]. The amount of radiation increases with the higher states of ionization where more than one electron is lost from the gas atom [16]. Since, the hydrogen atom only has one electron to lose there is only one stage of ionization and therefore lower energy levels of radiation would be expected. Due to the number of factors affecting the en-

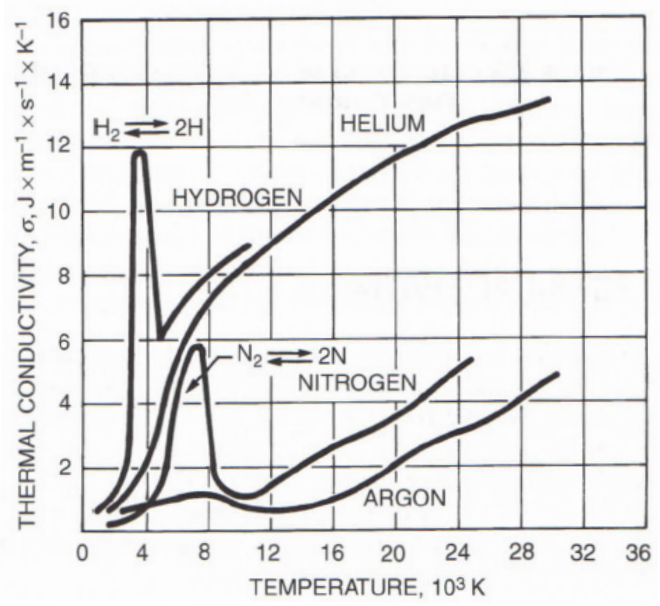

Figure 73: Thermal conductivities of H_2 and N_2 gases as a function of temperature [16].

ergy transferred to the wire, a full energy balance is required in order to determine which gas promotes a higher energy loss across the discharge.

The voltage distribution across the discharge also has a large influence on the energy transferred to the anode [16]. The highest potential is usually in the anode fall region [16]. The discharge shape and therefore, current density can vary across the discharge which influences the temperature. This is often referred to as "constriction" in the arc welding industry where the arc shape changes [64-70]. The area that the current flows into the anode has the largest effect on the heat energy [16]. Therefore, constriction of the discharge at the wire will have a significant effect on the FAB. Constriction occurs due to several different mechanisms. Three of these mechanisms include: i) large ionization potential preventing ionization away from the high energy portion of the discharge (ex. He shielding gases in arc welding) [67], ii) high thermal conductivity and specific heat keeping the temperature of the edges of the discharge column too low for ionization to occur,

which is called the “thermal pinch” effect (ex. H_2+ Ar shielding gas in arc welding) [64, 67, 73], and iii) electrons captured in the cooler outer regions of the discharge by O_2 and halogens (Cl and F) that have a higher electron affinity (ex. activating fluxes in arc welding) [69]. Constriction caused by the thermal pinch effect of adding H_2 to the shielding gas has been considered a possible mechanism for the increased energy input during EFO and for improving the shape of the FAB [7].

4.4 Effect of Wire Anode on Discharge Characteristics

The EFO discharge with the Cu wire anode produces a 6 % higher V_{SS} than the discharge between the electrode and the Au anode. This phenomenon could be due to the low ionization energies of metal vapours assuming that the temperature reached at the wire anode is high enough to cause vaporization [13, 71]. Since insufficient melting occurred to form a Cu FAB with the selected EFO parameters, it is likely that there is not enough heat to produce metal vapour [Figs. 66 c) and d)]. This would cause less ionization in the discharge plasma with the Cu wire anode and will increase the resistance across the discharge. A higher voltage would therefore be required to achieve the required I_{EFO} of 50 mA. However, the ionization energies of Au and Cu are 7.726 eV and 9.225 eV, respectively, and Cu has a higher vapour pressure than Au as shown in Fig. 74 [16, 74]. Therefore, if the I_{EFO} or t_{EFO} is increased where a Cu FAB is produced and vaporization of the Cu wire occurs, the V_{SS} would be expected to decrease due to the ionization of the Cu metal vapour.

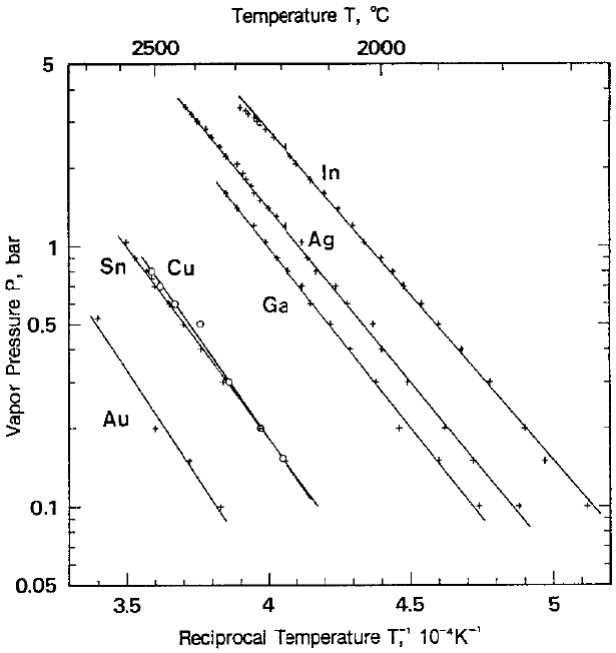

Figure 74: Vapour pressures of Au and Cu at high temperatures [74].

The condition of the wire tail could also cause changes in the measured discharge voltages. For example the Cu wire tail is often bent away from the electrode due to the bond-off direction used to create the tail as shown in Fig. 75 a). The tip of the wire tail is in the shape of a hook bending away from the electrode increasing the gap between the electrode and the wire [12]. The wire tail is also sometimes bent as illustrated in Figs. 70 b) and c) for both the Au and Cu wires. This will also have an effect on the distance the discharge must span. It has been shown in section 4.2.4 that the discharge gap has an effect on the measured V_{SS}. Therefore, the condition of the wire tail will change the gap and will influence the discharge voltage.

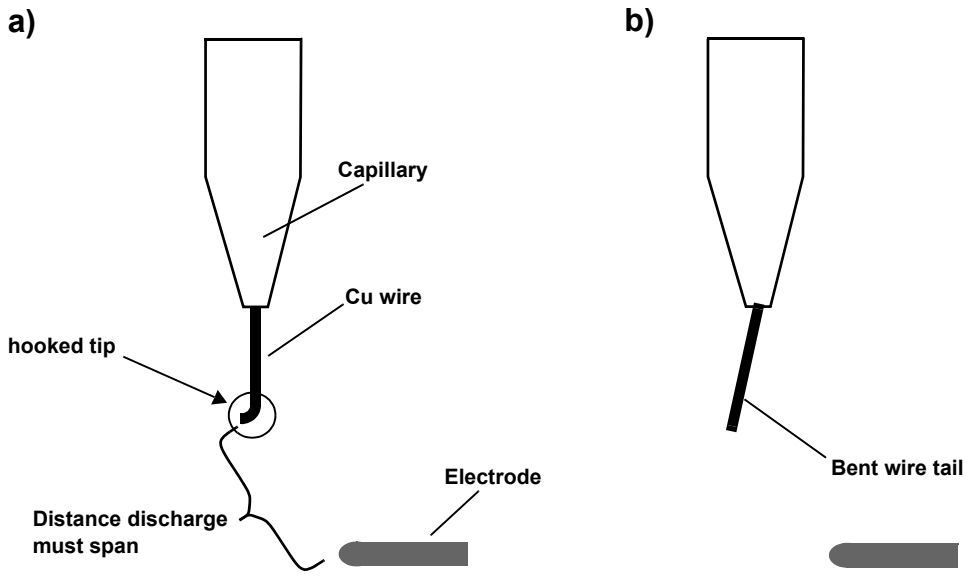

Figure 75: Illustration of common wire tail abnormalities that can effect the measured EFO discharge voltage; a) Hooked tail tip, and b) bent wire tails.

4.5 Summary

The power of the N_2 gas discharge is 12 % higher than that of the discharge produced in the 5 % H_2 + 95 % N_2 forming gas. However, the Au FAB produced in the forming gas has a 6 % larger diameter than the FAB produced in N_2 gas and more melting is observed on the Cu wire tail when the discharge is produced in forming gas. Factors such as lower energy loss in the discharge, or constriction that effects the flow of heat energy into the wire are likely to be a source of additional heat energy from the H_2 in the forming gas.

Factors that effect the discharge voltage are the selected control current, discharge gap, and the wire anode material where:

a) a 5 % increase in discharge voltage is observed with a 60 % increase in the controlled current,

b) the discharge voltages increases linearly with the gap due to the increase in resistance of the longer discharge, and

c) the EFO discharge with the Cu wire anode produces a 6 % higher V_{SS} than the discharge between the electrode and the Au anode.

The larger heat input caused by adding H_2 to the shielding gas is not due to an increase in the overall EFO discharge power. More research on how H_2 effects the EFO discharge is required in order to determine the exact cause of the additional heat input.

5.0 Conclusions

In this study a better understanding of the EFO process is obtained by investigating the effects of EFO parameters and shielding gas types on Au and Cu FABs. The knowledge obtained through this study helps to advance the EFO step of the thermosonic ball bonding process. The behaviour of novel wire materials such as Cu, coated, and insulated wires during EFO can now be better predicted leading to higher quality FABs and ball bonds. The main FAB issues associated with new wire materials such as higher hardness and oxidation are addressed and the conditions at which acceptable FAB shape and quality occur are identified.

By applying the online deformability method along with microhardness testing it is found that the EFO parameters have a substantial effect on FAB hardness and the amount of work hardening that occurs during deformation. Upon initial deformation, as typically observed in microelectronic ball bonding, work hardening occurs for both Au and Cu FABs and depends on EFO parameters in a similar way for both materials. The work hardening effect is stronger with FABs produced with lower I_{EFO} levels and longer t_{EFO} even though the hardness of the FAB is lower. A better understanding of FAB hardness and deformability which influences the US stress, and bonding force levels present during bonding is achieved. Such understanding helps to reduce underpad damage in the ball bonding process.

An online method is developed that is used to characterize FABs during bonding. The EFO process has been studied using both forming gas and N_2 gas. The gas flow rates required to produce acceptable FABs are identified and therefore the online FAB characterization method is a useful tool for optimizing the shielding gas flow rate. It is concluded that it is important to optimize the

flow rate for each new wire type used. It is also confirmed that the addition of H_2 to the gas mixture provides additional thermal energy to the EFO process and reduces oxidation during EFO. Consequently, the likelihood of forming defective FABs decreases. The additional thermal energy provided by forming gas containing 5 % H_2 is determined to not be only a result of the reduction of oxides but of at least one other source.

The characteristics of the discharge is investigated by measuring the discharge voltage during EFO. It is found that the power of the N_2 gas discharge is greater than that of the discharge produced in the 5 % H_2 + 95 % N_2 forming gas. However, Au FABs produced in a forming gas atmosphere have 6 % larger diameter than the FAB produced in N_2 gas. Lower energy loss in the discharge and/or constriction that effects the flow of heat energy into the wire anode are likely to be a source of additional heat energy from the H_2 in the forming gas. Other factors that were found to affect the voltage of the EFO discharge include the controlled EFO current, the discharge gap, and the wire anode material. More research is still required to determine the exact cause of the additional thermal energy caused by adding H_2 to the shielding gas.

References

[1] S. K. Prasad, *Advanced Wirebond Interconnection Technology*, Kluwer Academic Publishers, Boston, Massachusetts, USA, 2004.

[2] G. Harman, *Wire Bonding in Microelectronics Materials, Process, Reliability, and Yield*, 2nd edn., McGraw-Hill, New York, New York, USA, 1997.

[3] W. J. Greig, *Integrated Circuit Packaging, Assembly and Interconnections*, Springer Science + Business Media LLC, 2007.

[4] Y. Zhou, *Microjoining and Nanojoining*, Woodhead Publishing Ltd., Cambridge, England, 2008.

[5] H. M. Buschbeck, The Future is Copper, Published in European Semiconductor Dec 2004/ Jan. 2005, Available online at: <http://www.kns.com/UPLOADFILES/DGALLERY/2008.PDF>.

[6] R. Lyn, W. Crockett, Assembly using X-wire^{TM} Insulated Bonding Wire Technology, in proceedings of SEMICON Singapore Conf. (2007), pp. 33-39.

[7] T. Uno, K. Kimura, T. Yamada, Surface-enhanced Copper Bonding Wire for LSI and its Bond Reliability Under Humid Environment, in proceedings of IEEE 59th Electronics Components and Technology Conf. (2009), pp. 1486-1495.

[8] G. Harman, J. Albers, The Ultrasonic Welding Mechanism as Applied to Aluminum- and Gold-wire Bonding in Microelectronics, IEEE Transactions on parts, hybrids, and packaging, Vol. PHP-13, NO.4 (1977), pp. 406-412.

[9] C. Hang, C. Wang, M. Shi, X. Wu, H. Wang, Study of Copper Free Air Ball in Thermosonic Copper Ball Bonding, in proceedings of IEEE 6th International Conference on Electronics Packaging Technology (2005), pp. 414-418.

[10] J. F. Caers, A. Bischoff, J. Falk, J. Roggen, Conditions for Reliable Ball-wedge Copper Wire Bonding, in proceedings of IEEE Japan International Electronics Manufacturing Technology Symposium (1993), pp. 312-315.

[11] H. Xu, C. Liu, V. Silberschmidt, H. Wang, Effects of Process Parameters on Bondability in Thermosonic Copper Ball Bonding, in proceedings of Electronic Components and Technology Conference (2008), pp. 1424-1430.

[12] S. S. Sripada, *Fundamental Studies of Plasma Applications in Microelectronic Manufacturing and Flames: Fluid Mechanics, Phase-change, and Heat Transfer*, PhD Dissertation, University of Pennsylvania, Pennsylvania, USA (1999).

[13] J. F. Lancaster, *The Physics of Welding*, 2nd edn., International Institute of Welding, Pergamon Press, Headington Hill Hall, Oxford, England, 1986.

[14] W. Qin, I. Cohen, P. Ayyaswamy, Charged Particle Distributions and Heat Transfer in a Discharge Between Geometrically Dissimilar Electrodes: From Breakdown to Steady State, Physics of Plasmas, Vol. 7, No. 2 (2000), pp. 719-728.

[15] R. A. Wijsman, Breakdown Probability of a Low Pressure Gas Discharge, Physical Review, Vol. 75, No. 5 (1949), pp. 833-838.

[16] C. L. Jenny, A. O'Brien, *Welding Handbook*, Ninth Edition, Vol. 1, American Welding Society, Miami, Florida, USA, 2001.

[17] K. Toyozawa, K. Fujita, S. Minamide, T. Maeda, Development of Copper Wire Bonding Application Technology, IEEE Transactions on Components, Hybrids, and Manufacturing Technology, Vol. 13 No. 4 (1990), pp. 667-672.

[18] S. Khoury, D. Burkhard, D. Galloway, T. Scharr, A Comparison of Copper and Gold Wire Bonding on Integrated Circuit Devices, IEEE Transactions on Components, Hybrids, and Manufacturing Technology, Vol. 13 No. 4 (1990), pp. 673-681.

[19] S. Sripada, I. Cohen, P. Ayyaswamy, Melting of a Wire Anode Followed by Solidification: A Three-phase Moving Interface Problem, Journal of Heat Transfer, Vol. 125 (2003), pp. 661-668.

[20] H. M. HO, J. Tan, Y.C. Tan, B.H. Toh, P. Xavier, Modeling Energy Transfer to Copper Wire for Bonding in an Inert Environment, in proceedings of IEEE Electronics Packaging Technology Conf. (2005), pp. 292-297.

[21] K. C. Joshi, The Formation of Ultrasonic Bonds Between Metals, Welding Journal, Vol. 50 (1971), pp. 840-848.

[22] J. E. Krazanowski, A Transmission Electron Microscopy Study of Ultrasonic Wire Bonding, IEEE Transactions on Components, Hybrids, and Manufacturing Technology (1990), pp. 176-181.

[23] G. Harman, K. O. Leedy, An Experimental Model of the Microelectonic Ultrasonic Wire Bonding Mechanism, in proceedings of the 10^{th} annual Reliability Physics Conf. (1972), pp. 49-56.

[24] H. H. Yu, Z. Suo, Mechanics and Physics of Solids, A Model of Wafer Bonding by Elastic Accommodation, Vol. 46, No. 5 (1998), pp. 829-844.

[25] T. Worren, K. H. Hansen, E. Laegsgaard, f. Besenbacker, I. Stensgaard, Copper Clusters on Al2O3/NiAl(110) Studied with STM, Surface Science, Vol. 447 (2001), pp. 8-16.

[26] S. P. Hannula, J. Wanagel, C. Y. Li, Evaluation of Mechanical Properties of Thin Wires for Electrical Interconnections, IEEE Transactions on Components, Hybrids, and Manufacturing Technology, Vol. 6, No. 4 (1983).

[27] F. Y. Hung, T. S. Lui, L. H. Chen, Y. C. Lin, Recrystallization, Electric Flame-off Characteristics, and Electron Backscatter Diffraction of Copper Bondign Wires, IEEE Transactions on Advanced Packaging, Vol. 23, No. 1 (2010).

[28] D. R. Askeland, P. P. Phule, *The Science and Engineering of Materials, 4th ed.*, Thomson Brooks/Cole, Pacific Grove, California, USA, 2003.

[29] B. Langenecker, Effects of Ultrasound on Deformation Characteristics of Metals, IEEE Transactions on Sonics and Ultrasonics, Vol. SU-13, No. 1 (1966), pp. 1-8.

[30] V. P. Severdenko, V. V. Klubovich, A. V. Stepanenko, *Ultrasonic Rolling and Drawing of Metals*, Consultants Bureau, New York, New York, USA, 1972.

[31] D. R. Culp, H. T. Gencsoy, Metal Deformation with Ultrasound, in proceedings of Ultrasonics Symposium (1973), pp. 195-198.

[32] W. H. Song, C. Hang, A. Pequegnat, M. Mayer, N. Y. Zhou, Y. K. Song, J. Persic, Comparison of Insulted with Bare Au Bonding Wire: HAZ Length, HAZ Breaking Force, and FAB Deformability, Journal of Electronic Materials, Vol. 38, No. 6 (2009), pp. 834-842.

[33] MIL-STD-883E: Bond Strength (destructive bond pull test), METHOD 2011.7 (1989), pp. 1-6.

[34] H. Huang, A. Pequegnat, B.H. Chang, M. Mayer, D. Du, Y. Zhou, Influence of Superimposed Ultrasound on Deformability of Cu, Journal of Applied Physics, Vol. 106, 113514 (2009), doi: 10.1063/1.3266170.

[35] A. Pequegnat, C. J. Hang, M. Mayer, Y. Zhou, J. T. Moon, J. Persic, Effect of EFO Parameters on Cu FAB Hardness and Work Hardening in Thermosonic Wire Bonding, Journal of Materials Science: Electronic Materials, Vol. 20 (2009), pp. 1144-1149.

[36] JEDEC Standard JESD22-B116, Electronic Industries Alliance, July 1998.

[37] S. Murali, N. Srikanth, C. J. Vath III, Grains, Deformation Substructures, and Slip Bands Observed in Thermosonic Copper Ball Bonding, Materials Characterization, Vol. 50 (2003), pp. 39-50.

[38] Z. W. Zhong, H. M. Ho, Y. C. Tan, W. C. Tan, H. M. Goh, B. H. Toh, J. Tan, Study of Factors Affecting the Hardness of Ball Bonds in Copper Wire Bonding, Microelectronic Engineering, Vol. 84 (2007), pp. 368-374.

[39] J. H. Westbrook, H. Conrad, *The Science of Hardness Testing and its Research Applications*, American Society for Metals, ASM, Ohio, USA, 1973.

[40] C. J. Hang, I. Lum, J. Lee, M. Mayer, C. Q. Wang, Y. Zhou, S. J. Hong, S. M. Lee, Bonding Wire Characterization Using Automatic Deformability Measurement, Microelectronics Engineering, Vol. 85 (2008), pp. 1795-1803.

[41] J. Lee, M. Mayer, Y. Zhou, S. J. Hong, Iterative Optimization of Tail Breaking Force of 1 mil Wire Thermosonic Ball Bonding Process and the Influence of Plasma Cleaning, Microelectronics Journal, Vol. 38 (2007), pp. 842-847.

[42] C. J. Hang, W. H. Song, I. Lum, M. Mayer, Y. Zhou, C. Q. Wang, J. T. Moon, J. Persic, Effect of Electronic Flame off Parameters on Copper Bonding Wire: Free-air Ball Deformability, Heat Affected Zone Length, Heat Affected Zone Breaking Force, Microelectronic Engineering, Vol. 86 (2009), pp. 2094-2103.

[43] S. Hu, R. Lim, G. Sow, Gold Wire Weakening in the Thermosonic Bonding of the First Bond, IEEE Transactions on Components, Packaging, and Manufacturing Technology, Vol. 18, No. 1 (1995), pp. 230-234.

[44] I. Lum, C. J. Hang, M. Mayer, Y. Zhou, In Situ Studies of the Effects of Ultrasound During Deformation on Residual Hardness of a Metal, Journal of Electronic Materials, Vol. 38, No. 5 (2009), pp. 647-653.

[45] I. Lum, H. Huang, B. H. Chang, M. Mayer, D. Du, Y. Zhou, Effects of Superimposed Ultrasound on Deformation of Gold, Journal of Applied Physics, Vol. 105, 024905 (2009).

[46] A. Pequegnat, M. Mayer, J. Persic, Y. Zhou, Accelerated Characterization of Bonding Wire Materials, in the proceedings of IMAPs 42nd International Symposium on Microelectronics (2009), pp. 367-373.

[47] M. Deley, L. Levine, The Emergence of High Volume Copper Ball Bonding, Kulicke & Soffa Technical Library (2004), Available online at: <http://www.kns.com/UPLOADFILES/DGALLERY/2011.PDF>.

[48] J. Onuki, M. Koizumi, I Araki, Investigation of the Reliability of Copper Ball Bonds to Aluminum Electrodes, IEEE Transactions on Components, Hybrids, and Manufacturing Technology, Vol. 10 (1987), pp. 550-555.

[49] D. Olsen, K. James, Evaluation of the Potential Reliability Effects of Ambient Atmosphere on Aluminum-Copper Bonding in Semiconductor Products, IEEE Transactions on Components, Hybrids, and Manufacturing Technology, Vol. 7 (1984), pp. 357-362.

[50] A. Shah, M. Mayer, Y. Zhou, S. J. Hong, J. T. Moon, Reduction of Underpad Stress in Thermosonic Copper Ball Bonding, in proceedings of the 58th Electronic Components and Technology Conference (2008), p. 2123-2130.

[51] A. Shah, M. Mayer, Y. Zhou, S. J. Hong, J. T. Moon, In situ Ultrasonic force signals during Low-temperature Thermosonic Copper Wire Bonding, Microelectronics Engineering, Vol. 85 (2008), pp. 1851-1857.

[52] S. Narasimalu, Wire Bond Challenges in Low-k devices, Microelectonics International, Vol. 25, No. 1 (2008), pp. 34-40.

[53] Z. W. Zhong, Wire Bonding Using Insulated Wire and New Challenges in Wire Bonding, Microelectronics International, Vol. 25, No. 2 (2008), pp. 9-14.

[54] B. Hatton, K. Landskron, W. Hunks, M. Bennett, D. Shukaris, D. Perovic, G. Ozin, Materials Chemistry for Low-k Materials, Materials Today, Vol. 9 (2006), pp. 22-31.

[55] R. Lyn, J. Persic, Y. K. Song, Overview of X-wire^{TM} Insulated Bonding Wire Technology, in proceedings of IMAPS 39th International Symposium on Microelectronics (2006), pp. 1-7.

[56] S. Okikawa, M. Tanimoto, H. Watanabe, H. Mikino, T. Kaneda, Development of a Coated Wire Bonding Technology, IEEE Transactions of Components, Hybrids, and Manufacturing Technology, Vol. 12, NO. 4 (1989), pp. 603-608.

[57] Y. F. Yao, T. Y. Lin, K. H. Chua, Improving the deflection of wire bonds in stacked chip scale packages (CSP), Microelectronics Reliability, Vol. 43 (2003), pp. 2039-2045.

[58] J. Lee, M. Mayer, N. Zhou, J. Persic, Microelectronic Wire Bonding with Insulated Au Wire: Effects of Process Parameters on Insulation Removal and Crescent Bonding, Materials Transactions, Vol. 49, No. 10 (2008), pp. 2347-2353.

[59] J. Onuki, M. Koizumi, H. Suzuki, Influence of Ball-forming Conditions on the Hardness of Copper Balls, Journal of Applied Physics, Vol. 68, No. 2 (1990), pp. 5610-5614.

[60] C. J. Hang, C. Q. Wang, Y. H. Tian, M. Mayer, Y. Zhou, Microstructural Study of Copper Free Air Balls in Thermosonic Wire Bonding, Microelectronic Engineering, Vol. 85 (2008), pp. 1815-1819.

[61] J. H. Cho, J. S. Cho, J. T. Moon, J. Lee, Y. H. Cho, Y. W. Kim, A. D. Rollett, K.H. Oh, Metallurgical and Materials Transactions, Vol. 34A, No. 5 (2003), pp. 1113-1125.

[62] ASM Handbook Vol. 2, Properties and Selection: Nonferrous Alloys and Special-Purpose Materials, ASM International (1992).

[63] G. Qui, S. Zhang, Recrystallization of Gold Alloys for Producing Fine Bonding Wires, Journal of Materials Processing Technology, Vol. 68, No. 3 (1997), pp. 288-293.

[64] J. Tusek, M. Suban, Experimental Research of the Effect of Hydrogen in Argon as a Shielding Gas in Arc Welding of High-alloy Stainless Steel, International Journal of Hydrogen Energy, Vol. 25 (2000), pp. 369-376.

[65] J. J. Lowke, R. Morrow, H. Haidar, A. B. Murphy, Prediction of Gas Tungsten Arc Welding Properties in Mixtures of Argon and Hydrogen, IEEE Transactions on Plasma Science, Vol. 25, No. 5 (1997), pp. 925-930.

[66] A. Durgutlu, Experimental Investigation of the Effect of Hydrogen on Argon as a Shielding Gas on TIG Welding of Austenitic Stainless Steel, Materials and Design, Vol 25 (2004), pp. 19-23.

[67] M. Tanaka, S. Tashiro, M. Ushio, T. Mita, A. B. Murphy, J. J. Lowke, CO2-shielded Arc as a High-intensity Heat Source, Vacuum, Vol. 80 (2006), pp. 1195-1198.

[68] D. S. Howse, W. Lucas, Investigation into Arc Constriction by Active Fluxes for Tungsten Inter Gas Welding, Science and Technology of Welding and Joining, Vol. 5, No. 3 (2000), pp. 189-193.

[69] M. Tanaka, T. Shimizu, H. Terasaki, M. Ushio, F. Koshi-ishi, C. L. Yang, Effects of Activating Flux on Arc Phenomena in Gas Tungsten Arc Welding, Science and Technology of Welding and Joining, Vol. 5, No. 6 (2000), pp. 397-402.

[70] P. V. Poritskii, Thermal Contraction of Arc Discharges in Mixtures of Inter Gasses: Special Features, High Temperature, Vol. 44, No. 3 (2006), pp. 328-335, Translated from Teplofizika Vysokikh Temperatur, Vol. 44, No. 3 (2006), pp. 335-342.

[71] S. Tashiro, M. Tanaka, N. Nakata, T. Iwao, F. Koshiishi, K. Suzuki, K. Yamazaki, Plasma Properties of Helium Gas Tungsten Arc Wire Metal Vapour, Science and Technology of Welding and Joining, Vol 12, No. 3 (2007), pp. 202-207.

[72] E. E. Kunhardt, Electrical Breakdown of Gases: The Prebreakdown Stage, IEEE Transactions on Plasma Science, Vol. PS-8, No. 3 (1980), pp. 130-138.

[73] P. V. Porytskyy, A. M. Veklich, On the Influence of Metal Impurities on the Thermal Contraction of a Nitrogen Arc, Plasma Physics, Vol. 12 (2006), pp. 222-224.

[74] F. Geiger, C. A. Busse, R. I. Loehrke, The Vapor Pressure of Indium, Silver, Gallium, Copper, Tin, and Gold Between 0.1 and 3.0 Bar, International Journal of Thermophysics, Vol 8, No. 4 (1987), pp. 425-436.